SWEDISH DEFENCE
RESEARCH AGENCY

FOI-R–0330–SE
December 5, 2001
ISSN 1650-1942

Scientific report

Kristoffer Jensen and Gunilla Efraimsson

Aeroengine Fan-Noise Resolution Requirement in Computational Fluid Dynamics

Division of Aeronautics, FFA
SE-172 90 STOCKHOLM

FOI – Swedish Defence Research Agency
Division of Aeronautics, FFA
SE-172 90 STOCKHOLM

FOI-R–0330–SE
December 5, 2001
ISSN 1650-1942

Scientific report

Kristoffer Jensen and Gunilla Efraimsson

Aeroengine Fan-Noise Resolution Requirement in Computational Fluid Dynamics

Division of Aeronautics, FFA
SE-172 90 STOCKHOLM

Abstract

Jet-noise has eventually been reduced to a minimum, but still there are problems in keeping the overall noise levels low during take-off and approach. The reason for this is basically that fan-noise, i.e. pressure fluctuations generated in the compressor or turbine, becomes dominating. This phenomenon can be recognized as non-linear and complex aerodynamics rather than acoustic problem in nature, and thus it becomes difficult to obtain models that are general and accurate. However, with the aid of CFD, the problem can now be studied in detail, but unfortunately this requires a very large number of points per wavelength to distinguish the wave solution from numerical errors.

Applying the well-established linear methods for aeroacoustics in a parallel wall-duct to the fan stage, one can obtain analytical expressions for the dispersion-relation. A sinusoidal acoustic wave with the known dispersion-relation is then propagated thru a 2D numerical fan stage using a time-dependent finite-volume scheme. The numerical solution is then compared with the original wave to identify deviations that could originate from dispersion, dissipation and reflections induced by the numerical boundaries.

An optimal number of points per wavelength were not established exactly, but in order to have good results within reasonable computational time a rough estimate of around 20 - 40 points per circumferential wavelength has shown to be sufficient to preserve the wave. In addition, certain physical and numerical phenomena applied to aeroacoustics has been more clarified, that includes; viscous interaction, numerical dispersion and dissipation of the sound waves, dependence of number of time steps per period, influence of different grid skew angles, and the errors induced by improper boundary conditions.

Contents

Appendix A

Appendix B

Appendix C

Appendix D

Appendix E

1 Introduction

The silence of the birds was for real broken in 1902 when the Wright brothers entered the free airspace with their propeller driven aircraft. The exceptional advantages of the ground-independent vehicles gave a quick increase in number, later substituting slow boats and cars with the fast and comfortable aircraft. The development was rapid, starting with small aircrafts mainly used in military operations and later continued on to larger and faster aircraft, both for military and civil use. In 1919 air transport of passenger started, using propeller driven single and multi-engine aircraft. Increasing air traffic and the need for larger and faster aircraft, in a combination of wartime, initiated development of turbine-powered propulsion (Turbojet engine). In 1944 the first operational turbine-powered aircraft for military use was introduced, the German Messerschmitt Me 262, which was used as a “Blitzbomber” during the Second World War. Followed up by the first turbine-powered aircraft for civil passenger transport 8 years later; the De Havilland Comet in May 1952. The Comet marked a milestone for the new era of jet-powered transport aircrafts.

The large advantages of jet-powered aircraft sat pace for research and development on jet-engines with better performance. Associated with the better performance and larger engines, there was also a steep increase in noise emitted – especially during take-off and approaches. This, in combination with airports situated very close to the cities, noise regulations during near-city flights were introduced. Therefore, methods to develop jet-engines quiet enough to fulfill new airport regulations were needed.

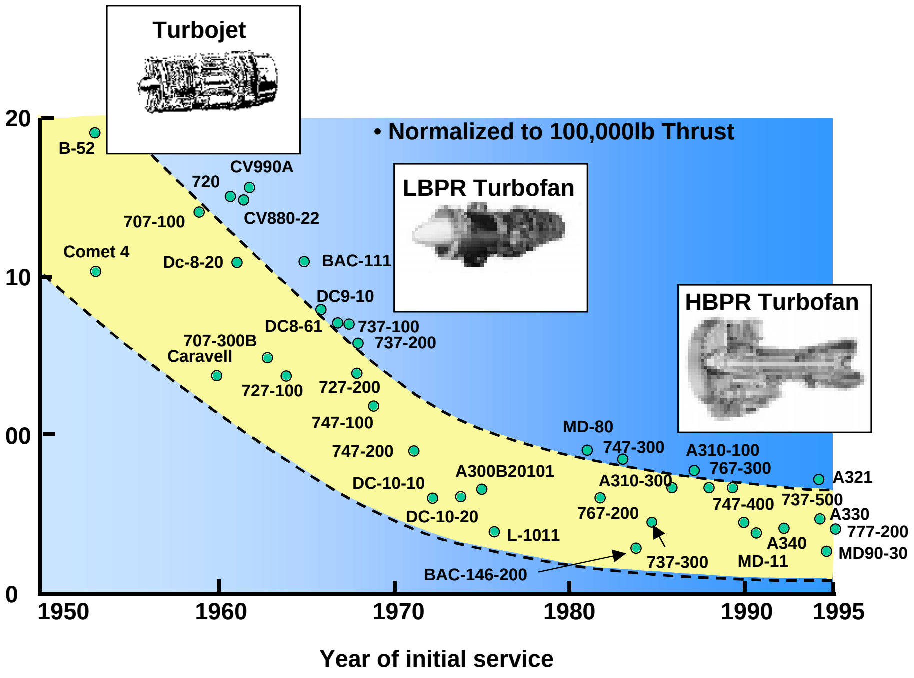

Figure 1. Normalized noise levels of transport aircraft by year of entry into service. The noise levels for configurations are at time of initial service, EPNdB.

In 1951, Sir James Lighthill proposed a coupling between the well-established fluid mechanical equations and the acoustics equations, Lighthill’s equation (e.g. [7]). This gave rise to the so-called U^8-law, $W = \alpha \frac{\rho_0 D^2 U^8}{c_0^5}$, which indicates that the acoustic effect from a jet is proportional to both velocity U of the power of eight and nozzle diameter D of the power of two at the jet-outlet. The consensus of this dictates that to retain the same performance, but to reduce noise, one has to lower the exit velocity and higher the nozzle diameter. This gave birth to the so-called Turbofan engine, which have over the last four decades reduced noise levels with about 30 dB (second-generation Turbofan), Figure 1.

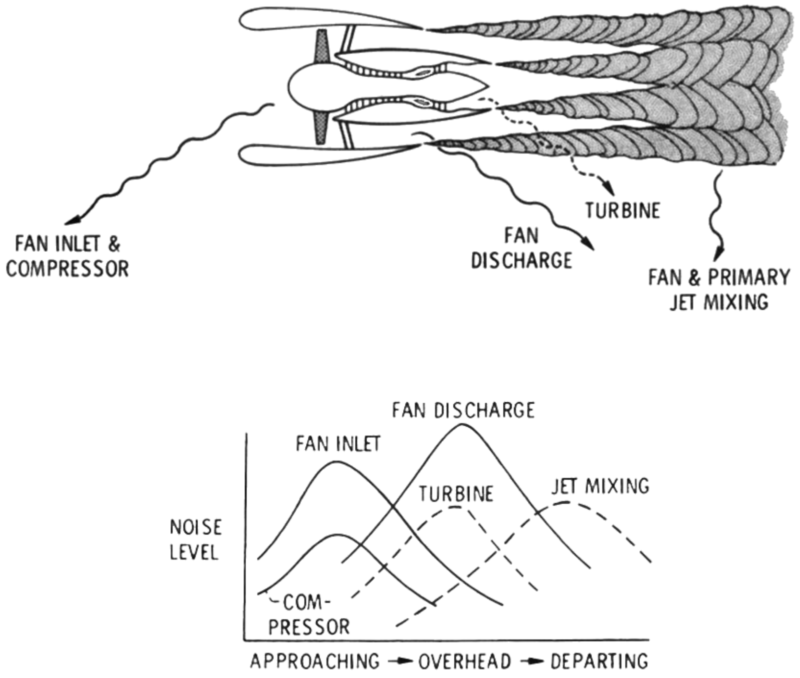

Figure 2. The major powerplant noise sources, where noise levels from the different sources is given. Picture taken from [13].

Even though jet-noise eventually has been reduced to a minimum, there are still problems in keeping the noise levels low during take-off and approach. From experiments (see e.g. [19]), it has been shown that fan noise intensity (i.e. noise generated by the blades/vanes in the compressor or turbine – often associated with turbulent wakes developed by rotor/stator) dominates over the jet noise intensity. This is a problem especially on approach, when the fan noise generated in the compressor radiates out of the ground-pointing engine inlet, see Figure 3 and 2. During take-off, on the other hand, jet noise is still the dominating part, but the duration of a take-off is often less than the duration of an approach, and therefore the total emitted sound is less, see Figure 2. This has directed the research to concentrate on how to reduce fan noise instead of further reducing jet noise.

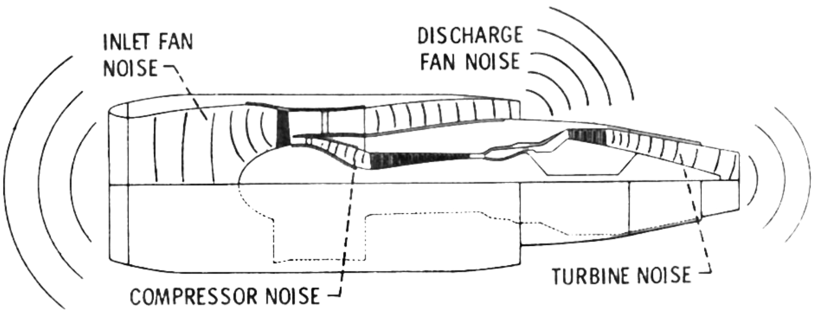

Figure 3. Phases in emission of fan noise. Picture taken from [13].

Fan noise is a complex process that involves strong directivity. Basically, fan noise is generated at the rotating blades (rotor) and stationary vanes (stator). This is a result of fluctuating blade surface pressure, which essentially arises due to unsteady inflow from turbulent free stream into a stage, and to airfoil wakes from upstream stages, see Figure 4. In addition, supersonic blade tip speeds will produce additional noise from the blade shock patterns that are generated. Summing up, it can easily be recognized as non-linear and complex aerodynamics rather than acoustic problem in nature. Furthermore, knowing that the sound origins from fluctuating forces, it can be identified as a dipole source (e.g. [7]), which radiates sound in two highly distinct directions.

In order to make estimates of the radiated sound power to the far-field (far away from the source, e.g. an observer on the ground relative an aircraft flying above, see Figure 5)

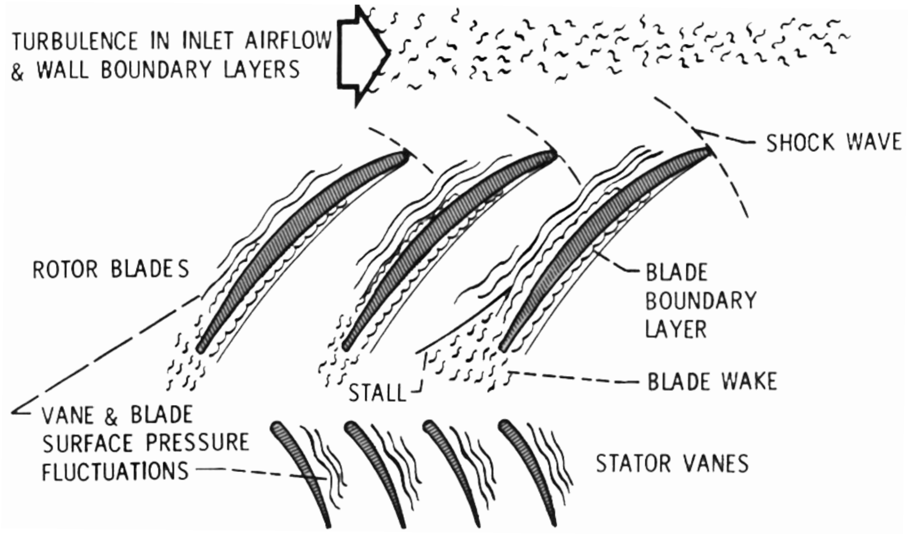

Figure 4. Broadband noise generation due to random blade load variation. Picture taken from [13].

the acoustic power generated by the non-linear process inside the engine to the near-field has to be calculated.

The difficulty in developing general analytical methods for the near-field, has made it necessary to use numerical methods. Using numerical computations (CFD) in aeroacoustics is at the present time very new. Since preserving sound waves convected by fluid motion in a numerical domain, without loss of information, requires a very high resolution to distinguish the wave solution from numerical errors. This has until the last few years, not been possible because of the need for extremely powerful computers.

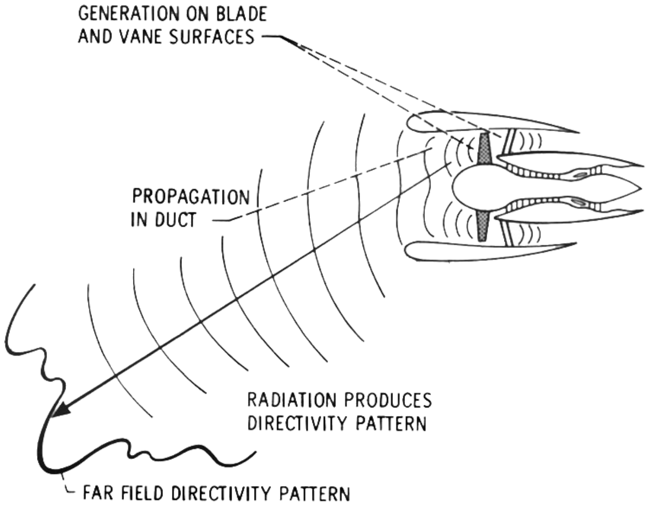

Figure 5. Phases in emission of fan noise. Picture taken from [13].

The main objective of this thesis is to numerically investigate how acoustic waves develops in a two-dimensional fan stage using the viscous Navier-Stokes equations. This is an initial study of a large EU-project called TurboNoiseCFD led by Rolls Royce, where the overall goal is to reduce fan-noise by optimizing the blade design.

By applying the well-established linear methods for aeroacoustics in a parallel wall-duct to the fan stage, one can obtain analytical expressions for the dispersion-relation – which is an important factor containing all the wave information to be preserved in space and time for ensuring good quality (see [23]). A sinusoidal acoustic wave with a known dispersion-relation is propagated thru a 2D numerical fan stage using a time-dependent finite-volume scheme in Euranus (see [15]). Solution is obtained by using a central scheme with artificial dissipation in space and a second-order implicit time-

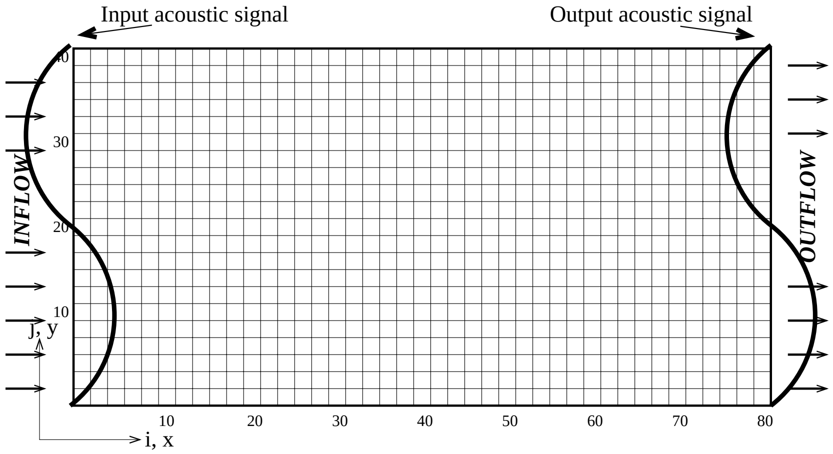

Figure 6. Numerical wave propagation in a 2D domain, which basically is the spacing between a rotor-rotor or a stator-stator, but very simplified. The numbers is x- and y-direction represent the node numbers. The acoustic input signal is simply a sinusoidal pressure variation in y-direction.

integration, in order to have A-stability. This numerical solution is then compared with the original wave to obtain deviations that could originate from dispersion, dissipation and boundary-condition (reflections) errors induced by the numerical boundaries. For this analysis, a method called wavesplitting is applied on the discrete points from the numerical solution, decomposing the flow field into upstream and downstream traveling waves (see [24]) explicitly decoding the analytical encoded dispersion-relation. From this, one can make a resolution requirement that diminishes the errors, and thus clarifies the real strength and weakness of CFD applied on aeroacoustics.

2 Governing equations

In this report, we consider a two-dimensional unsteady viscous compressible flow for which the Navier-Stokes equations are the governing equations. On conservation form, these are given by the continuity of mass transport

$$\frac{\partial \rho}{\partial t} + \nabla \cdot (\rho \mathbf{V}) = 0, \tag{1}$$

the momentum equation

$$\frac{\partial}{\partial t}(\rho \mathbf{V}) + \nabla \cdot (\rho \mathbf{V} \otimes \mathbf{V}) = -\nabla p + \nabla \cdot \bar{\bar{\tau}}^{\mathrm{v}}, \tag{2}$$

the energy equation

$$\frac{\partial}{\partial t}(\rho E) + \nabla \cdot (\rho E \mathbf{V}) = -\nabla \cdot (p\mathbf{V}) - \nabla \cdot \mathbf{q} + \nabla \cdot \left(\bar{\bar{\tau}}^{\mathrm{v}} \mathbf{V}\right), \tag{3}$$

and the equation of state

$$p = \rho R T. \tag{4}$$

Where $\otimes$ denotes the tensor product, $\mathbf{V} = [u \ v]^T$ is the velocity components, ρ the density, p the pressure, R the specific gas constant, $\mathbf{q} = -\kappa \nabla T$ the heat conduction flux often referred to as Fourier's law, and $E = e + \frac{1}{2}V^2$ is the total energy (internal plus kinematic). The viscosity is given by the two-dimensional Newtonian stress tensor matrix

$$\bar{\bar{\tau}}^{\mathrm{v}} = \begin{bmatrix} \tau_{xx}^{\mathrm{v}} & \tau_{xy}^{\mathrm{v}} \\ \tau_{yx}^{\mathrm{v}} & \tau_{yy}^{\mathrm{v}} \end{bmatrix} = \begin{bmatrix} 2\mu \frac{\partial u}{\partial x} - \frac{2}{3}\mu (\nabla \cdot \mathbf{V}) & \mu \left(\frac{\partial u}{\partial y} + \frac{\partial v}{\partial x}\right) \\ \mu \left(\frac{\partial u}{\partial y} + \frac{\partial v}{\partial x}\right) & 2\mu \frac{\partial v}{\partial y} - \frac{2}{3}\mu (\nabla \cdot \mathbf{V}) \end{bmatrix}$$

where μ is the fluid viscosity. In this report all body forces are neglected.

3 Aeroacoustic relations

Consider acoustic waves traveling in a two-dimensional duct with a constant cross section and carried by an external mean flow. This is applicable to e.g. turbine cascades, i.e. rotor-rotor or stator-stator spacing. The flow is considered adiabatic, as well as viscous contributions are neglected, which reduces the Navier-Stokes to the Euler equations. Written out in full, the continuity equation

$$\frac{\partial \rho}{\partial t} + \frac{\partial}{\partial x}(\rho u) + \frac{\partial}{\partial y}(\rho v) = 0, \tag{5}$$

the momentum equation parallel to the duct (x-momentum)

$$\frac{\partial u}{\partial t} + u\frac{\partial u}{\partial x} + v\frac{\partial u}{\partial y} = -\frac{1}{\rho}\frac{\partial p}{\partial x}, \tag{6}$$

and momentum equation for the cross-flow plane (y-momentum)

$$\frac{\partial v}{\partial t} + u\frac{\partial v}{\partial x} + v\frac{\partial v}{\partial y} = -\frac{1}{\rho}\frac{\partial p}{\partial y}. \tag{7}$$

For an acoustic disturbance in a calorical perfect gas, isentropic state conditions are valid

$$c^2 = \frac{\gamma p}{\rho} \tag{8}$$

where c is the speed of sound, and $\gamma = 1.4$.

3.1 Linearized problem formulation

We assume that each flow quantity consist of a parallel and uniform mean flow, i.e. $U_0 = const$, and a perturbated flow by the following

$$\begin{array}{ll} u = U_0 + u'(x,y,t) & p = p_0 + p'(x,y,t) \\ v = 0 + v'(x,y,t) & \rho = \rho_0 + \rho'(x,y,t) \end{array} \tag{9}$$

where $\mathcal{O}(U_0) \gg \mathcal{O}(u')$ etc., that is the perturbated components are small compared to the mean flow components. Inserting (9) into the Euler equations, Eq. (5)-(7), and linearizing by neglecting quadratic and higher order terms we obtain

$$\begin{array}{l} \frac{\partial \rho'}{\partial t} + U_0\frac{\partial \rho'}{\partial x} = -\rho_0 \nabla \cdot \mathbf{u}' \\ \frac{\partial \mathbf{u}'}{\partial t} + U_0\frac{\partial \mathbf{u}'}{\partial x} = -\frac{1}{\rho_0}\nabla p'. \end{array}$$

where $\mathbf{u}' = [u'\ v']^T$.

Expressing the density variation as pressure variation using

$$\frac{p}{p_0} = \left(\frac{\rho}{\rho_0}\right)^\gamma \text{ and } c^2 = \frac{\gamma p}{\rho}$$

yields the linearized Euler equations for an acoustic disturbance

$$\begin{array}{l} \frac{1}{c}\frac{\partial p^*}{\partial t} + M\frac{\partial p^*}{\partial x} = -\gamma \nabla \cdot \mathbf{u}^* \\ \frac{1}{c}\frac{\partial \mathbf{u}^*}{\partial t} + M\frac{\partial \mathbf{u}^*}{\partial x} = -\frac{1}{\gamma}\nabla p^* \end{array} . \tag{10}$$

Here M is the mean flow Mach number, and the non-dimensional perturbation values denoted with * is normalized by its mean flow components and the speed of sound, i.e. $p^* = \frac{p'}{p_0}$ and $\mathbf{u}^* = \frac{\mathbf{u}'}{c}$.

3.2 Duct transmission properties

The acoustic dispersion-relation is attained by Fourier transformation in time and y-direction, respectively, of the linearized equations, see [20]. Using (8) in (10) and reformulating to a matrix-system, one obtains

$$\frac{1}{c}\frac{\partial \mathbf{f}}{\partial t}+\frac{\partial \mathbf{g}}{\partial x}+\frac{\partial \mathbf{h}}{\partial y}=0 \tag{11}$$

where

$$\mathbf{f}=\begin{bmatrix} p \\ u \\ v \end{bmatrix}, \quad \mathbf{g}=\begin{bmatrix} Mp+\gamma u \\ Mu+\frac{1}{\gamma}p \\ Mv \end{bmatrix}, \quad \mathbf{h}=\begin{bmatrix} \gamma v \\ 0 \\ \frac{1}{\gamma}p \end{bmatrix}$$

and the * has been removed for simplicity.

By Fourier analysis the function $\mathbf{f}(x,y,t)$ can be represented by its harmonic elements

$$\mathbf{f}(x,y,t)=\iint_{-\infty}^{\infty}\hat{\mathbf{f}}(x,k_y,\omega)e^{-i(k_y y-\omega t)}\,\mathrm{d}k_y\,\mathrm{d}\omega \tag{12}$$

where $\hat{\mathbf{f}}(x,k_y,\omega)$ is the complex axial amplitude. After Fourier transforming Eq. (11), we have the following system of differential equations

$$\mathbf{A}\frac{\partial \hat{\mathbf{f}}}{\partial x}+\mathbf{B}\hat{\mathbf{f}}=0$$

or equivalently

$$\frac{\partial \hat{\mathbf{f}}}{\partial x}+\mathbf{A}^{-1}\mathbf{B}\hat{\mathbf{f}}=0 \tag{13}$$

where

$$\mathbf{A}=\begin{bmatrix} M & \gamma & 0 \\ \frac{1}{\gamma} & M & 0 \\ 0 & 0 & M \end{bmatrix}, \quad \mathbf{B}=\begin{bmatrix} i\tilde{\omega} & 0 & -i\gamma k_y \\ 0 & i\tilde{\omega} & 0 \\ -i\frac{1}{\gamma}k_y & 0 & i\tilde{\omega} \end{bmatrix}$$

and $\tilde{\omega}=\frac{\omega}{c}$. Let $\mathbf{L}$ be a matrix with the eigenvectors of the matrix $\mathbf{A}^{-1}\mathbf{B}$ as coloumns. Define $\mathbf{q}=\mathbf{L}^{-1}\widehat{\mathbf{f}}$. After multiplying Eq. (13) with $\mathbf{L}^{-1}$ we obtain the decoupled system of ordinary differential equations on the form

$$\frac{\partial \mathbf{q}}{\partial x}+\mathbf{\Lambda}\mathbf{q}=0 \tag{14}$$

where $\mathbf{q}$ is the decoupled flow variables and

$$\mathbf{\Lambda}=\begin{bmatrix} \lambda_{ds} & 0 & 0 \\ 0 & \lambda_{us} & 0 \\ 0 & 0 & \lambda_v \end{bmatrix}.$$

The eigenvalues of $\mathbf{A}^{-1}\mathbf{B}$ are found by solving

$$\det\left|\mathbf{A}^{-1}\mathbf{B}-\mathbf{\Lambda}\right|=0$$

yielding

$$\lambda_{ds}=i\frac{M\tilde{\omega}+\sqrt{\tilde{\omega}^2-k_y^2\left(1-M^2\right)}}{1-M^2} \tag{15}$$

$$\lambda_{us}=i\frac{M\tilde{\omega}-\sqrt{\tilde{\omega}^2-k_y^2\left(1-M^2\right)}}{1-M^2} \tag{16}$$

$$\lambda_v=i\frac{\tilde{\omega}}{M}. \tag{17}$$

The notion of the eigenvalues describes two physically different waves; *acoustic* and *vorticity* waves. The vorticity waves, denoted with subscript *v*, consist of velocity fluctuations only (zero pressure variation). The acoustics waves, denoted by subscript *ds* and *us* to represent downstream and upstream traveling waves respectively, involves on the other hand fluctuations in all physical variables. See [20] for a more detailed physical description of the different acoustic waves.

3.2.1 Cut-off ratio

The so-called *cut-off* ratio is defined as

$$\xi = \frac{\tilde{\omega}}{k_y\sqrt{1-M^2}}, \tag{18}$$

The cut-off ratio describes the damping of the wave in the axial direction. In this report we consider subsonic conditions, implying that $\sqrt{1-M^2} < 1$, and a hard-wall duct providing a real wavenumber k_y. Hence ξ is a real and positive value. By introducing the cut-off ratio into the acoustic eigenvalues (or axial wavenumbers) (15) and (16) we have that

$$\lambda_{ds,us} = ik_x^{ds,us} = i\frac{M\xi \pm \sqrt{\xi^2-1}}{\sqrt{1-M^2}}k_y, \tag{19}$$

where k_x is the axial wavenumber. For the vorticity waves

$$\lambda_v = ik_x^v = i\frac{k_y\xi\sqrt{1-M^2}}{M}. \tag{20}$$

From (19) and (14) it is obvious that axial damping of the waves take place when $\xi < 1$ since the real part of λ will be non-zero. Subsequently, this means that the modes having cut-off ratio less than one will decay downstream the engine duct and therefore not contribute in the far-field (this also holds for upstream traveling waves having a cut-off ratio less than one). Note that λ_v is always pure imaginary and hence the vorticity waves will be cut-on for all waves of ξ.

3.2.2 Wave splitting

To obtain the decoupled flow variables $\mathbf{q}$ from (14) as function of the variables p, u and v, we have to find the eigenvectors corresponding to the eigenvalues Eq. (15) - (17). Straightforward calculations yield that

$$\mathbf{l_{ds}} = \begin{bmatrix} 1 \\ -\frac{Mk_y^2+\tilde{\omega}\sqrt{\tilde{\omega}^2-k_y^2(1-M^2)}}{\gamma(k_y^2M^2+\tilde{\omega}^2)} \\ \frac{k_y\tilde{\omega}-M\sqrt{\tilde{\omega}^2-k_y^2(1-M^2)}}{\gamma(k_y^2M^2+\tilde{\omega}^2)} \end{bmatrix}$$

$$\mathbf{l_{us}} = \begin{bmatrix} 1 \\ -\frac{Mk_y^2-\tilde{\omega}\sqrt{\tilde{\omega}^2-k_y^2(1-M^2)}}{\gamma(k_y^2M^2+\tilde{\omega}^2)} \\ \frac{k_y\tilde{\omega}+M\sqrt{\tilde{\omega}^2-k_y^2(1-M^2)}}{\gamma(k_y^2M^2+\tilde{\omega}^2)} \end{bmatrix}$$

$$\mathbf{l_v} = \begin{bmatrix} 0 \\ -\frac{k_yM}{\tilde{\omega}} \\ 1 \end{bmatrix}.$$

The eigenvector matrix now becomes $\mathbf{L} = [\mathbf{l_{ds}}\ \ \mathbf{l_{us}}\ \ \mathbf{l_v}]$, where the inverse is

$$\mathbf{L}^{-1} = \begin{bmatrix} \frac{-1}{\gamma}\frac{\xi\sqrt{1-M^2}}{\xi^2(1-M^2)+M^2} & \frac{-\xi M\sqrt{1-M^2}}{\xi^2(1-M^2)+M^2} & \frac{\xi^2(1-M^2)}{\xi^2(1-M^2)+M^2} \\ \frac{1}{2} & \gamma\frac{\xi}{2\sqrt{\xi^2-1}} & \gamma\frac{M}{2\sqrt{(\xi^2-1)(1-M^2)}} \\ \frac{1}{2} & \gamma\frac{-\xi}{2\sqrt{\xi^2-1}} & \gamma\frac{-M}{2\sqrt{(\xi^2-1)(1-M^2)}} \end{bmatrix}.$$

The decoupled variables can now be found by $\mathbf{q} = \mathbf{L}^{-1}\hat{\mathbf{f}}$, or explicitly

$$q_{ds,us} = \frac{1}{2}\hat{p} \pm \gamma \frac{\xi}{2\sqrt{\xi^2 - 1}}\hat{u} \pm \gamma \frac{M}{2\sqrt{(\xi^2 - 1)(1 - M^2)}}\hat{v} \tag{21}$$

and similarly

$$q_v = \frac{-\xi\sqrt{1 - M^2}}{\xi^2(1 - M^2) + M^2}\left(\frac{1}{\gamma}\hat{p} + M\hat{u} - \xi\sqrt{1 - M^2}\hat{v}\right). \tag{22}$$

This method is called *wavesplitting* and is a method that is extensively used in this project. By applying this method, it is possible to obtain information on each of the decoupled variables separately.

4 Reynolds-averaged equation with eddy-viscosity

In this project, we solve the viscous Navier-Stokes equations with turbulence models, i.e. Reynolds-averaged equations numerically. In this section we give a brief introduction to this transformation and the turbulence model used.

Considering a turbulent flow field that can be decomposed into a mean and fluctuating part, i.e.

$$\phi = \overline{\phi} + \phi'$$

where $\overline{\phi}$ is any mean flow scalar that is obtained by turbulent time-averaging over a time T, the total flow field

$$\overline{\phi}(\mathbf{x}, t) = \frac{1}{T} \int_{-T/2}^{T/2} \phi(\mathbf{x}, t + \tau)\, \mathrm{d}\tau. \tag{23}$$

Also ϕ' is the fluctuating part, which by definition is zero when time-averaged, i.e. $\overline{\phi'} = 0$. Considering compressible flow, it is also necessary to define the density-weighted averaged through

$$\widetilde{\phi} = \frac{\overline{\rho\phi}}{\overline{\rho}} \tag{24}$$

with

$$\phi = \widetilde{\phi} + \phi'' \tag{25}$$

where $\overline{\rho\phi''} = 0$ by definition.

Returning to the governing equations Eq. (1) - (3) in Section 2, and substituting these averages into the flow variables of the Navier-Stokes equations, one obtains the Reynolds averaged equations of the mean flow, see [12]. The continuity of mass transport then becomes

$$\frac{\partial \overline{\rho}}{\partial t} + \nabla \cdot (\overline{\rho}\widetilde{\mathbf{V}}) = 0, \tag{26}$$

the momentum equation

$$\frac{\partial}{\partial t}\left(\overline{\rho}\widetilde{\mathbf{V}}\right) + \nabla \cdot \left(\overline{\rho}\widetilde{\mathbf{V}} \otimes \widetilde{\mathbf{V}}\right) = -\nabla \overline{p} + \nabla \cdot \left(\widetilde{\overline{\overline{\tau}}}^{\mathrm{v}} - \overline{\rho \mathbf{V}'' \otimes \mathbf{V}''}\right) \tag{27}$$

and the energy equation

$$\frac{\partial}{\partial t}(\overline{\rho}\widetilde{E}) + \nabla \cdot \left(\overline{\rho}\widetilde{E}\widetilde{\mathbf{V}}\right) = -\nabla \cdot (\overline{p}\widetilde{\mathbf{V}}) - \nabla \cdot \overline{\mathbf{q}} + \nabla \cdot \left[\left(\widetilde{\overline{\overline{\tau}}}^{\mathrm{v}} - \overline{\rho \mathbf{V}'' \otimes \mathbf{V}''}\right) \mathbf{V}\right]. \tag{28}$$

Here the term $-\overline{\rho \mathbf{V}'' \otimes \mathbf{V}''}$ is the so-called Reynolds stresses $\widetilde{\overline{\overline{\tau}}}^{\mathrm{r}}$, and is essentially the term containing the turbulent-contributing flow changes. It is highly non-linear and needs to be modeled. This term also represent the main difference between the Reynolds-averaged mean flow equation and the Navier-Stokes equation.

Furthermore, assuming that the Reynolds stresses can be expressed through an eddy viscosity model, following the Boussineq hypothesis:

$$\widetilde{\overline{\overline{\tau}}}^{\mathrm{r}} = \begin{bmatrix} 2\mu_T \frac{\partial \tilde{u}}{\partial x} - \frac{2}{3}\mu_T \left(\nabla \cdot \widetilde{\mathbf{V}}\right) - \frac{2}{3}\overline{\rho}K & \mu_T \left(\frac{\partial \tilde{u}}{\partial y} + \frac{\partial \tilde{v}}{\partial x}\right) \\ \mu_T \left(\frac{\partial \tilde{u}}{\partial y} + \frac{\partial \tilde{v}}{\partial x}\right) & 2\mu_T \frac{\partial \tilde{v}}{\partial y} - \frac{2}{3}\mu_T \left(\nabla \cdot \widetilde{\mathbf{V}}\right) - \frac{2}{3}\overline{\rho}K \end{bmatrix} \tag{29}$$

where μ_T is the turbulent viscosity (a property of the flow, not the fluid), and

$$K = \frac{1}{2\overline{\rho}}\left(\overline{\rho u'' u''} + \overline{\rho v'' v''}\right) \tag{30}$$

is the kinetic energy of the turbulent vortices (eddies).

Substituting the eddy-viscosity assumption Eq. (29) into Eq. (26) - (28) we obtain a matrix system splitted into an inviscid and a viscous flux part in conservation form (see [10])

$$\frac{\partial \mathbf{U}}{\partial t} + \nabla \cdot \tilde{\mathbf{F}}_{\mathbf{I}} - \nabla \cdot \tilde{\mathbf{F}}_{\mathbf{V}} = \mathbf{Q} \tag{31}$$

where $\mathbf{Q} = \mathbf{0}$ since all body forces are neglected. $\tilde{\mathbf{F}}_{\mathbf{I}} = [\mathbf{f}_{\mathbf{I}},\ \mathbf{g}_{\mathbf{I}}]$ and $\tilde{\mathbf{F}}_{\mathbf{V}} = [\mathbf{f}_{\mathbf{V}},\ \mathbf{g}_{\mathbf{V}}]$ are the inviscid and viscous fluxes respectively

$$\mathbf{U} = \begin{bmatrix} \overline{\rho} \\ \overline{\rho}\widetilde{u} \\ \overline{\rho}\widetilde{v} \\ \overline{\rho}\widetilde{E} \end{bmatrix}, \ \mathbf{f}_{\mathbf{I}} = \begin{bmatrix} \overline{\rho}\widetilde{u} \\ \overline{\rho}\widetilde{u}\widetilde{u} + \overline{P} \\ \overline{\rho}\widetilde{u}\widetilde{v} \\ (\overline{\rho}\widetilde{E} + \overline{P})\widetilde{u} \end{bmatrix}, \ \mathbf{g}_{\mathbf{I}} = \begin{bmatrix} \overline{\rho}\widetilde{v} \\ \overline{\rho}\widetilde{v}\widetilde{u} \\ \overline{\rho}\widetilde{v}\widetilde{v} + \overline{P} \\ (\overline{\rho}\widetilde{E} + \overline{P})\widetilde{v} \end{bmatrix},$$

$$\mathbf{f}_{\mathbf{V}} = \begin{bmatrix} 0 \\ \widetilde{\tau}_{xx} \\ \widetilde{\tau}_{xy} \\ (\kappa + \kappa_T)\frac{\partial \overline{T}}{\partial x} + \widetilde{\tau}_{xx}\widetilde{u} + \widetilde{\tau}_{xy}\widetilde{v} + \left(\mu + \frac{\mu_T}{\sigma_k}\right) K \end{bmatrix},$$

$$\mathbf{g}_{\mathbf{V}} = \begin{bmatrix} 0 \\ \widetilde{\tau}_{yx} \\ \widetilde{\tau}_{yy} \\ (\kappa + \kappa_T)\frac{\partial \overline{T}}{\partial y} + \widetilde{\tau}_{yx}\widetilde{u} + \widetilde{\tau}_{yy}\widetilde{v} + \left(\mu + \frac{\mu_T}{\sigma_k}\right) K \end{bmatrix}.$$

Here the turbulent stresses are added to the viscous stresses to give $\widetilde{\overline{\overline{\tau}}} = \widetilde{\overline{\overline{\tau}}}^{\mathrm{v}} + \widetilde{\overline{\overline{\tau}}}^{\mathrm{r}}$, the pressure containing the kinetic energy from turbulence are defined as $\overline{P} = \overline{p} + \frac{2}{3}\overline{\rho}K$, σ_k the Schmidt number (a constant found by turbulence model calibration), the thermal and turbulent conductivity constants are defined as $\kappa = \frac{\mu c_p}{Pr}$ and $\kappa_T = \frac{\mu_T c_p}{Pr_T}$ respectively where c_p is the specific heat at constant pressure and Pr is the Prandtl number.

4.1 The Wilcox standard $K - \omega$ turbulence model

As mentioned in the previous section, the Reynolds stress tensor represents a highly non-linear term and will therefore involve extremely huge computational efforts to calculate exactly. To reduce the amount of needed computer power, this term was substituted with an eddy-viscosity model. This behaves in the same way as fluid viscosity, except that the turbulent viscosity factor μ_T is not a constant, and needs to be resolved for each position in the flow field. To retain closure, two simple equations are introduced; one for the kinetic energy K and one for the angular velocity ω of the eddies. This is referred to as the Wilcox standard $K - \omega$ turbulence model, which will be briefly presented here, for full description see e.g. [12].

Since μ_T is not a constant, it has to be calculated for each position in the flow field. The following eddy-viscosity relation holds

$$\mu_T = \overline{\rho}\frac{K}{\omega} \tag{32}$$

and

$$\omega = \frac{\epsilon}{\beta K} \tag{33}$$

where ϵ is the dissipation of energy by the small eddies, and β is a calibration constant. To obtain a value for μ_T in (32) it is obvious that one has to calculate K and ω first.

Introducing the K-equation, which basically is the equation of the fluctuating velocity in (25) transformed into kinetic energy by (30)

$$\frac{\partial}{\partial t}(\overline{\rho}K) + \nabla \cdot \left(\overline{\rho}K\widetilde{\mathbf{V}}\right) = \nabla \cdot \left[\left(\mu + \frac{\mu_T}{\sigma_k}\right)\nabla K\right] + \left(\widetilde{\overline{\overline{\tau}}}^{\mathrm{r}} \cdot \nabla\right) \cdot \widetilde{\mathbf{V}} - \overline{\rho}\epsilon. \tag{34}$$

The first term on the right-hand side is the diffusion term, while the second term is the production of turbulent energy, often denoted by $\mathcal{P}$, done by the work of the mean flow against the Reynolds stress $\widetilde{\overline{\overline{\tau}}}^{\,\mathrm{r}}$. The last term is the dissipation given by ϵ in (33).

To have closure, the ω-equation is introduced as the auxiliary quantity, which is the modeled equation and therefore also the major weakness of this and other two-equation turbulence models

$$\frac{\partial}{\partial t}\left(\overline{\rho}\omega\right) + \nabla \cdot \left(\overline{\rho}\omega\widetilde{\mathbf{V}}\right) = \nabla \cdot \left[\left(\mu + \frac{\mu_T}{\sigma_k^*}\right)\nabla\omega\right] + \gamma^* \frac{\omega}{K}\left(\widetilde{\overline{\overline{\tau}}}^{\,\mathrm{r}} \cdot \nabla\right) \cdot \widetilde{\mathbf{V}} - \beta^*\overline{\rho}\omega^2.$$

This equation contains factors that are experimentally obtained. These may change from different flow cases and calibration methods, but here the following “standard” values are used

$$\gamma^* = 0.556,\ \ \beta = 0.075,\ \ \beta^* = 0.09,\ \ \sigma_k = 2,\ \ \sigma_k^* = 2.$$

Representing the K- and the ω-equation in a matrix system compatible with (31)

$$\frac{\partial \mathbf{U}^{(\mathbf{T})}}{\partial t} + \nabla \cdot \tilde{\mathbf{F}}_{\mathbf{I}}^{(\mathbf{T})} - \nabla \cdot \tilde{\mathbf{F}}_{\mathbf{V}}^{(\mathbf{T})} = \mathbf{Q}^{(\mathbf{T})} \tag{35}$$

where the inviscid and viscous fluxes together with the source term are given by

$$\mathbf{U}^{(\mathbf{T})} = \begin{bmatrix} \overline{\rho}K \\ \overline{\rho}\omega \end{bmatrix},\ \ \mathbf{f}_{\mathbf{I}} = \begin{bmatrix} \overline{\rho}K\widetilde{u} \\ \overline{\rho}\omega\widetilde{u} \end{bmatrix},\ \ \mathbf{g}_{\mathbf{I}}^{(\mathbf{T})} = \begin{bmatrix} \overline{\rho}K\widetilde{v} \\ \overline{\rho}\omega\widetilde{v} \end{bmatrix},$$

$$\mathbf{f}_{\mathbf{V}}^{(\mathbf{T})} = \begin{bmatrix} \left(\mu + \frac{\mu_T}{\sigma_k}\right)\frac{\partial K}{\partial x} \\ \left(\mu + \frac{\mu_T}{\sigma_k^*}\right)\frac{\partial \omega}{\partial x} \end{bmatrix},\ \ \mathbf{g}_{\mathbf{V}}^{(\mathbf{T})} = \begin{bmatrix} \left(\mu + \frac{\mu_T}{\sigma_k}\right)\frac{\partial K}{\partial y} \\ \left(\mu + \frac{\mu_T}{\sigma_k^*}\right)\frac{\partial \omega}{\partial y} \end{bmatrix}$$

$$\mathbf{Q}^{(\mathbf{T})} = \begin{bmatrix} \left(\widetilde{\overline{\overline{\tau}}}^{\,\mathrm{r}} \cdot \nabla\right) \cdot \widetilde{\mathbf{V}} - \overline{\rho}\epsilon \\ \gamma^* \frac{\omega}{K}\left(\widetilde{\overline{\overline{\tau}}}^{\,\mathrm{r}} \cdot \nabla\right) \cdot \widetilde{\mathbf{V}} - \beta^*\overline{\rho}\omega^2 \end{bmatrix}.$$

5 Spatial discretization

5.1 Mean flow equations

The mean flow equations (31) and (35) are discretized using a cell-centered Finite Volume method. In order to do the discretization it is necessary formulate the equations on integral form

$$\int_\Omega \frac{\partial \mathbf{U}}{\partial t}\,\mathrm{d}\Omega + \int_\Omega \nabla\cdot\tilde{\mathbf{F}}_\mathbf{I}\,\mathrm{d}\Omega - \int_\Omega \nabla\cdot\tilde{\mathbf{F}}_\mathbf{V}\,\mathrm{d}\Omega = \int_\Omega \mathbf{Q}\,\mathrm{d}\Omega$$

where Ω is the volume of integration. Furthermore, by using Gauss' theorem at a vector $\tilde{\mathbf{F}}$

$$\int_\Omega \nabla\cdot\tilde{\mathbf{F}}\,\mathrm{d}\Omega = \oint_S \tilde{\mathbf{F}}\cdot\mathrm{d}\mathbf{S}$$

Here $\mathbf{S} = S\mathbf{e}$ is the surface of the integration volume Ω-faces with the projection $\mathbf{e}$. With this, one can transform the volume integral of the inviscid and viscous fluxes into surface integrals

$$\frac{\partial}{\partial t}\int_\Omega \mathbf{U}\,\mathrm{d}\Omega + \oint_S \tilde{\mathbf{F}}_\mathbf{I}\cdot\mathrm{d}\mathbf{S} - \oint_S \tilde{\mathbf{F}}_\mathbf{V}\cdot\mathrm{d}\mathbf{S} = \int_\Omega \mathbf{Q}\,\mathrm{d}\Omega. \tag{36}$$

In this report, we use the so-called *method of lines*, that is the time and space discretization has been separated. The time integration is described in Section 6

Equation (36) is replaced by the spatial discrete form for a finite volume in two dimensions

$$\frac{\partial \mathbf{U}_{ij}}{\partial t}\,\Omega_{ij} + \sum_{\text{sides}}(\tilde{\mathbf{F}}_\mathbf{I}\cdot\boldsymbol{\Delta}\mathbf{S})_{ij} - \sum_{\text{sides}}(\tilde{\mathbf{F}}_\mathbf{V}\cdot\Delta\mathbf{S})_{ij} = \mathbf{Q}_{ij}\,\Omega_{ij}, \tag{37}$$

The computations are performed on a structured orthogonal grid (as in Figure 7 and 12), which then simply gives that $\Omega_{ij} = \Delta x\Delta y$. Written out in full, both the summation terms in (37) takes the general form in two dimensions (see Figure 7) as

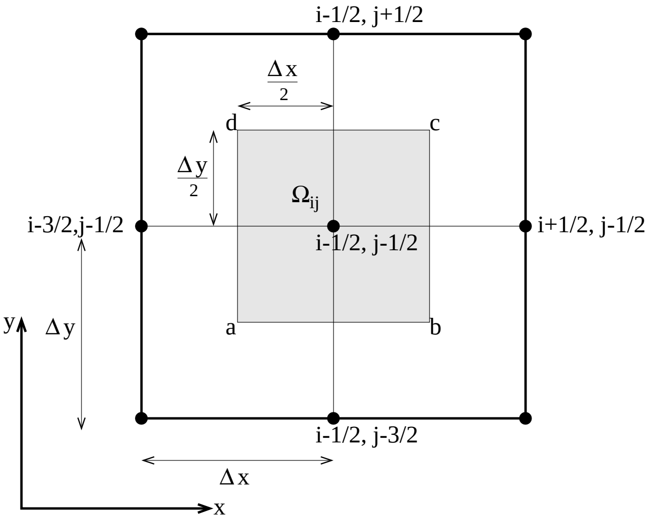

Figure 7. Two dimensional cell centered finite volume, with the computational box is defined within the box a-b-c-d.

$$\begin{aligned}\sum_{\text{sides}}(\tilde{\mathbf{F}}\cdot\boldsymbol{\Delta}\mathbf{S}) =& \mathbf{f}_{ab}(y_b-y_a) + \mathbf{f}_{bc}(y_c-y_b) + \mathbf{f}_{cd}(y_d-y_c) + \mathbf{f}_{da}(y_a-y_d) + \\ &+ \mathbf{g}_{ab}(x_b-x_a) + \mathbf{g}_{bc}(x_c-x_b) + \mathbf{g}_{cd}(x_d-x_c) + \mathbf{g}_{da}(x_a-x_d).\end{aligned}$$

where the fluxes are given on the cell faces in Ω_{IJ}. Since the calculations are carried out on a structured grid, and the major part of the calculations are performed with orthogonal mesh rectangles (see Section 8 for exceptions), the previous formula reduces to

$$\sum_{\text{sides}} (\tilde{\mathbf{F}} \cdot \mathbf{\Delta S}) = \mathbf{f}_{i+1/2,j}\Delta y - \mathbf{f}_{i-1/2,j}\Delta y + \mathbf{g}_{i,j+1/2}\Delta x - \mathbf{g}_{i,j-1/2}\Delta x, \tag{38}$$

writing $\mathbf{f}_{da} = \mathbf{f}_{i-1/2,j} = \mathbf{f}(\mathbf{U}_{i-1/2,j})$ and similarly for the other components. By using (38) in (37) one further reduces to a cell-centered finite difference formulation

$$\frac{\partial \mathbf{U}_{i,j}}{\partial t} = -\left[\frac{\mathbf{f}_{i+1/2,j} - \mathbf{f}_{i-1/2,j}}{\Delta x} + \frac{\mathbf{g}_{i,j+1/2} - \mathbf{g}_{i,j-1/2}}{\Delta y}\right]_{\mathbf{I}} + \left[\frac{\mathbf{f}_{i+1/2,j} - \mathbf{f}_{i-1/2,j}}{\Delta x} + \frac{\mathbf{g}_{i,j+1/2} - \mathbf{g}_{i,j-1/2}}{\Delta y}\right]_{\mathbf{V}} + \mathbf{Q}_{ij}, \tag{39}$$

which is second-order accurate in the half-cells.

5.1.1 Viscous fluxes

The viscous fluxes contain gradients of the velocity field that has to be evaluated on the cell-faces. To illustrate how the gradients are evaluated, e.g. by taking the third component, $\widetilde{\tau}_{xy}$, of the viscous flux $\mathbf{f_V}$ in (31)

$$\widetilde{\tau}_{xy} = \mu_T \left(\frac{\partial \widetilde{u}}{\partial y} + \frac{\partial \widetilde{v}}{\partial x}\right)$$

and discretize this using an central difference around the half-cell face, point $i - 1/2, j$, one obtains

$$\begin{aligned} \mu_T \left(\frac{\partial \widetilde{v}}{\partial x}\right)_{i-1/2,j} &\simeq \mu_T \left(\frac{\widetilde{v}_{i-1,j} - \widetilde{v}_{i,j}}{\Delta x}\right) \\ \mu_T \left(\frac{\partial \widetilde{u}}{\partial y}\right)_{i-1/2,j} &\simeq \mu_T \frac{1}{2}\left(\frac{\widetilde{u}_{i-1,j+1} - \widetilde{u}_{i-1,j-1}}{2\Delta y} + \frac{\widetilde{u}_{i,j+1} - \widetilde{u}_{i,j-1}}{2\Delta y}\right), \end{aligned}$$

which is second-order in the half-cell faces.

In general, there are ways of making the gradient more exactly calculated. By for instance instead using weighted averaging or averages of gradients calculated in each neighbor cell point. In this project these are of little interest, as the extra expenses will not improve the results much on a structured orthogonal mesh.

5.1.2 Inviscid fluxes

The inviscid fluxes, on the other hand, suffer from stability problems when discretized as a second-order method like the central differences. To avoid these problems, a so-called artificial viscosity term is subtracted from the fluxes in (39)

$$\mathbf{f}^{(AV)}_{i-1/2,j} = \mathbf{f}_{i-1/2,j} - d_{i-1/2,j}, \tag{40}$$

which will introduce dissipation into the solution and damp the oscillations that occur when strong gradient are present from the odd-even decoupling (see both Figure 8 and appendix A for a description). The physical flux $\mathbf{f}_{i-1/2,j}$ is calculated by averaging the flux to the right and left of the half-cell

$$\mathbf{f}_{i-1/2,j} = \frac{1}{2}(\mathbf{f}_{i-1,j} + \mathbf{f}_{i,j}).$$

The artificial viscosity term $d_{i-1/2,j}$ is on the form

$$d_{i-1/2,j} = \epsilon^{(2)}_{i-1/2,j}(\mathbf{U}_{i,j} - \mathbf{U}_{i-1,j}) - \epsilon^{(4)}_{i-1/2,j}(\mathbf{U}_{i+1,j} - 3\mathbf{U}_{i,j} + 3\mathbf{U}_{i-1,j} - \mathbf{U}_{i-1,j})$$

Figure 8. Illustration of the development of the dispersion error near discontinuities. Using Lax-Wendroff method to the inviscid Burgers equation. $\Delta t/\Delta x = 0.25$ after 200 time steps.

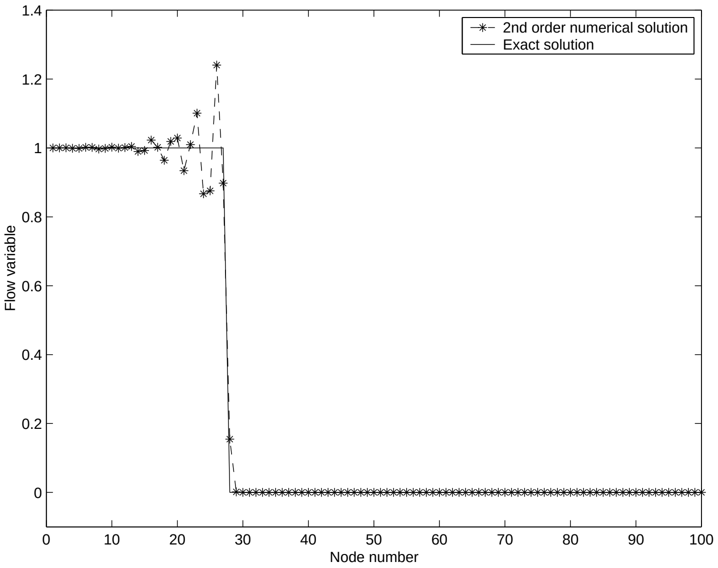

and is called the Jamesson artificial dissipation, see [11]. The terms $\epsilon^{(2)}_{i-1/2,j}$ and $\epsilon^{(4)}_{i-1/2,j}$ are evaluated as

$$\epsilon^{(2)}_{i-1/2,j} = \frac{1}{2}\sigma^{(2)}\lambda^*_{i-1/2,j}\max(\nu_{i-2,j},\nu_{i-1,j},\nu_{i,j},\nu_{i+1,j}) \tag{41}$$

and

$$\epsilon^{(4)}_{i-1/2,j} = \max\left(0, \frac{1}{2}\sigma^{(4)}\lambda^*_{i-1/2,j} - \epsilon^{(2)}_{i-1/2,j}\right) \tag{42}$$

respectively. The $\nu_{i,j}$ is a measure of the change in gradients, e.g. discontinuities. Here the pressure is used as a sensor for the amount of second-order dissipation to be activated when strong gradient appear

$$\nu_{i,j} = \left|\frac{p_{i+1,j} - 2p_{i,j} + p_{i-1,j}}{p_{i+1,j} + 2p_{i,j} + p_{i-1,j}}\right|. \tag{43}$$

Hence, the spectral radii λ^* is a measure of the inviscid fluxes that is calculated using

$$\lambda^*_{i-1/2,j} = \left(\vec{u}\Delta\vec{S} + c\Delta S\right)_{i-1/2,j}$$

and similar for j-direction. For the i-direction, cell face normal $\Delta\vec{S}$ is obtained by averaging the normals on the 4 cell faces in the i-direction, belonging to the 2 cells which share the $j - 1/2$ cell face.

The goal of the artificial viscosity parameters is to retain second-order accuracy, except in regions of strong pressure gradients, where it reduces to first-order – and where $\epsilon^{(2)}$ then becomes the dominating part. Moreover, in smooth regions small oscillations can also occur. These oscillations are controlled and damped with the $\epsilon^{(4)}$, which is proportional to a third-order difference and is, in the same way as $\epsilon^{(2)}$, only introduced when large gradient are apparent.

To scale the amount of added artificial viscosity, the constants $\sigma^{(2)}$ and $\sigma^{(4)}$ can be manually adjusted. In principle, since the artificial viscosity introduces non-physical dissipation into the solution one wants to minimize this amount. By fine-tuning these constant one can obtain an oscillation-free solution with as little artificial viscosity as possible.

5.2 Turbulence equations

Equivalent to the discretization of the mean flow equations, the turbulence equations are also discretized using central differences for both the inviscid and viscous fluxes. Obtaining, similar to (39)

$$\frac{\partial \mathbf{U}_{i,j}^{(\mathbf{T})}}{\partial t} = -\left[\frac{\mathbf{f}_{i+1/2,j} - \mathbf{f}_{i-1/2,j}}{\Delta x} + \frac{\mathbf{g}_{i,j+1/2} - \mathbf{g}_{i,j-1/2}}{\Delta y}\right]_{\mathbf{I}}^{(\mathbf{T})} + \left[\frac{\mathbf{f}_{i+1/2,j} - \mathbf{f}_{i-1/2,j}}{\Delta x} + \frac{\mathbf{g}_{i,j+1/2} - \mathbf{g}_{i,j-1/2}}{\Delta y}\right]_{\mathbf{V}}^{(\mathbf{T})} + \mathbf{Q}_{ij}^{(\mathbf{T})}. \tag{44}$$

The turbulent viscous fluxes are evaluated in the same manner as the mean flow viscous fluxes. However, the artificial viscosity of the turbulent inviscid fluxes are slightly different evaluated than the artificial viscosity of the mean flow inviscid fluxes. The difference lies in how the sensor for steep gradients is calculated. Instead of using pressure (43), one uses the turbulent kinetic energy

$$\nu_{i,j}^{(\mathbf{T})} = \left|\frac{K_{i+1,j} - 2K_{i,j} + K_{i-1,j}}{K_{i+1,j} + 2K_{i,j} + K_{i-1,j}}\right|.$$

Similar as for the mean flow adjustable parameters $\sigma^{(2)}$ and $\sigma^{(4)}$, one now has $\kappa^{(2)}$ and $\kappa^{(4)}$ to adjust.

To do separate computations on the mean flow and turbulence equations is not an obvious choice, but it has been proved to be necessary since instabilities could occur in for instance regions of turbulent flow while the mean flow is stable. This makes the model accurate.

6 Time integration

The time integration is divided into local and global time stepping. By having an implicit global time marching with local explicit subiterations, one can assure convergence in the time domain calculations.

When implicit time integration is used, a local time step within each global time step is used. Considering Eq. (39)

$$\begin{aligned}\frac{\partial \mathbf{U}_{i,j}}{\partial t}+\left[\frac{\mathbf{f}_{i+1/2,j}-\mathbf{f}_{i-1/2,j}}{\Delta x}-\frac{\mathbf{g}_{i,j+1/2}-\mathbf{g}_{i,j-1/2}}{\Delta y}\right]_{\mathbf{I}}-\\ \left[\frac{\mathbf{f}_{i+1/2,j}-\mathbf{f}_{i-1/2,j}}{\Delta x}+\frac{\mathbf{g}_{i,j+1/2}-\mathbf{g}_{i,j-1/2}}{\Delta y}\right]_{\mathbf{V}}-\mathbf{Q}_{ij}=\mathbf{0},\end{aligned} \tag{45}$$

which is discretized in time using $\mathbf{U}=\mathbf{U}_{i,j}$, and imposes a residual in each local time step

$$\mathbf{R}^*(\mathbf{U}^{n+1})=\frac{\beta_1\left(\Omega\mathbf{U}\right)^{n+1}+\beta_0\left(\Omega\mathbf{U}\right)^{n}+\beta_{-1}\left(\Omega\mathbf{U}\right)^{n-1}}{\Delta t}+\mathbf{R}\left(\mathbf{U}^{n+1}\right) \tag{46}$$

where $\mathbf{R}$ is the spatial discretization in (45), $\mathbf{R}^*$ is the residual after time-discretization, Ω_{ij} is the finite volume, and Δt is the global time step. The constants β_1, β_0 and β_{-1} are chosen as 1.5, -2 and 0.5 respectively, yielding a second-order accurate backward difference scheme that is A-stable. Introducing a pseudo time τ with the time dependent variables $\mathbf{U}(\tau)=\mathbf{U}^{n+1}$ to give the equation

$$\Omega_{ij}\frac{\mathrm{d}}{\mathrm{d}\tau}\mathbf{U}(\tau)+\mathbf{R}^*\left(\mathbf{U}(\tau)\right)=\mathbf{0}. \tag{47}$$

A steady state of the above equation is reached when the pseudo time-derivative approaches zero

$$\frac{\mathrm{d}}{\mathrm{d}\tau}\mathbf{U}(\tau)\to\mathbf{0}\Rightarrow\mathbf{U}^{n+1}=\mathbf{U}^{n}. \tag{48}$$

Hence, the equations reache a steady state in each global time step to give time-accuracy. For each of the local time step an explicit Runge-Kutta method is used, see section 6.1.

6.1 Explicit Runge-Kutta

Basically, the Runge-Kutta method is to evaluate the spatial discretization at several values of $\mathbf{U}$ in the interval between $n\Delta t$ and $(n+1)\Delta t$ to combine them in order to obtain a high-order approximation of $\mathbf{U}^{n+1}$. The explicit five-stage Runge-Kutta method for the equation (47) written on the form

$$\frac{\mathrm{d}}{\mathrm{d}\tau}\mathbf{U}=\tilde{\mathbf{F}}\left(\mathbf{U}\right) \tag{49}$$

now becomes

$$\mathbf{U}^{(1)}=\mathbf{U}^{n}+\alpha_1\Delta\tau\tilde{\mathbf{F}}(\mathbf{U}^{n}) \tag{50}$$

$$\mathbf{U}^{(2)}=\mathbf{U}^{n}+\alpha_2\Delta\tau\tilde{\mathbf{F}}(\mathbf{U}^{(1)}) \tag{51}$$

$$\ldots. \tag{52}$$

$$\mathbf{U}^{(5)}=\mathbf{U}^{n}+\alpha_5\Delta\tau\tilde{\mathbf{F}}(\mathbf{U}^{(4)}) \tag{53}$$

where

$$\mathbf{U}^{(5)}=\mathbf{U}^{n+1}. \tag{54}$$

The coefficients α_1 to α_5 determine the stability area and the order of accuracy of the Runge-Kutta scheme, respectively. They are here chosen to be .0814, .191, .342, .574 and 1, respectively.

To obtain a local time step for the Runge-Kutta method, the so-called CFL number is used. The CFL number (from Courant, Friedrichs, and Lewy's report issued in 1928) defines a ratio between the time step and the spatial step. From a stability analysis point of view, the CFL number gives important information on when the scheme is stable. Therefore, instead of pre-defining a time step, one obtains this by knowing the grid size and CFL number. In each cell a local inviscid and viscous local time step is calculated from

$$\Delta\tau_I = \frac{\Omega(\mathrm{CFL})_I}{\left|\vec{u}\vec{S}_i\right| + \left|\vec{u}\vec{S}_j\right| + c\left(\left|\vec{S}_i\right| + \left|\vec{S}_j\right|\right)} \tag{55}$$

and

$$\Delta\tau_V = \frac{\Omega^2\rho(\mathrm{CFL})_V}{8\mu\left(\left|\vec{S}_i\right|^2 + \left|\vec{S}_j\right|^2 + 2\left|\vec{S}_i\vec{S}_j\right|\right)} \tag{56}$$

respectively. The actual local time step is then the minimum of both these time steps

$$\Delta\tau = \min\left(\Delta\tau_I, \Delta\tau_V\right). \tag{57}$$

7 Boundary conditions

In order to correctly impose boundary conditions on the numerical domain it is important to know how information propagates. It is possible to explicitly obtain this information by calculating the eigenvalues of the entire system represented by the so-called characteristics.

In this section only a brief analysis will be done. Simplifying using only the mean flow of Reynolds-average equations in conservative form Eq. (31) with $\tilde{\mathbf{F}} = \tilde{\mathbf{F}}_{\mathbf{I}} - \tilde{\mathbf{F}}_{\mathbf{V}}$

$$\frac{\partial \mathbf{U}}{\partial t} + \nabla \cdot \tilde{\mathbf{F}} = \mathbf{Q},$$

which is rewritten into non-conservative form

$$\frac{\partial \mathbf{U}}{\partial t} + (\tilde{\mathbf{A}} \cdot \nabla)\mathbf{U} = \mathbf{Q} \tag{58}$$

where $\tilde{\mathbf{A}} = \frac{\partial \vec{F}}{\partial U}$ is the Jacobian of the system and $\tilde{\mathbf{A}} = [\mathbf{B} \;\; \mathbf{C}]^T$. Written out to

$$\frac{\partial \mathbf{U}}{\partial t} + \mathbf{B}\frac{\partial \mathbf{U}}{\partial x} + \mathbf{C}\frac{\partial \mathbf{U}}{\partial y} = \mathbf{Q}.$$

Furthermore, since it is obvious that the Jacobi matrix involves directivity one can express this as a scalar $\mathbf{K} = \tilde{\mathbf{A}} \cdot \vec{l}_n = \mathbf{B} \cdot \hat{n}_x + \mathbf{C} \cdot \hat{n}_y$, where $\vec{l}_n$ is the unit vector normal to the surface and $(\hat{n}_x, \; \hat{n}_y)$ is the components.

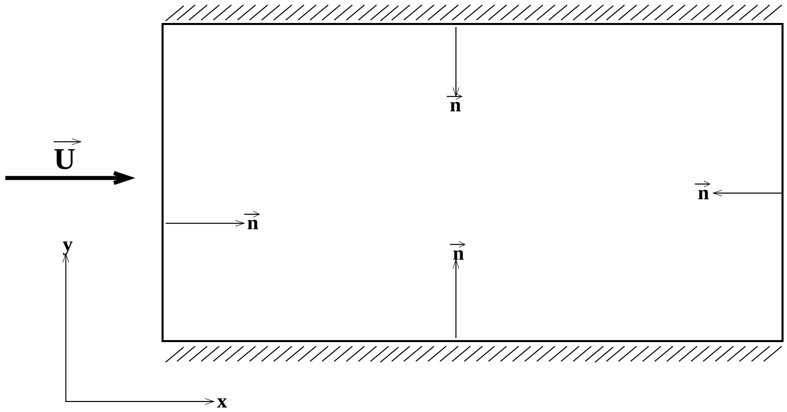

Figure 9. Boundaries of the domain.

Finding the eigenvalues of K as

$$\det\left|\tilde{\mathbf{A}} \cdot \vec{l}_n - \lambda \mathbf{I}\right| = 0 \tag{59}$$

provides information of characteristic propagation of the system of equation. If all eigenvalues are real, the equations is classified as *hyperbolic*, and when the eigenvalues contains imaginary values the equations are classified as *elliptic*. This describes two physically different states of information propagation (for a detailed description see [1]), which is an important condition when considering the choice of numerical scheme and boundary condition.

For subsonic flow, the four eigenvalues of Eq. (59) are all real, where three of them are positive and one negative. This implies that the system is hyperbolic.

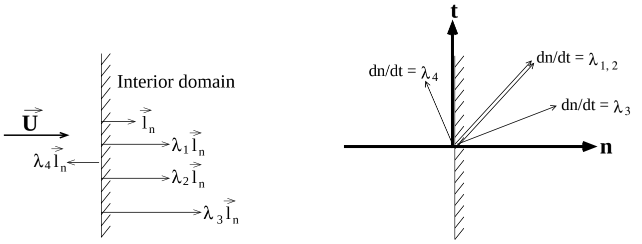

Figure 10. Illustration of how the eigenvalues λ_1 to λ_4 defines the information propagation. λ_1 to λ_3 are positive, but λ_4 is negative.

Hence, only variables or information transported from the boundaries towards the interior can be imposed at the boundaries as physical boundary conditions (referring to Figure 10). The remaining variables will depend on the computed flow situation and are therefore a part of the solution. See [14] for a detailed analysis.

7.1 Inflow boundary condition

A total number of six inflow boundary conditions must be applied, where five of them are physical and one is numerical. The physical boundary conditions are given by the velocity vector $\mathbf{V}_0$, the absolute total pressure p_0, the absolute total temperature T_0, the turbulent kinetic energy K_0, and the turbulent dissipation ϵ_0. The following default values are used

$$\begin{aligned} \mathbf{V}_0 &= \begin{bmatrix} u_0 \\ v_0 \end{bmatrix} = \begin{bmatrix} 136 \\ 0 \end{bmatrix} \text{ m/s} \\ p_0 &= 1.01 \cdot 10^5 \text{ Pa} \\ T_0 &= 288 \text{ K} \\ K_0 &= 1.00 \text{ J} \\ \epsilon_0 &= 1.00 \cdot 10^5 \text{ J/s}. \end{aligned}$$

The numerical boundary condition is extrapolated from the interior domain using either *Riemann* or *Giles*, see Section 7.3 and 7.4 respectively. Since the computations is two dimensional the velocity vector is given by two components $[u_0\ v_0]$ for x- and y-direction respectively.

7.2 Outflow boundary condition

Using Figure 10 again to get a physical understanding of how the outflow boundary conditions are set up. The interior domain is no longer at the right hand side, but instead on the left hand side. Hence, apart from one of the characteristics, all information propagation are pointing out of the domain, which indicates that the solution is not dependent on the boundary values but instead the boundary values are a part of the solution. To cope with this problem one has to apply numerical boundary conditions to the scheme. To minimize the reflections back into the domain caused by poor numerical boundary conditions, we have used both Riemann and Giles boundary conditions.

Since one are dealing with subsonic conditions, the physical outflow boundary condition is set to the back pressure, which in this project is equal to the inlet pressure

$$p_N = p_0 = 1.01 \cdot 10^5 \text{ Pa}. \tag{60}$$

7.3 Riemann extrapolation

Further simplifying the problem to one dimension, this then makes the physical understanding easier to acknowledge. Using Eq. (58) with $\mathbf{Q} = \mathbf{0}$ in one dimension

$$\frac{\partial \mathbf{U}}{\partial t} + \mathbf{B}\frac{\partial \mathbf{U}}{\partial x} = \mathbf{0} \tag{61}$$

transformed into primitive variables ρ, u, p (see [10]), leading to the system

$$\frac{\partial \widehat{\mathbf{V}}}{\partial t} + \widehat{\mathbf{B}}\frac{\partial \widehat{\mathbf{V}}}{\partial x} = \mathbf{0} \tag{62}$$

where

$$\widehat{\mathbf{V}} = \begin{bmatrix} \rho \\ u \\ p \end{bmatrix}, \quad \widehat{\mathbf{B}} = \begin{bmatrix} u & \rho & 0 \\ 0 & u & \frac{1}{\rho} \\ 0 & \rho c^2 & u \end{bmatrix}.$$

Diagonalizing Eq. (62) by multiplying with $\mathbf{L}^{-1}$ from the left gives

$$\mathbf{L}^{-1}\frac{\partial \widehat{\mathbf{V}}}{\partial t} + \Lambda \mathbf{L}^{-1}\frac{\partial \widehat{\mathbf{V}}}{\partial x} = \mathbf{0} \tag{63}$$

where

$$\mathbf{L}^{-1} = \begin{bmatrix} 1 & 0 & -\frac{1}{c^2} \\ 0 & 1 & \frac{1}{\rho c} \\ 0 & 1 & -\frac{1}{\rho c} \end{bmatrix}, \quad \mathbf{L} = \begin{bmatrix} 1 & \frac{\rho}{2c} & -\frac{\rho}{2c} \\ 0 & \frac{1}{2} & \frac{1}{2} \\ 0 & \frac{\rho c}{2} & -\frac{\rho c}{2} \end{bmatrix}$$

and the diagonal eigenvalue matrix

$$\Lambda = \mathbf{L}^{-1}\widehat{\mathbf{B}}\mathbf{L} = \begin{bmatrix} u & 0 & 0 \\ 0 & u+c & 0 \\ 0 & 0 & u-c \end{bmatrix}.$$

Eq. (63) can now be written as

$$\frac{\partial \mathbf{W}}{\partial t} + \Lambda \frac{\partial \mathbf{W}}{\partial x} = \mathbf{0} \tag{64}$$

where the characteristic variables are obtained from

$$\frac{\partial \mathbf{W}}{\partial t} = \mathbf{L}^{-1}\frac{\partial \widehat{\mathbf{V}}}{\partial t}, \quad \frac{\partial \mathbf{W}}{\partial x} = \mathbf{L}^{-1}\frac{\partial \widehat{\mathbf{V}}}{\partial x} \tag{65}$$

This show that the components of $\mathbf{W}$ propagate along the corresponding characteristics with the speed given by the respective component of Λ. It is important to notice that (65) only holds when $\mathbf{L}^{-1}$ is constant, which is not the case since it depends on x for a two-dimensional flow. But in one-dimensional flow $\mathbf{W}$ can be defined as a non-constant as long as no more than two differentials appear in the linear combination (65), see [10]. Thus, by investigating (64) one can see that the components can be written as

$$\frac{\mathrm{d}w}{\mathrm{d}t} = \frac{\partial w}{\partial t} + \frac{\mathrm{d}x}{\mathrm{d}t}\frac{\partial w}{\partial x} = 0$$

which indicates that the variables w, also called *Riemann variables* and *Riemann invariants*, remain constant along a given set of characterstics. This gives the definition of the three characteristics

$$\begin{aligned} \frac{\mathrm{d}x}{\mathrm{d}t} &= u \\ \frac{\mathrm{d}x}{\mathrm{d}t} &= u+c \\ \frac{\mathrm{d}x}{\mathrm{d}t} &= u-c. \end{aligned}$$

Figure 11. The characteristic lines for a one-dimensional flow.

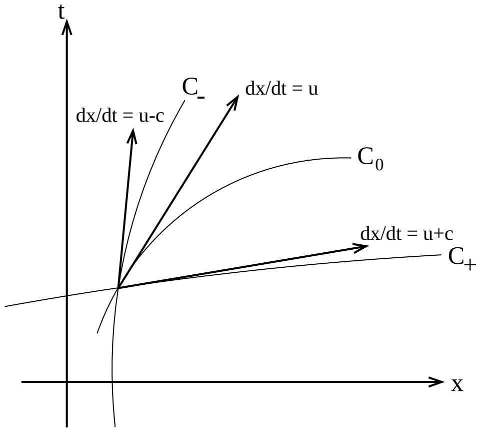

The first characteristic equation expresses the constant transport of entropy along the path line $dx/dt = u$ as (see [10])

$$\frac{\partial s}{\partial t} + u\frac{\partial s}{\partial x} = 0. \tag{66}$$

Eq. (66) indicates that the entropy propagates along the path line and is conserved along this characteristic, as long as discontinuities do not appear. If assuming isentropic flow, the two other Riemann variables can be integrated to obtain the following

$$w_2 = u + \frac{2}{\gamma - 1}c \tag{67}$$

$$w_3 = u - \frac{2}{\gamma - 1}c, \tag{68}$$

which represent the propagation of pressure waves along the respective characteristic variables.

The Riemann invariants (67) and (68) is constant along this given path. Extrapolating these variables, it is possible to obtain the boundary variables numerically. A first order extrapolation is given by

$$q_i = \frac{3}{2}q_{i-1} - \frac{1}{2}q_{i-2} \tag{69}$$

where q is a general flow variable, which in this case is the Riemann invariant w.

7.4 Giles extrapolation

Another approach of making non-reflecting boundary conditions in aeroacoustics applications is to instead investigate the wave nature of the solution. Doing a Fourier analysis in the same way as for the Riemann invariants, but here instead in two-dimensions linearized around a constant state in time; the Reynolds-averaged equations given by (58) with $\mathbf{Q} = \mathbf{0}$

$$\frac{\partial \mathbf{U}}{\partial t} + \mathbf{B}\frac{\partial \mathbf{U}}{\partial x} + \mathbf{C}\frac{\partial \mathbf{U}}{\partial y} = \mathbf{0}. \tag{70}$$

Considering the wave solution

$$\mathbf{U}(x, y, t) = \mathbf{u}e^{i(k_x x + k_y y - \omega t)}r \tag{71}$$

we obtain the dispersion relation from

$$\det|-\omega\mathbf{I} + k_x\mathbf{B} + k_y\mathbf{C}| = 0$$

where ω is the eigenvalue.

With ω as eigenvalue we obtain one right $\mathbf{r}$ and one left $\mathbf{l}$ eigenvector by

$$(-\omega\mathbf{I} + k_x\mathbf{B} + k_y\mathbf{C})\,\mathbf{r} = 0 \tag{72}$$

and

$$\mathbf{l}\,(-\omega\mathbf{I} + k_x\mathbf{B} + k_y\mathbf{C}) = 0. \tag{73}$$

Normally one is concerned with wave problems propagating in an infinite domain, so it is usual to consider a group of waves with the same k_x and k_y with different values of ω, where the above right and left eigenvector would be imposed. However, when dealing with boundary conditions the importance is how the waves develop in the spatial domain. A general solution $\mathbf{U}$ at the boundaries $x = 0$ and $x = L$ can be decomposed into a sum of Fourier modes with different values of ω and k_y, where each of these modes is a collection of waves with the same ω and k_y with different values of k_x. Therefore it is necessary to obtain a set of eigenvectors that has $-k_x$ as eigenvalues. This is done by multiplying Eq. (72) with $\mathbf{B}^{-1}$

$$\mathbf{B}^{-1}\left(-\omega\mathbf{I} + k_x\mathbf{B} + k_y\mathbf{C}\right)\mathbf{r} = \left(-\omega\mathbf{B}^{-1} + k_x\mathbf{I} + k_y\mathbf{B}^{-1}\mathbf{C}\right)\mathbf{r} = 0.$$

Which implies that $\mathbf{r}$ still is the right eigenvector with the eigenvalue $-k_x$. On the other hand, the left eigenvector will not be equivalent to Eq. (73) when $-k_x$ is the eigenvalue

$$\widehat{\mathbf{l}}\,\mathbf{B}^{-1}\left(-\omega\mathbf{I} + k_x\mathbf{B} + k_y\mathbf{C}\right) = 0,$$

where it is easy to see the relation between the new eigenvector $\widehat{\mathbf{l}}$ and the previous eigenvector $\mathbf{l}$ is

$$\widehat{\mathbf{l}} = \mathbf{l}\,\mathbf{B}, \tag{74}$$

which is an important relation in finding the boundary conditions.

The mathematical difference of the two sets of eigenvectors is the orthogonality. The right eigenvector $\mathbf{r}$ is orthogonal to the left eigenvector $\mathbf{l}$ of the same matrix, except for the one with the same eigenvalue ω. Thus, if ω_n and ω_m are two different roots of the dispersion relation for the same values of k_x and k_y, the orhtogonality gives that $\mathbf{l}(\omega_n, k_x, k_y)\,\mathbf{r}(\omega_m, k_x, k_y) = 0$. Equivalently when $k_{x,n}$ and $k_{x,m}$ are two different eigenvalues with constant values of ω and k_y we obtain

$$\widehat{\mathbf{l}}(\omega, k_{x,n}, k_y)\,\mathbf{r}(\omega, k_{x,m}, k_y) = 0.$$

Let k_n be the n^{th} root of the dispersion relation for a given value of ω and k_y, and $\mathbf{l}_n$ be the corresponding null-vector of $(k_{x,n}\mathbf{B} + k_y\mathbf{C})$. Then $\widehat{\mathbf{l}}_n$ can be defined as

$$\widehat{\mathbf{l}}_n = \left[\frac{k_{x,n}}{\omega}\right]_{k_y=0}\mathbf{l}_n\mathbf{B}, \tag{75}$$

which implies that when $k_y = 0$ we obtain the important relation

$$\widehat{\mathbf{l}}_n = \mathbf{l}_n. \tag{76}$$

By dividing the dispersion relation by ω one can see that $\widehat{\mathbf{l}}_n$ becomes a function of $\frac{k_y}{\omega}$. By Taylor expansion of $\widehat{\mathbf{l}}_n$ around $\lambda = k_y/\omega = 0$ we obtain

$$\widehat{\mathbf{l}}_n(\lambda) = \left[\widehat{\mathbf{l}}_n\right]_{\lambda=0} + \lambda\left[\frac{\mathrm{d}\widehat{\mathbf{l}}_n}{\mathrm{d}\lambda}\right]_{\lambda=0} + \frac{1}{2}\lambda^2\left[\frac{\mathrm{d}^2\widehat{\mathbf{l}}_n}{\mathrm{d}\lambda^2}\right]_{\lambda=0} + \ldots$$

Keeping the terms up to second-order, this together with (75) and (76) will now essentially become an approximation giving

$$\bar{\mathbf{l}}_n(\lambda) = \left[\mathbf{l}_n\right]_{\lambda=0} + \frac{k_y}{\omega}\left[\frac{k_{x,n}}{\omega}\frac{\mathrm{d}\mathbf{l}_n}{\mathrm{d}\lambda}\mathbf{B}\right]_{\lambda=0}. \tag{77}$$

where $\bar{\mathbf{l}}_n \approx \widehat{\mathbf{l}}_n$.

Before continuing this analysis, it is necessary to find an expression to obtain a closed boundary condition. Since $\mathbf{U}$ can be decomposed into a sum of Fourier modes, the most general case when just considering constant ω and k_y becomes

$$\mathbf{U}(x, y, t) = \left[\sum_{n=1}^{N} a_n\mathbf{r}_n e^{ik_{x,n}x}\right] e^{i(k_y y - \omega t)} \tag{78}$$

Ideally a non-reflecting boundary condition would be to specify that $a_n = 0$ for each n that corresponds to an incoming wave on the boundaries. Since the eigenvectors are orthogonal, we can obtain

$$\widehat{\mathbf{l}}_n\mathbf{U} = \widehat{\mathbf{l}}_n\left[\sum_{m=1}^{N} a_m\mathbf{r}_m e^{ik_{x,m}x}\right]e^{i(k_y y-\omega t)}$$

and so the specification of a non-reflecting boundary condition would be

$$\widehat{\mathbf{l}}_n\mathbf{U} = 0, \tag{79}$$

for all n corresponding to incoming waves.

Returning to (77), and using (79) one obtains the following boundary condition

$$\left([\mathbf{l}_n]_{\lambda=0} + \frac{k_y}{\omega}\left[\frac{k_{x,n}}{\omega}\frac{\mathrm{d}\mathbf{l}_n}{\mathrm{d}\lambda}\mathbf{B}\right]_{\lambda=0}\right)\mathbf{U} \simeq 0, \tag{80}$$

which, by using Eq. (71), is equivalent to

$$[\mathbf{l}_n]_{\lambda=0}\frac{\partial\mathbf{U}}{\partial t} - \left[\frac{k_{x,n}}{\omega}\frac{\mathrm{d}\mathbf{l}_n}{\mathrm{d}\lambda}\mathbf{B}\right]_{\lambda=0}\frac{\partial\mathbf{U}}{\partial y} \simeq 0. \tag{81}$$

Before applying the boundary condition (81), the Euler equations in two dimensions Eq. (70) has to be transformed into primitive variables to obtain the eigenvectors

$$\frac{\partial\widehat{\mathbf{V}}}{\partial t} + \widehat{\mathbf{B}}\frac{\partial\widehat{\mathbf{V}}}{\partial x} + \widehat{\mathbf{C}}\frac{\partial\widehat{\mathbf{V}}}{\partial y} = \mathbf{0} \tag{82}$$

where $\widehat{\mathbf{V}} = [\rho \quad u \quad v \quad p]^T$. By following the analysis given above, the eigenvalues are found to be

$$\begin{array}{rclcccccc}
\widehat{\mathbf{l}}_1 & = & [& -1 & 0 & 0 & 1 &] \\
\widehat{\mathbf{l}}_2 & = & [& 0 & -u\lambda & 1-v\lambda & -\lambda &] \\
\widehat{\mathbf{l}}_3 & = & [& 0 & 1-v\lambda & u\lambda & 1-v\lambda &] \\
\widehat{\mathbf{l}}_4 & = & [& 0 & -1(1-v\lambda) & -u\lambda & 1-v\lambda &]
\end{array} \tag{83}$$

In the same way as the analysis given for the Riemann boundary conditions, the Euler equations have four characteristics which indicates how the information propagates in time and space. In subsonic conditions there will be three characteristics pointing in the flow direction, and one which points into the flow direction. Inserting the eigenvectors Eq. (83) into the boundary condition Eq. (81) one obtain four equations, where three represent the inflow boundary condition

$$\begin{bmatrix} -1 & 0 & 0 & 1 \\ 0 & 0 & 1 & 0 \\ 0 & 1 & 0 & 1 \end{bmatrix}\frac{\partial\widehat{\mathbf{V}}}{\partial t} + \begin{bmatrix} 0 & 0 & 0 & 0 \\ 0 & u & v & 1 \\ 0 & v & -u & v \end{bmatrix}\frac{\partial\widehat{\mathbf{V}}}{\partial y} = 0 \tag{84}$$

and one the outflow boundary condition

$$\begin{bmatrix} 0 & -1 & 0 & 1 \end{bmatrix}\frac{\partial\widehat{\mathbf{V}}}{\partial t} + \begin{bmatrix} 0 & -v & u & v \end{bmatrix}\frac{\partial\widehat{\mathbf{V}}}{\partial y} = 0. \tag{85}$$

These equations is implemented in the program, where the outgoing characteristics equation (85) is extrapolated from the interior points, and the incoming characteristics equation (84) is calculated by integrating these equations in time, with the described method for time integration in Section 6.

7.5 Periodic boundary condition

At the duct "walls" periodic boundary conditions is imposed, which means that the numerical domain is infinity in the y-direction and should not impose any reflections back into the domain. For an arbritary numerical flow variable q this it is written as

$$q_{i,j=1/2} = q_{i,j=N+1/2}$$

8 Computations

A parametric study of how the aeroacoustic signal propagate with different flow variables, numerical parameters and boundary conditions is done in order to evaluate the second-order accurate finite volume scheme used in Euranus, [15]. The parameters considered in this study and their default values are shown in Table 1.

Table 1. Default values of the variables in the parametric study. † Navier-Stokes equations. ‡ Inflow acoustic b.c. = Riemann (R) and Outflow acoustic b.c. = Giles (G) for a downstream imposed wave, opposite for an upstream imposed wave.

	Non-Dimensionals	**Symbol**	**Default**
Flow Dependent	Points Per Circumferential Wavelength	N_θ	20
	Cut-off ratio	ξ	1.1
	Mean Flow Axial Mach Number	M	0.4
Code Dependent	Points Per Period in Time	N_t	40
	2^{nd}-order AV Mean Flow Smoothing	$\sigma^{(2)}$	1.0
	4^{th}-order AV Mean Flow Smoothing	$\sigma^{(4)}$	0.1
	2^{nd}-order AV Turbulence Smoothing	$\kappa^{(2)}$	1.0
	4^{th}-order AV Turbulence Smoothing	$\kappa^{(4)}$	0.1
	Turbulent Reynolds Number	$\mathrm{Re}_{\mathrm{tu}}$	$5 \cdot 10^5$
	Equations used in the computations	eq.	N-S†
	Boundary Conditions (Inflow/Outflow)	b.c.	R/G‡
Grid Dependent	Cell Aspect ratio	$\frac{\Delta x}{\Delta y}$	1.0
	Axial Stretching Ratio	$\frac{\Delta x_{j+1}}{\Delta x_j}$	1.0
	Skew Angle (degrees)	α	0.0
	Circumferential Distribution	CircDist	Uniform

Since some parameters that have not been considered in previous sections have been introduced in Table 1, it is necessary to give a brief explanation to these.

First, the flow dependent variables, which is the major part of this parametric study, the test is performed by prescribing a sinusoidal wave input on either one of the axial boundaries (representing downstream or upstream traveling waves) of varying frequencies or varying wavelength in the y-direction. These waves are described in terms of $\omega\Delta t$ and $k_y\Delta y$ respectively. It is convenient to represent these terms as non-dimensional quantities of points per wavelength and cut-off frequency (as in (18)) respectively

$$N_\theta = \frac{2\pi}{k_y \Delta y} \tag{86}$$

and

$$\xi = \frac{\omega}{c k_y \sqrt{1 - M^2}}.$$

The number of points per wavelength, N_θ, is essentially the most important variable. Since this in fact describes the wave length of the aeroacoustic signal – which in reality will for instance vary during different flight conditions, but more related to this project; it defines the grid size and number of time steps per period at the given wave length, see (18). Therefore it is important to evaluate how the numerical error will vary with different values of N_θ.

Next, within the code-dependent parameters; the global time step N_t is halved and doubled to see the effect of reducing and increasing points per period in time. The Turbulent Reynolds Number, $\mathrm{Re}_{\mathrm{tu}}$, is defined through $\mathrm{Re}_{\mathrm{tu}} = \frac{u'' l''}{\nu}$, where u'' and l'' is a measure of the fluctuating velocity and length scale respectively for the eddies. Reformulated to kinetic and dissipation energy, see [12], we obtain

$$\mathrm{Re}_{\mathrm{tu}} = \frac{\overline{\rho} K^2}{\mu \epsilon}.$$

The artificial viscosity coefficients , $\sigma^{(2)}$ and $\sigma^{(4)}$, are explained in Section 5.1.2. Similarly the artificial viscosity in the turbulence equations are described in Section 5.2.

Within the code dependent runs, we also study the effect of the equations used in the computations. The Navier-Stokes equations (Reynolds-averaged with eddy viscosity), are used as default and comparisons are made with results from solving the Euler equations.

Finally, the grid dependent parameters; the Cell Aspect Ratio, Axial Stretching Ratio, Skew Angle α, and Circumferential Distribution, describes the computational grid which can be seen in Figure 7 and 12, respectively

Figure 12. The different grids used in this project. (a) is the default grid that is far the most used.

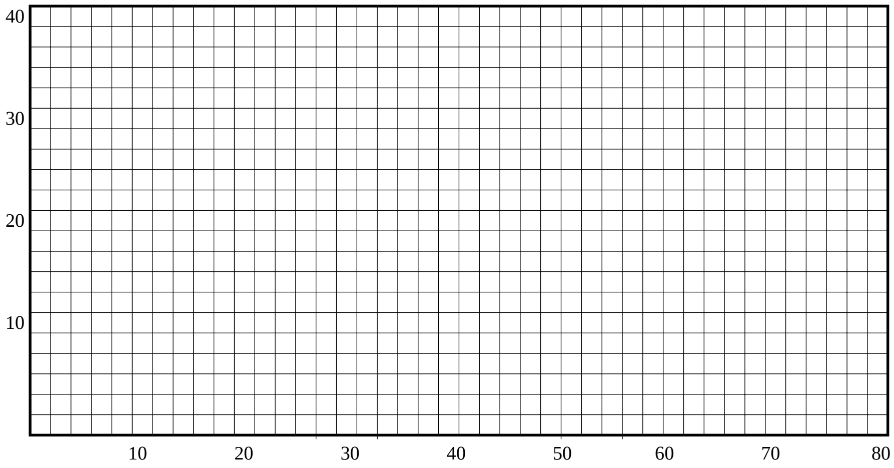

(a) The default grid size of the computational domain.

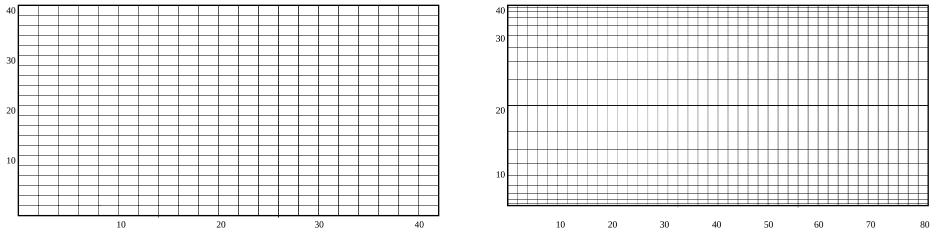

(b) Cell Aspect Ratio, $\frac{\Delta x}{\Delta y} = 2$.

(c) Non-uniform distribution in y.

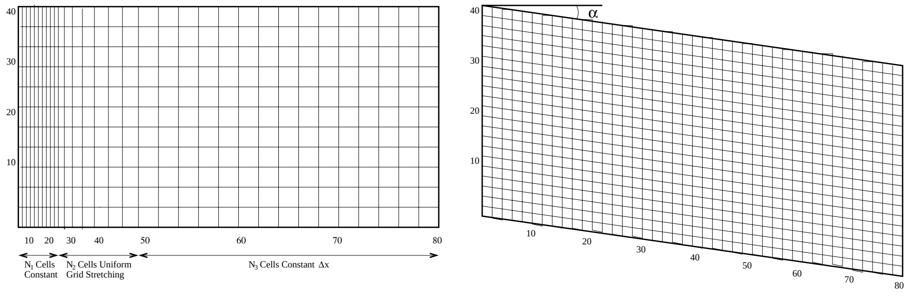

(d) Axial grid stretching imposed from x=0.

(e) Skew angle α.

8.1 CFD input parameters

The sinusoidal input pressure is added to the mean flow as follows

$$p = \mathrm{real}\left(\hat{p}e^{i(\omega t - k_y y)}\right), \tag{87}$$

where the pressure amplitude $\hat{p}$ is selected such that non-linear wave-propagation effects can be neglected. In this project, with $p_0 = 101$ kPa, a sound pressure level of 130 dB corresponds to a peek-to-mean pressure variation of

$$\hat{p} = 89\ \mathrm{Pa}$$

The input velocities are calculated directly from inserting the ansatz (87) into Eq. (10). This yields

$$u = \left(\frac{1}{\frac{\omega}{k_x c} - M}\right)\frac{p}{\rho c}, \tag{88}$$

and

$$v = \frac{k_x}{k_y} \tag{89}$$

where k_x is taken from (19). In addition, if not explicitly stated, the following free stream conditions is defined as constants, unless something else is explicitly stated, throughout this study

Default circumferential grid spacing	Δy	$=$	$2.5 \cdot 10^{-3}$ m
Default axial grid spacing	Δx	$=$	$2.5 \cdot 10^{-3}$ m
Free stream axial velocity	U_0	$=$	$136\ \mathrm{m/s}$
Free stream circumferential velocity	V_0	$=$	$0\ \mathrm{m/s}$
Free stream temperature	T_0	$=$	$288\ \mathrm{K}$
Free stream pressure	p_0	$=$	$1.01 \cdot 10^5\ \mathrm{Pa}$
Thermal and calorical perfect gas	γ	$=$	1.4
Specific gas constant	R	$=$	$287\ \mathrm{J/(kg \cdot K)}$
Laminar Reynolds Number	Re	$=$	$9.22 \cdot 10^5.$

The circumferential grid spacing Δy is chosen such that it is compatible with the order of magnitude of a typical spacing between a rotor-rotor or stator-stator, i.e. $40 \cdot \Delta y = 0.1\ \mathrm{m}$.

In order to obtain a periodic steady state condition, one must assure that the acoustic signal and the fluid has traveled through the whole domain. Data is then collected for a whole period at the given frequency $\tilde{\omega}$. Using (18) together with $k_y = \frac{2\pi}{N_\theta \Delta y}$ and $\tilde{\omega} = \frac{\omega}{c} = \frac{2\pi}{c t_{2\pi}}$ we obtain

$$t_{2\pi} = \frac{N_\theta \Delta y}{\xi c \sqrt{1 - M^2}}.$$

In this project we have chosen to use the number of point per period in time, i.e. $N_t = \frac{t_{2\pi}}{\Delta t}$, constant $N_t = 40$. From earlier investigations, [5] and [16], this number has proved to give small time integration errors. Hence, with 40 time steps after the solution has converged we have a time dependent solution that covers a whole period in time.

8.2 Post-processing

In this section a thorough step-by-step list of the post-processing is presented. This process can be described as follows:

1. **Extracting flow variables from CFD solution**. The absolute velocity components $\mathbf{U} = \mathbf{U}(x, y, t)$ and $\mathbf{V} = \mathbf{V}(x, y, t)$, together with the pressure $\mathbf{P} = \mathbf{P}(x, y, t)$ are picked out at discrete points in space and time forming three separate matrices, one for each of these flow variables.

2. **Nondimensionalizing**. The discrete flow matrices are then non-dimensionalized, see also Eq. (10), as follows
$$\begin{aligned}\mathbf{u} &= \frac{\mathbf{U} - U_0}{c}\\ \mathbf{v} &= \frac{\mathbf{V} - 0}{c}\\ \mathbf{p} &= \frac{\mathbf{P} - P_0}{P_0}\end{aligned} \tag{90}$$
where the subscript 0 defines the free stream condition. The new matrices $\mathbf{u}$, $\mathbf{v}$ and $\mathbf{p}$ are now the perturbations around the mean flow.

3. **Fourier transforming**. The Fast Fourier Transform used for discrete points is defined as
$$F(k) = \sum_{j=1}^{N} f(j)\omega_N^{(j-1)(k-1)} \tag{91}$$
where $\omega_N = e^{(-2\pi)/N}$ is an N^{th} root of unity. We use (91) on the data in the matrices defined in Eq. (90) twice, first in time and then in y-direction. A complex expression of the axial wave amplitude $\hat{\mathbf{f}}$ is then obtained
$$\hat{\mathbf{f}}(x)_{k_y,\omega} = ke^{-ik_x x}$$
where k is a constant. After the Fourier transform we now have three set of vectors $\hat{\mathbf{u}}(x)_{k_y,\omega}$, $\hat{\mathbf{v}}(x)_{k_y,\omega}$ and $\hat{\mathbf{p}}(x)_{k_y,\omega}$ that all contain complex numbers.

4. **Wavesplitting**. We then apply the wavesplitting technique, see Section 3.2.2, to obtain separate information on each of the waves that exist in the solution. The wavesplitted acoustic waves, as in (21), are
$$\mathbf{p}(x)^{ds,us}_{k_y,\omega} = \frac{1}{2}\hat{\mathbf{p}}(x)_{k_y,\omega} \pm \gamma\frac{\xi}{2\sqrt{\xi^2-1}}\hat{\mathbf{u}}(x)_{k_y,\omega} \pm \gamma\frac{M}{2\sqrt{(\xi^2-1)(1-M^2)}}\hat{\mathbf{v}}(x)_{k_y,\omega}$$
where $q_{ds,us}$ has been substituted with $\mathbf{p}(x)^{ds,us}_{k_y,\omega}$ for simplicity. The plus and minus sign represent a downstream and upstream acoustic wave, which also depends on whether the cut-off ratio ξ is larger or smaller than one. The vorticity wave is given by Eq. (22)
$$\mathbf{q}(x)^{v}_{k_y,\omega} = \frac{-\xi\sqrt{1-M^2}}{\xi^2(1-M^2)+M^2}\left(\frac{1}{\gamma}\hat{\mathbf{p}}(x)_{k_y,\omega} + M\hat{\mathbf{u}}(x)_{k_y,\omega} - \xi\sqrt{1-M^2}\hat{\mathbf{v}}(x)_{k_y,\omega}\right)$$
For a more detailed description of the physical difference of the acoustic and vortical waves, we refer to Section 3.

5. **Converting to sound pressure level (SPL)**. The final step of the post processing is to convert the acoustic pressure- and vorticity waves into sound pressure levels (SPL). Since the acoustic waves now represents an amplitude of the signal at each x-position in the flow, i.e. a function of x, it will among other things give indications on whether the damping from fluid- or numerical viscosity has reduced the original SPL. The conversion is done be re-dimensionalizing and taking the logarithm of the acoustic wave amplitudes
$$\mathbf{p}^{us,ds}_{SPL} = 20\log_{10}\left(\frac{P_0\left|\mathbf{p}(x)^{ds,us}_{k_y,\omega}\right|}{\sqrt{2.2}\cdot 10^{-5}}\right) \tag{92}$$
and for the vortical acoustic wave
$$\mathbf{q}^{v}_{SPL} = 20\log_{10}\left(\frac{\rho_0 c^2\left|\mathbf{q}(x)^{v}_{k_y,\omega}\right|}{\sqrt{2.2}\cdot 10^{-5}}\right), \tag{93}$$
where ρ_0 is the free-stream density and c is speed of sound.

The obtained dimensional sound pressure level $\mathbf{p}^{us,ds}_{SPL}$ and $\mathbf{q}^{v}_{SPL}$ can now be investigated for errors by comparing with the analytical sound pressure level.

8.3 Interpretation of the result

The analytical wave solution of Eq. (10) for a single frequency is

$$p = \mathrm{Re}\left(\hat{p}_{k_x,k_y,\omega}\, e^{i(\omega t - k_y y - k_x x)}\right). \tag{94}$$

From (86) we have that k_y is

$$k_y = \frac{2\pi}{N_\theta \Delta y}.$$

Applying this to (18) gives the frequency

$$\omega = \xi c k_y \sqrt{1 - M^2}.$$

The acoustic axial wave number is given by (19)

$$k_x^{ds,us} = \frac{M\xi \pm \sqrt{\xi^2 - 1}}{\sqrt{1 - M^2}} k_y,$$

which includes both up- and downstream acoustic wave. The vortical axial wave number is given by (20)

$$k_x^v = \frac{k_y \xi \sqrt{1 - M^2}}{M}.$$

8.3.1 Investigating raw CFD data

By solving (94) on discrete points, equivalent spaced to the CFD-evaluated grids, one has a totally comparable result. See Figure 13 and 14 for a rough comparison.

Figure 13. An illustration of how the acoustic signal propagates in the numerical quasi-duct for the theoretically constructed wave with known dispersion relations. Flow is from the left to right.

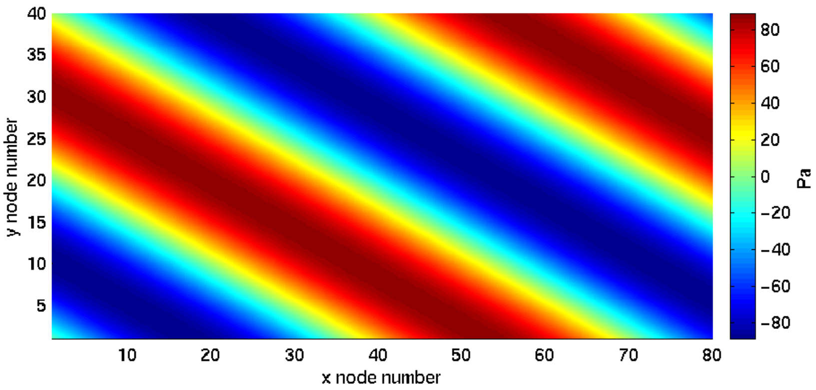

Figure 14. An illustration of how the acoustic signal propagates in the numerical quasi-duct for wave obtained by CFD. Flow is from the left to right. Note how the wave amplitude decays at the end of the duct.

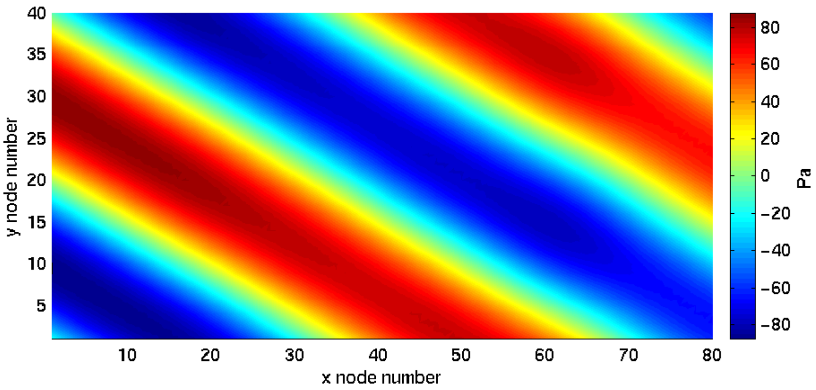

However, a comparison of these two figures do not say much except that the waves look similar, and that the wave from CFD-solution has some small defects at the outflow of the domain. To see some more qualitatively results, the post-processing described in Section 8.2 can be performed.

8.3.2 Investigating individual post-processed CFD data

After the post-processing, three vectors for the downstream, upstream and vortical wave is present, these vectors can be plotted, as in Figure 15. The y-axis contain the SPL, see Eq. (92) and (93), which in fact is the logarithmic amplitude of the sound wave. The x-axis is the x node number; that is the axial grid number. Hence, this is a plot of how the sound pressure level (or wave amplitude) varies with x. Both the CFD and the analytical solution involves three components; downstream and upstream acoustic wave together with the vortical wave.

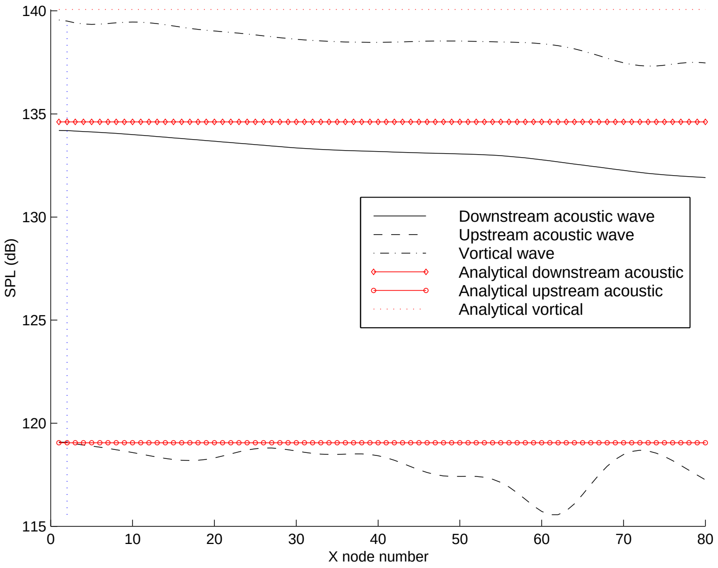

Figure 15. An example of the SPL for the CFD-results and the analytical-result obtained downstream propagating acoustic field (see Figure 14) plotted in the same graph for comparison. Note the amplitude (or SPL) decay of the CFD-solution going from left to right.

From Figure 15 one may already have noticed that the acoustic waves from the CFD-result deviates from the analytical result. This is caused by dissipation of the numerical errors, and is therefore non-physical related phenomena. The upstream wave has imposed some non-physical wiggles, which is caused by the reflections of the boundary condition at the acoustic output. Reflections are non-physical and should be as small as possible for non-reflecting conditions. These phenomena are discussed further in Section 8.4.

Reflections from boundary conditions will also impose a phase shift of the wave (94), and it is therefore appropriate to investigate how the phase of the acoustic and vortical waves changes axially. By differentiating Eq. (94) with respect to x we obtain the following expression for the axial phase

$$k_x = i\frac{1}{p}\frac{\partial p}{\partial x}. \tag{95}$$

Using this result on the discrete points, one can plot the phase with respect to x for both the CFD-result and the analytical-result, as in Figure 16. It is important to notice that the phase of the two acoustic and the vortical wave should coincide together with the analytical wave, since it only exist one phase for all the waves. This is not the case, and the reason for this will be discussed further in Section 8.4.

In order to present the data in an efficient way as well as retaining all important information, a combination-plot of the raw CFD-results in Figure 14 with the post-processed result in Figure 15 and 16 are used, see Figure 17.

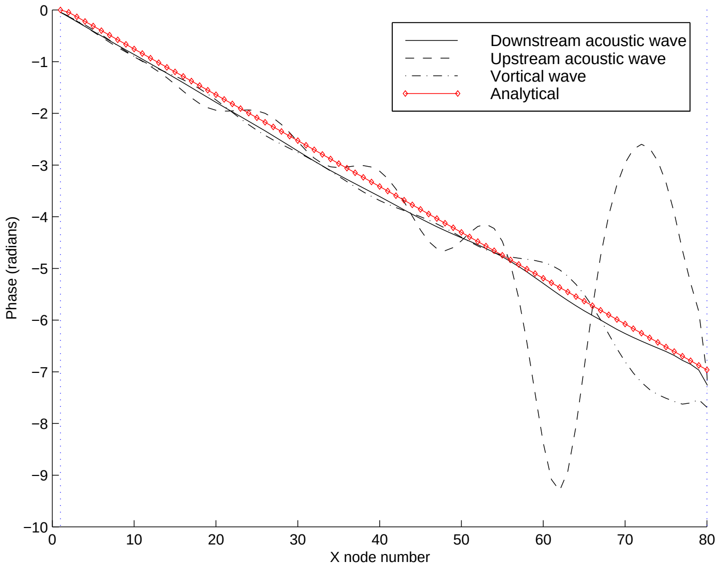

Figure 16. An example of the phase for the CFD-results and the analytical-result obtained acoustic field (see Figure 14) plotted in the same graph for comparison.

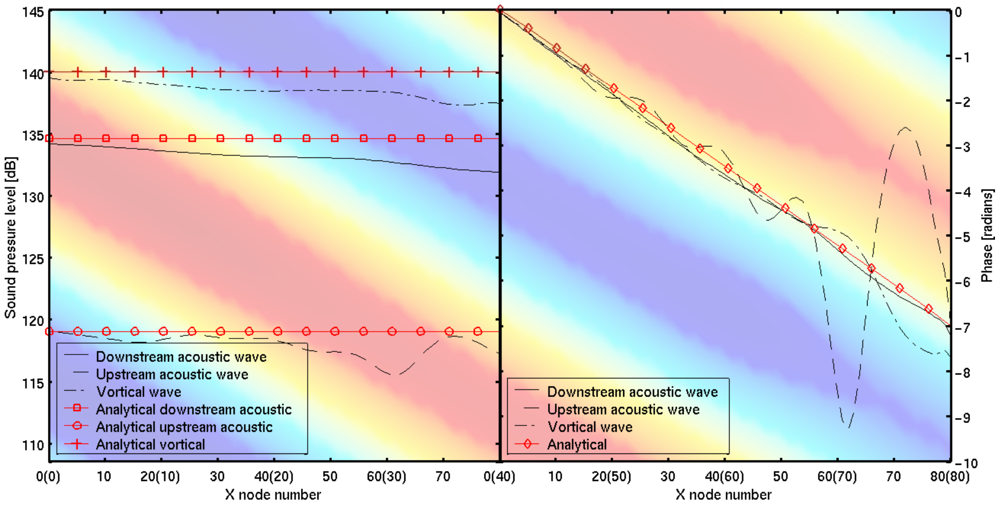

Figure 17. An example of the combined plot of Figure 14 (raw-CFD result), 15 (SPL) and 16 (phase). SPL to the left and phase to the right.

With this plot one is now able to do both qualitatively and quantitatively comparisons of all runs. The background-picture of each figure represents the raw CFD-result, and is dimensioned to be quantitatively fully comparable with all the other plots; using a fixed size of 80 points in x-direction, and 40 points in y-direction (height = 0.1 m and length = 0.2 m). Note that the x-axis of raw CFD results and the x-axis of the SPL- and phase-plots are not equal; the parenthesis at the x-axis is the node numbers for the raw result (background-picture). Also, the limits of the y-axis of both the SPL and phase may vary from each run to run.

8.3.3 Comparing multiple CFD runs

From the post-processed result in the previous section, the amplitude and phase for each individual run are plotted against axial node number. However, more important is the amplitude error $\Delta\epsilon$ (related to dissipation) and phase error $\Delta\Theta$ (related to dispersion), which is defined by the difference between the inclination of the theoretical and CFD-results for the amplitude and phase at a certain axial point respectively.

When computing flow between a rotor-rotor or stator-stator at a fixed radius (2D-computations) of internal turbomachinery it is obvious that the amplitude and phase error as a function of axial distance is of primary interest, but this does not represent the whole truth. Since the acoustic waves will have a two dimensional wave propagation, the dispersivity and dissipation will not only depend on the circumferential wave resolution N_θ, but also on the axial wave resolution N_x. Therefore an appropriate way of reducing the 2D-data to a 1D plot would be to use the true theoretical wavelength perpendicular to the wave front N_λ instead of N_θ only.

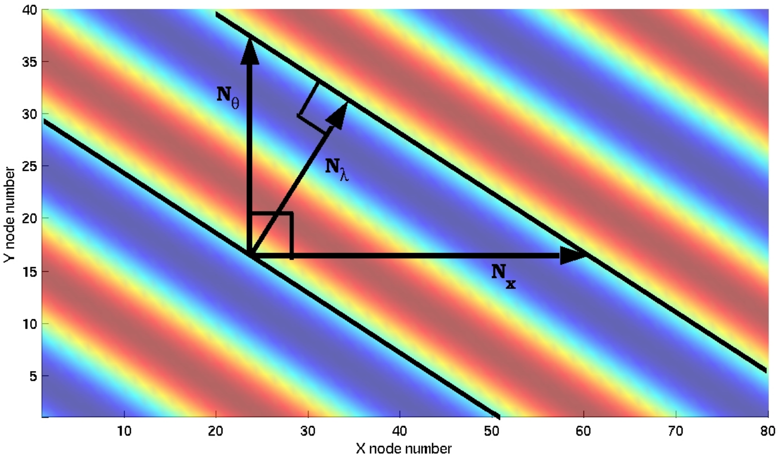

Figure 18. Relation between circumferential (N_θ), axial (N_x) and true wavelength (N_λ) perpendicular to the wave front.

From Figure 18 one see that the theoretical true wavelength N_λ can be constructed from N_θ and N_x by the following

$$\frac{1}{N_\lambda^2} = \frac{1}{N_\theta^2} + \frac{1}{N_x^2}. \tag{96}$$

Hence, instead of plotting against N_x we will here plot against N_λ. This reduces the data to a 1D plot, and will provide a form of averaged weighting towards the least well-defined direction, see Figure 19.

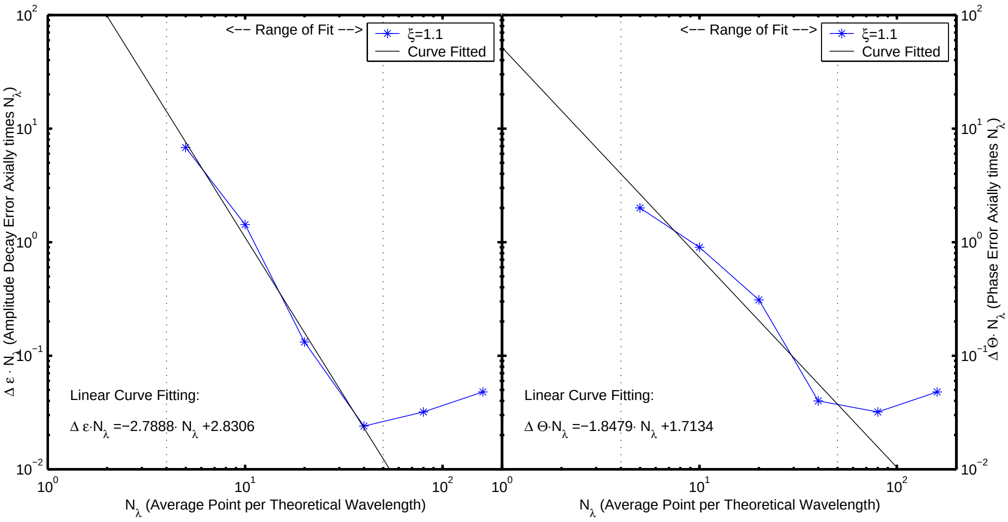

Figure 19. Amplitude decay error (left) and phase error (right) development as a function of the average points per theoretical wavelength on a cut-on downstream wave.

Any changes of axial amplitude decay $\Delta\epsilon$ for the cut-on waves can be assumed to be due to dissipation from numerical errors – the physical viscosity contributions is likely small. Hence, for the cut-on waves the errors are calculated as: $\Delta\epsilon = |\epsilon - 0|$. For cut-off waves, which has a natural decay rate in the axial direction, the errors are calculated as the difference between the theoretical decay rate (imaginary part of the axial wave number k_x, see (19)) and the numerical obtained decay rate, i.e. $\Delta\epsilon = |\epsilon - \epsilon_0|$ where ϵ_0 is the theoretical obtained amplitude decay. Likewise the phase error $\Delta\Theta$ is calculated as the difference in phase between the theoretical and numerical results.

8.4 Main error sources

From Figure 15 and 16 it can easily be seen that there are errors in the numerical solution. To give an exact explanation to this is difficult, but there are some error sources that can be seen upon as the far most contributing error terms.

As mentioned in Section 5.1.2 the numerical viscosity plays a major role in damping the amplitude of the waves axially. How much the amplitude is damped depends on the resolution of the wave, i.e. N_λ see Figure 20. A poor resoluted wave contains discontinuities, which induces artificial viscosity into the solution, see Appendix A. In addition to the numerical viscosity, there is also damping induced by the fluid viscosity, since we are using Navier-Stokes equations in the numerical computations, but this is likely to be small. However, with a large $\mathrm{Re}_{\mathrm{tu}}$ and a very fine mesh, damping from the physical viscous terms could be notable.

Figure 20. Example of sharp gradients on a poor resoluted wave (a).

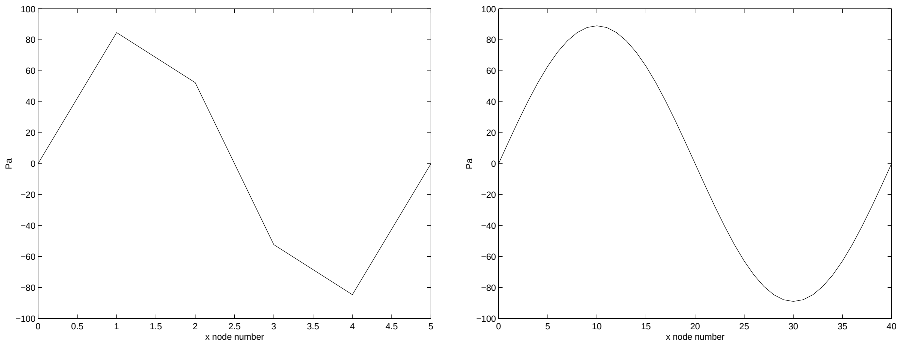

(a) $N_\theta = 5$, poor resoluted wave.

(b) $N_\theta = 40$, good resoluted wave.

For cut-off waves, the amplitude of the wave will quickly decrease to a level of the order of accuracy of the computer.

The solver is of second-order accuracy in space, which is at the lower limit of what to accept for aeroacoustic computations. The amplitudes are small compared to the free stream conditions, and are hard to distinguish from the numerical errors. In addition, when using a grid with non-orthogonal cells, see Figure 7 and 13(d), the order of accuracy will fall below second-order, which makes it even more difficult to distinguish the acoustic wave from numerical errors.

Another important factor that is highly relevant in this project is the error caused by reflections that originates from the boundaries, see Section 7. When waves are reflected back, superposition occur, which gives dispersion errors that imposes a phase shift in (94). In this project it can easily be detected by the wiggles at the upstream wave and by a phase plot. Note that the reflections from the boundaries will increase in time. Hence, the amount of reflections will depend on how long the calculation has run before collecting the data during one period.

In addition, a time integration error is also present. Having too few points per period in time, the dissipation and dispersion error will enhance.

It is important to notice that the axial wavenumber k_x in (19) is much less for upstream waves than for downstream waves. This gives a less resolution N_λ, which then induce more numerical damping. This is basically the reason why the quality of the upstream waves is poorer in comparison with the downstream waves.

The aim of this parametric study is to investigate how these error sources will interfere with each other when the given parameters are changed. The total number of standard cases is 67, with an upstream and a downstream wave input for each, giving a total number of 134 runs.

8.5 Influence from flow dependent parameter variations

The flow dependent variables involves the parameters N_θ, ξ and M (see Table 1). These parameters are combined giving a finite number of combinations that represents this part of the parametric study, all combinations of N_θ and ξ is tested. In Table 2 the range of study is given. The total number of runs will be 80, since there are two runs for each of the combinations; downstream and upstream traveling waves.

Table 2. Range of study for the flow dependent parameters. Note that number of runs is the double of the number variations. For each combination, there are two runs; upstream- and downstream-imposed waves respectively.

Symbol	Default	Range of Study	Variations
N_θ	20	5, 10, 20, 40, 80, 160	All combinations of N_θ and ξ, giving 36 var. and 72 runs
ξ	1.1	0.7, 0.9, 1.1, 1.5, 3.0, 5.0	
M	0.4	0.2, 0.4, 0.6, 0.8, 0.9	5 variations and 10 runs

A complete coverage of the runs from this part of the parametric study will not be included. Instead, some of the runs that represent the most important result will be prescribed. Flow is from left to right, with a downstream traveling acoustic wave imposed at the left boundary. Upstream traveling acoustic waves are imposed at the right boundary.

8.5.1 Variation of N_θ with constant ξ

In this section only the result from variation of N_θ, for $\xi = 1.1$, is presented. All other parameters are kept constant by the default values, see Table 1.

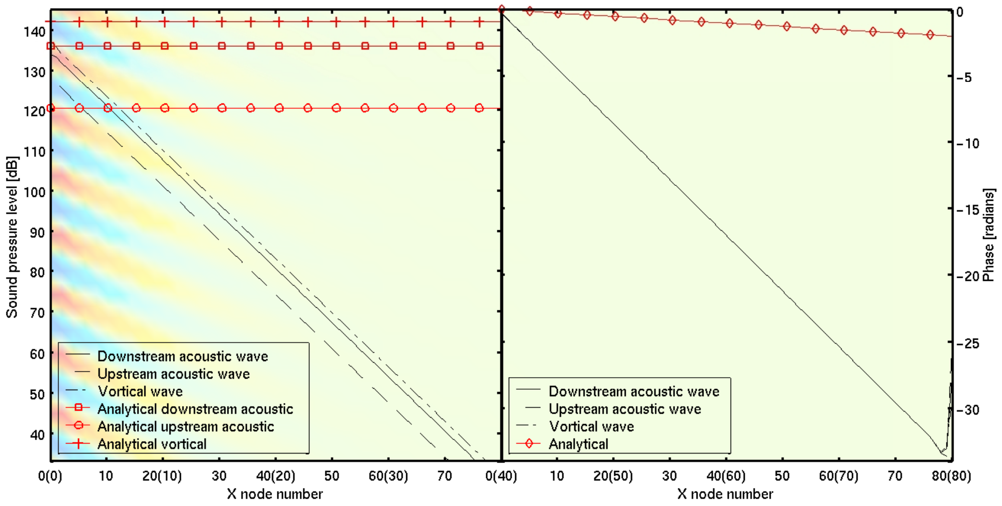

Figure 21. $N_\theta = 5$. Constant flow parameters: $\xi = 1.1$ and $M = 0.4$. Downstream.

From these plots one can see the amplitude decay and phase errors develops by changing the resolution N_θ is used. Basically, the results improve with larger N_θ up to about 80 points per wavelength, where it does not improve any more. The reason for this could be either the interaction of the viscous terms in the Navier-Stokes equations, time integration errors, or that the solution is not fully converged. This is summarized in Section 8.5.4.

The corresponding figures for the upstream traveling wave (flow is still going from left to right, but the acoustic wave is imposed at the right boundary and traveling upstream the flow) can be found in Appendix B.1. Note that the axial wavenumber is much

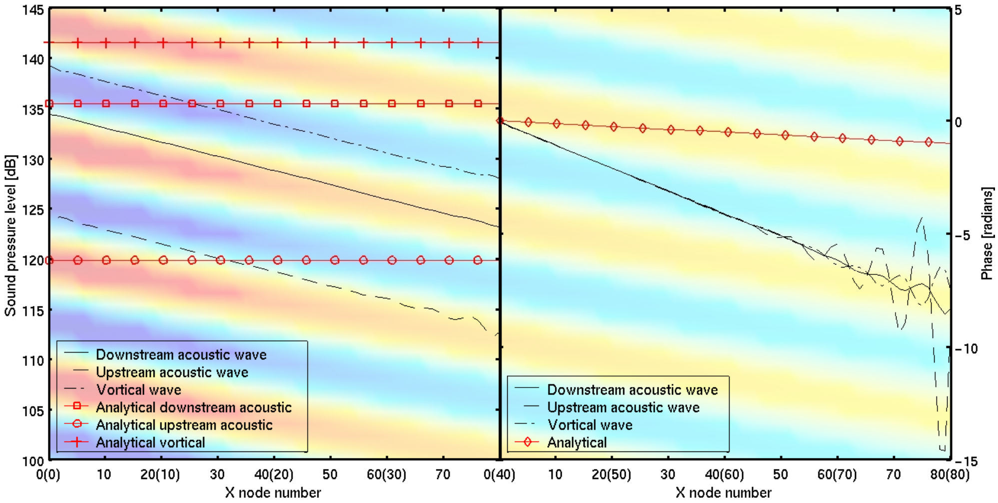

Figure 22. $N_\theta = 10.$ Constant flow parameters: $\xi = 1.1$ and $M = 0.4$. Downstream.

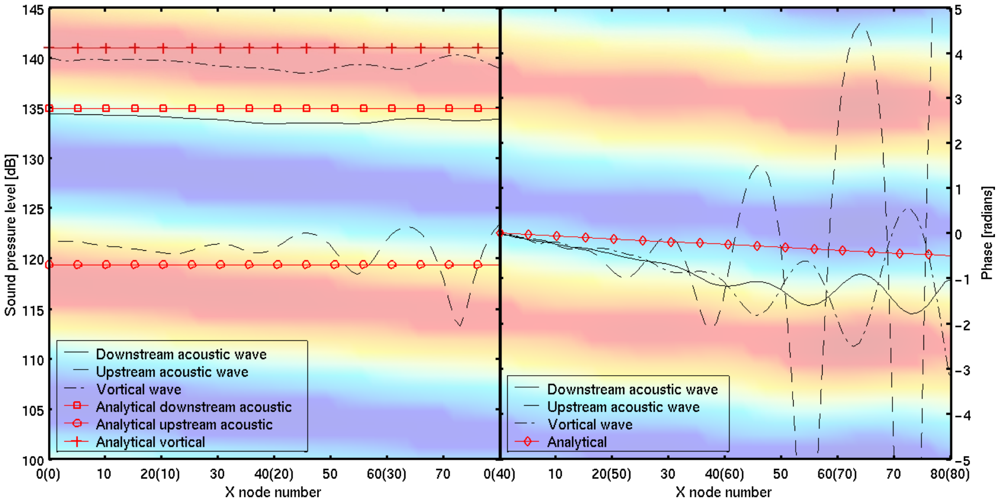

Figure 23. $N_\theta = 20.$ Constant flow parameters: $\xi = 1.1$ and $M = 0.4$. Downstream.

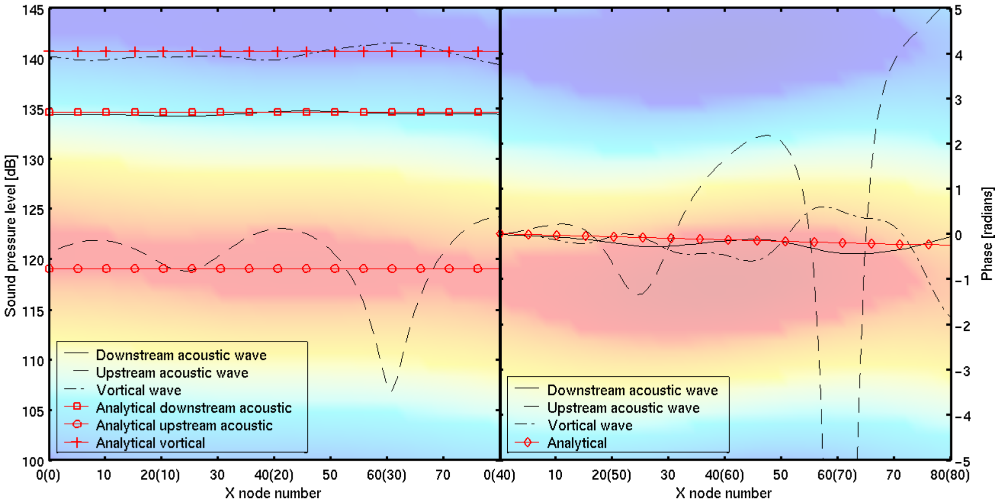

Figure 24. $N_\theta = 40.$ Constant flow parameters: $\xi = 1.1$ and $M = 0.4$. Downstream.

less than for downstream waves, giving less resolution which then induces numerical damping – this is basically the reason why the quality of the upstream waves are so poor in comparison with the downstream waves.

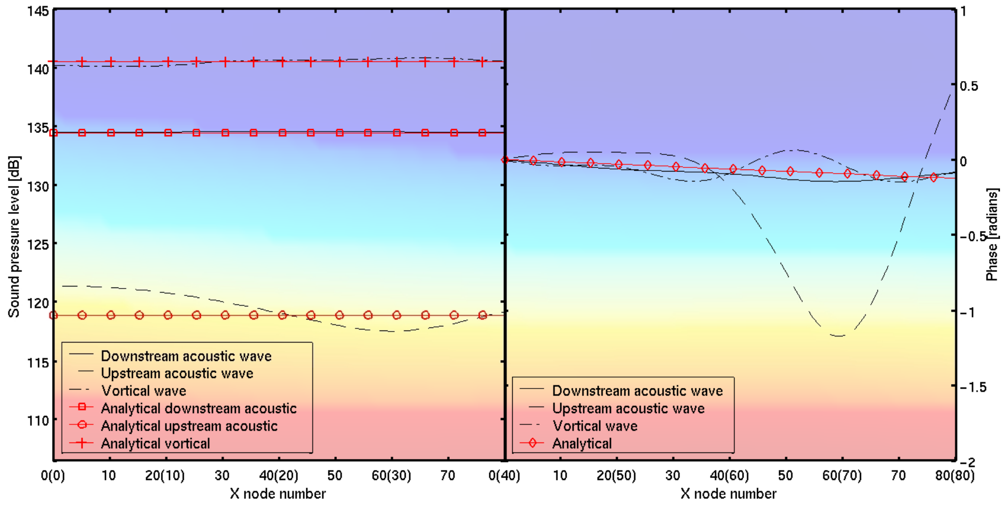

Figure 25. $N_\theta = 80$. Constant flow parameters: $\xi = 1.1$ and $M = 0.4$. Downstream.

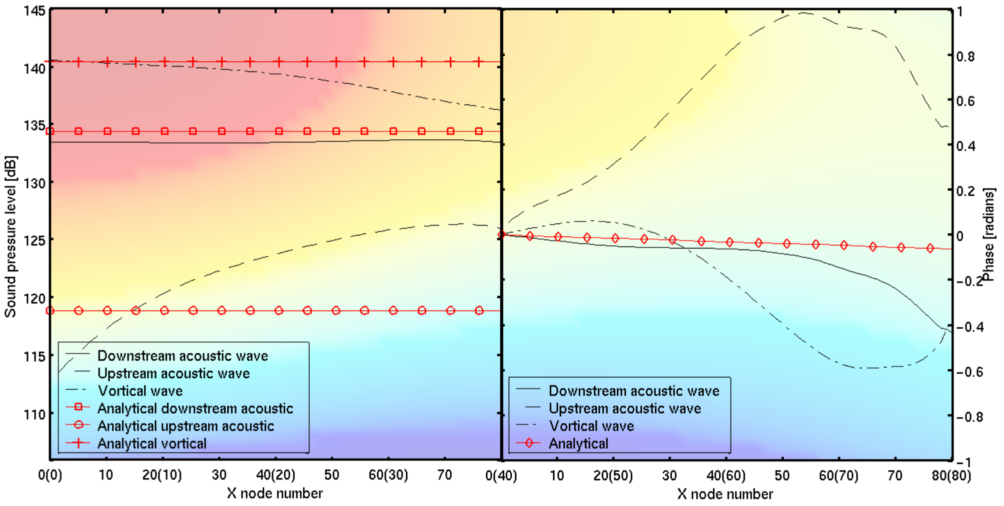

Figure 26. $N_\theta = 160$. Constant flow parameters: $\xi = 1.1$ and $M = 0.4$. Downstream.

8.5.2 Variation of ξ with constant N_θ

In this section the result from variation of ξ, for $N_\theta = 20$ only, is presented . The other parameters are kept constant with the default values, see Table 1.

Here it is important to notice how the cut-off waves ($\xi < 1$) decays, and that the acoustic cut-on waves ($\xi > 1$) is damped. As the cut-off ratio becomes much larger than one, the wavelength is reduces, which then leads to poorer resoluted waves and therefore introduces more numerical viscosity into the scheme. Especially when $\xi > 1.5$ and $\xi < 1$ the acoustic signal is damped to a level which makes it indistinguishable to the accuracy of the computer (noise floor), i.e. $1 \cdot 10^{-16}$. This trigger the computations to get spurious (see for instance at x-position of about 30 for $\xi = 5.0$), and the result will therefore becomes useless after this trigger-point.

Figure 27. $\xi = 0.7$. Constant flow parameters: $N_\theta = 20$ and $M = 0.4$. Downstream.

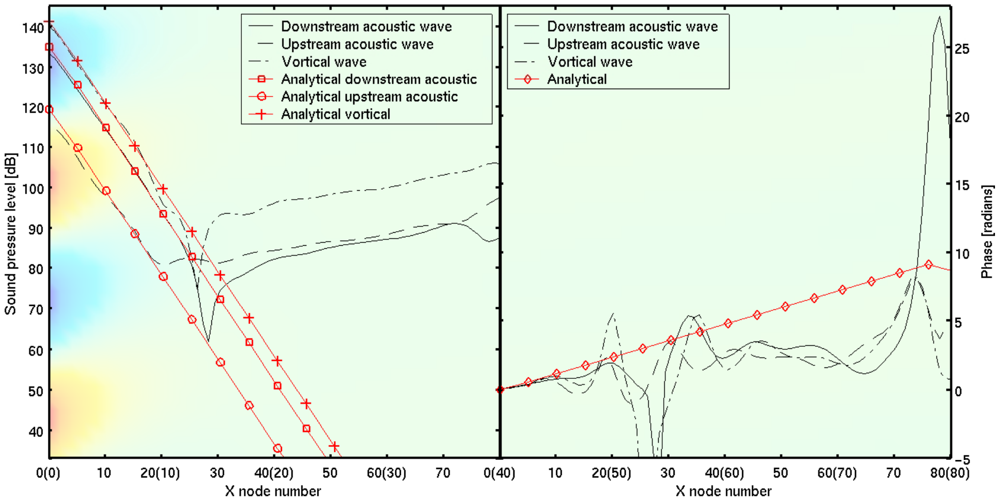

Figure 28. $\xi = 0.9$. Constant flow parameters: $N_\theta = 20$ and $M = 0.4$. Downstream.

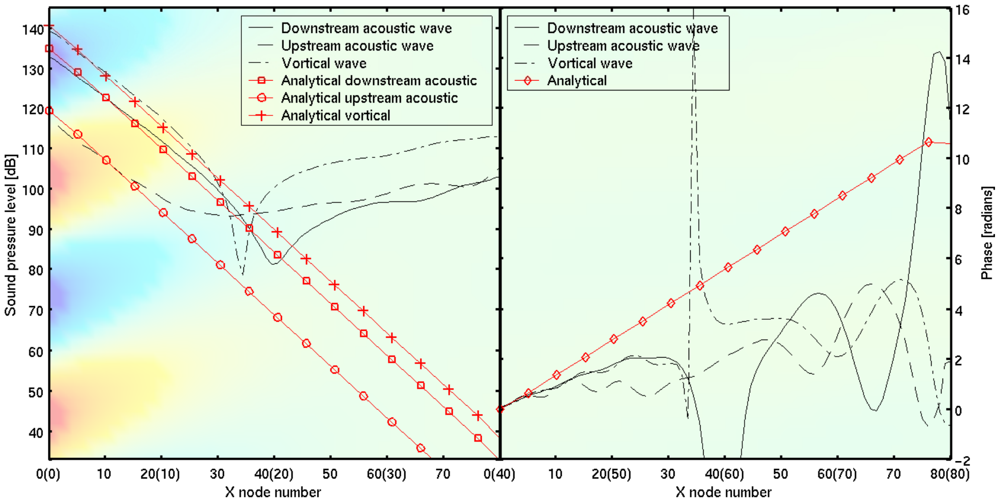

Figure 29. $\xi = 1.1$. Constant flow parameters: $N_\theta = 20$ and $M = 0.4$. Downstream.

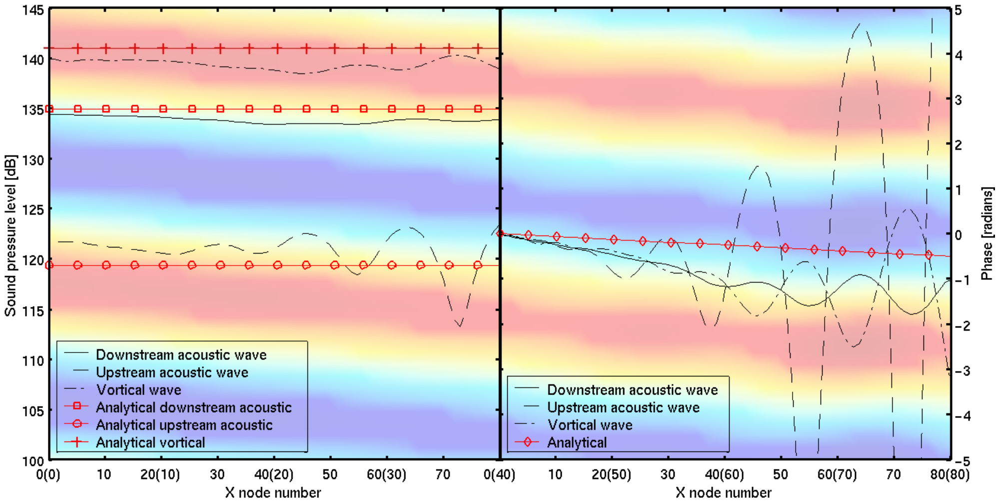

The corresponding figures for the upstream traveling wave (flow is still going from left to right, but the acoustic wave is imposed at the right boundary and traveling upstream the flow) can be found in Appendix B.2.

Figure 30. $\xi = 1.5$. Constant flow parameters: $N_\theta = 20$ and $M = 0.4$. Downstream.

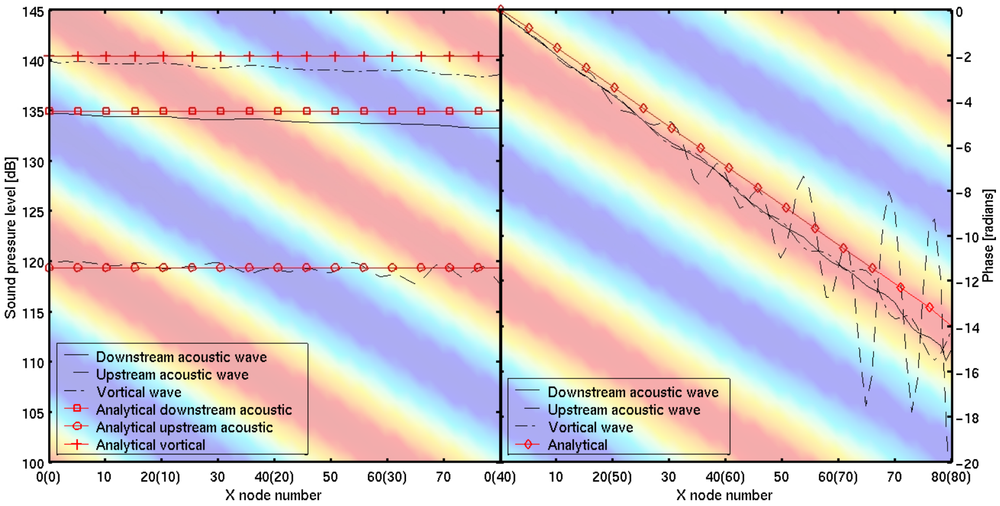

Figure 31. $\xi = 3.0$. Constant flow parameters: $N_\theta = 20$ and $M = 0.4$. Downstream.

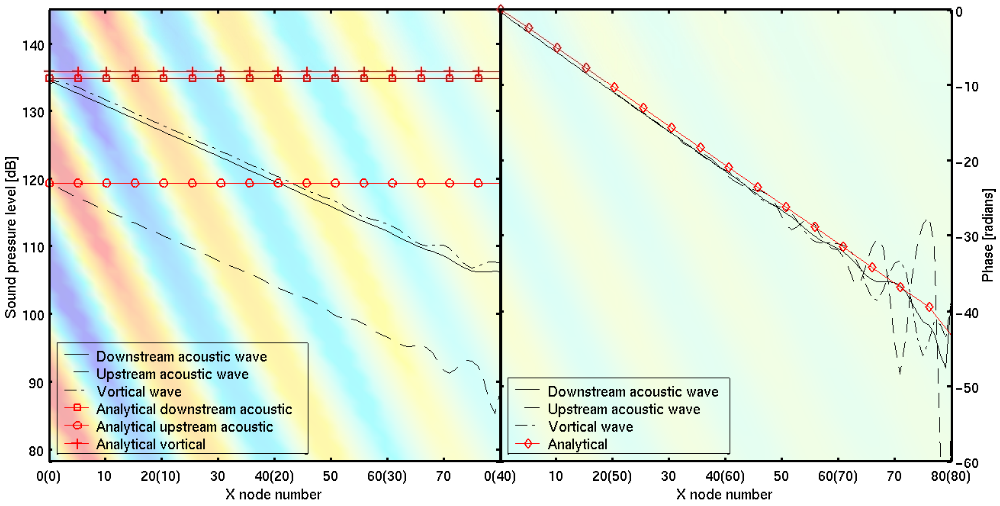

Figure 32. $\xi = 5.0$. Constant flow parameters: $N_\theta = 20$ and $M = 0.4$. Downstream.

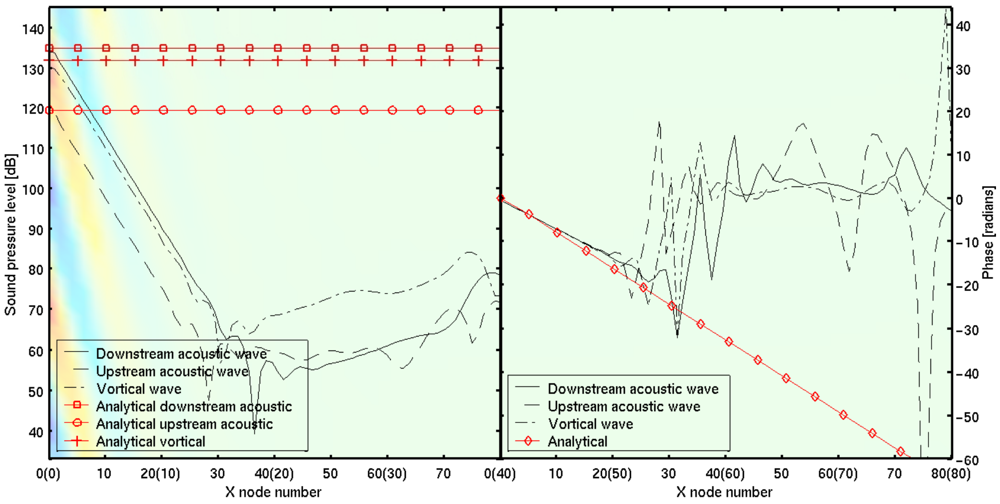

8.5.3 Variation of Mach number M

In this section the result from variation of the Mach number M is presented . The other parameters are kept constant with the default values, see Table 1.

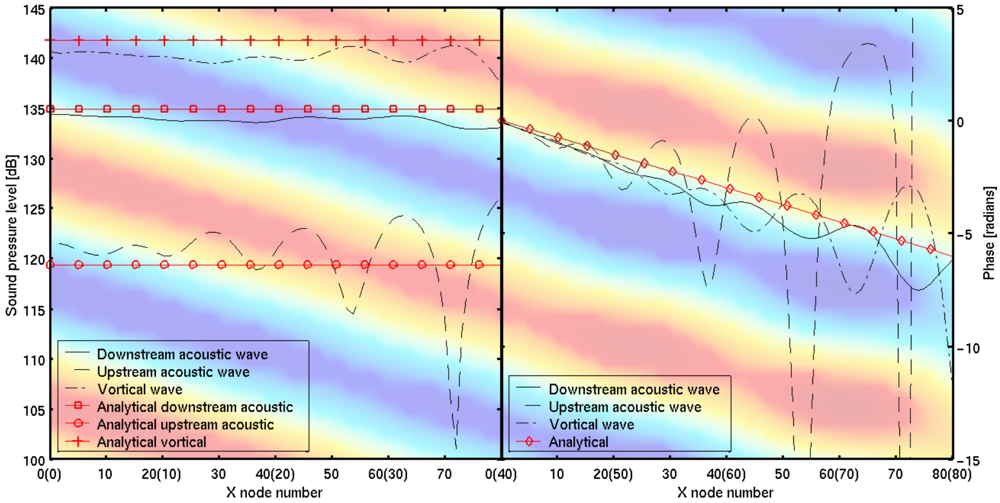

Figure 33. $M = 0.2$. Constant flow parameters: $N_\theta = 20$ and $\xi = 1.1$. Downstream.

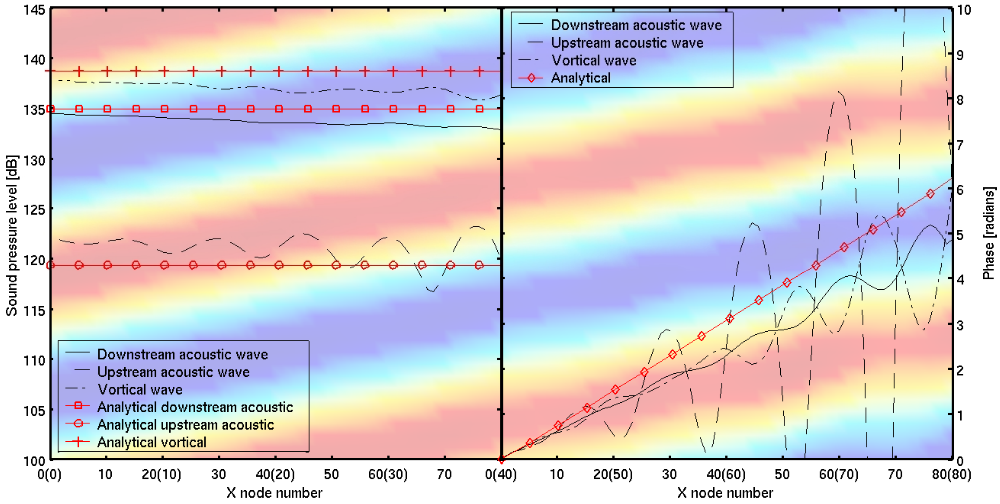

Figure 34. $M = 0.6$. Constant flow parameters: $N_\theta = 20$ and $\xi = 1.1$. Downstream.

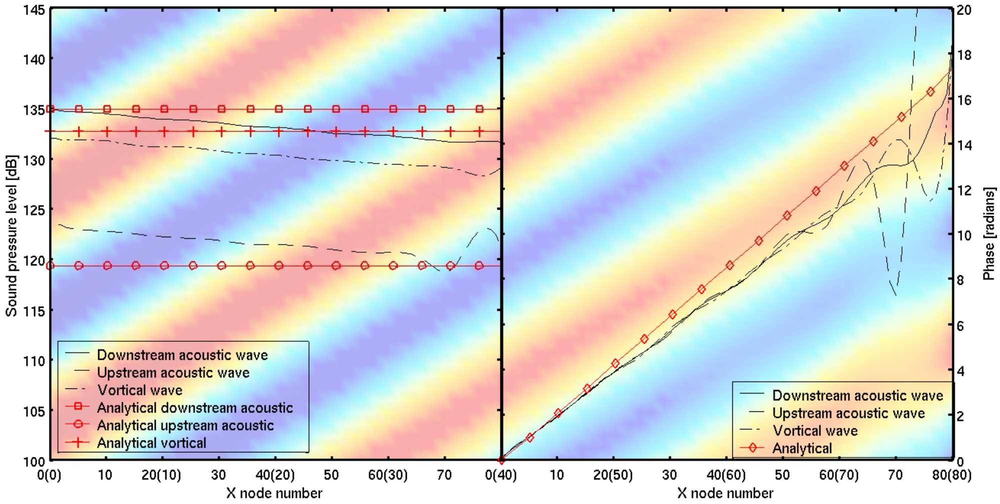

Figure 35. $M = 0.8$. Constant flow parameters: $N_\theta = 20$ and $\xi = 1.1$. Downstream.

Going from low to high Mach number one should notice the enhanced influence of numerical dissipation. This is a direct result of a decrease in axial wavelength, see (19). A decrease in axial wavelength means that the resolution, points per wavelength, in x is less, and Figure 20 holds. At low mach number, the reflections from the boundary conditions are very clearly seen as the wiggly nature of the acoustic waves. These reflections are present because one has to perform many iterations – compared to high-Mach number runs – to ensure that the flow has moved throughout the domain.

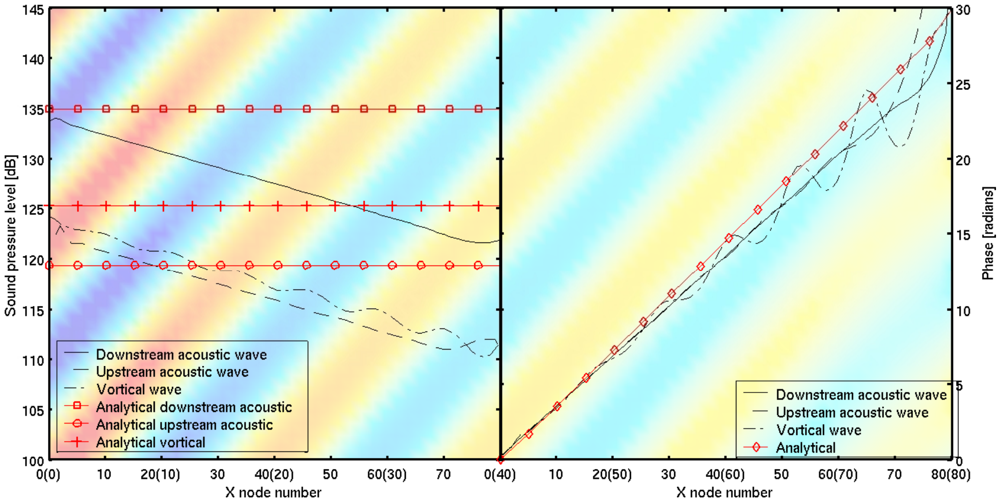

Figure 36. $M = 0.9$. Constant flow parameters: $N_\theta = 20$ and $\xi = 1.1$. Downstream.

The corresponding figures for the upstream traveling wave can be found in Appendix B.3.

8.5.4 Summary and comparison of the result

The result of the flow dependent computations is summarized in Table 3.

Table 3. Result of axial damping error $\Delta\epsilon$ and axial phase error $\Delta\Theta$ for the flow dependent computations. The values are found by first-order curve-fitting above the 'noise floor' of the individual results.

Parameters				**Downstream**		**Upstream**	
	N_θ	ξ	M	$\Delta\epsilon_{ds}$ [dB]	$\Delta\Theta_{ds}$ [rad]	$\Delta\epsilon_{us}$ [dB]	$\Delta\Theta_{us}$ [rad]
N_θ	5	1.1	0.4	1.3639	0.4006	5.0287	0.8415
	10	1.1	0.4	0.1429	0.0902	0.9793	0.0114
	20	1.1	0.4	0.0066	0.0155	0.0461	0.0044
	40	1.1	0.4	0.0006	0.0010	0.0119	0.0005
	80	1.1	0.4	0.0004	0.0004	0.0089	0.0006
	160	1.1	0.4	0.0003	0.0003	0.0060	0.0003
ξ	20	0.7	0.4	0.1127	0.0156	0.0382	0.0472
	20	0.9	0.4	0.2011	0.0370	0.0089	0.0233
	20	1.1	0.4	0.0066	0.0155	0.0461	0.0044
	20	1.5	0.4	0.0176	0.0132	0.3318	0.0269
	20	3.0	0.4	0.3781	0.0220	4.1503	0.8224
	20	5.0	0.4	2.3045	0.3144	7.2253	1.9403
M	20	1.1	0.2	0.0102	0.0096	0.0265	0.0111
	20	1.1	0.4	0.0066	0.0155	0.0461	0.0044
	20	1.1	0.6	0.0183	0.0173	1.0608	0.0557
	20	1.1	0.8	0.0446	0.0278	1.6541	0.2718
	20	1.1	0.9	0.1644	0.0321	2.3408	0.6075

The results of the cut-on waves (see Figure 37 and 38) for the combinations of points per wavelength N_θ and cut-off ratio ξ show many interesting features.

Firstly, the amplitude errors are strongly dependent of points per wavelength N_λ, but is not much affected by the cut-off ratio (the points are generally grouped around the fitted curve – with the exception of the downstream $\xi = 1.1\,\mathrm{new}$, see Figure 37(a)). The line $\xi = 1.1\,\mathrm{new}$ represents a CFD-result from a refined version of the solver, and as one can see it indicates a better result. Some possible explanations to this might be that the viscosity terms of the Navier-Stokes equation begins to dominate, or reflections from outflow boundary condition, or time integration error, or it might also be that the sensitivity of the post-processing was not good enough. It is also likely that several of these results have been calculated before the flow had converged to fully periodic in the whole domain. However, we expect that the errors will decrease in the same way as for $\xi = 1.1\mathrm{new}$ when fully converged solutions are considered. Note that the results from upstream waves are in general worse than downstream waves, which is mainly because the axial wavelength N_x is less.

Figure 37. Downstream, cut-on ($\xi > 0$ only). Amplitude error (left) and phase error (right) development as a function of the average points per theoretical wavelength.

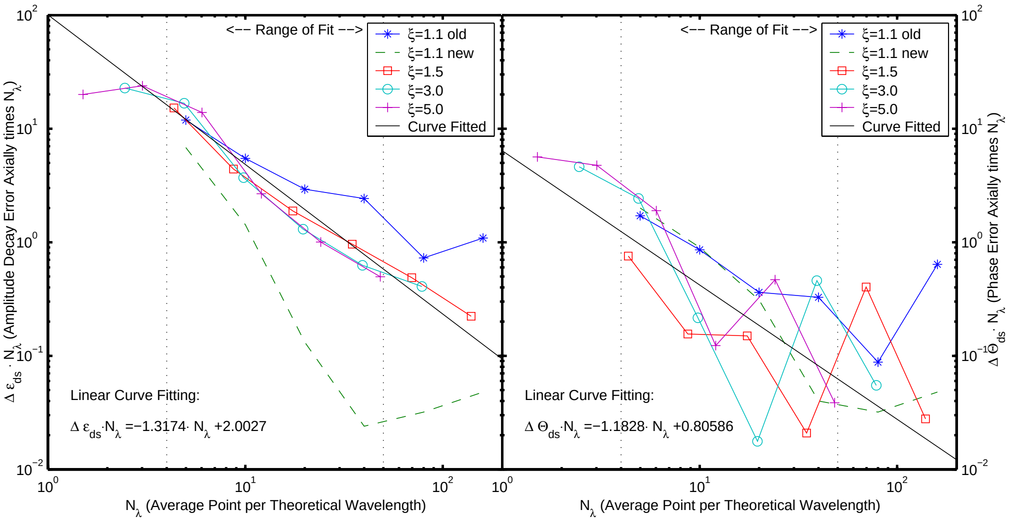

Figure 38. Upstream, cut-on ($\xi > 0$ only). Amplitude error (left) and phase error (right) development as a function of the average points per theoretical wavelength.

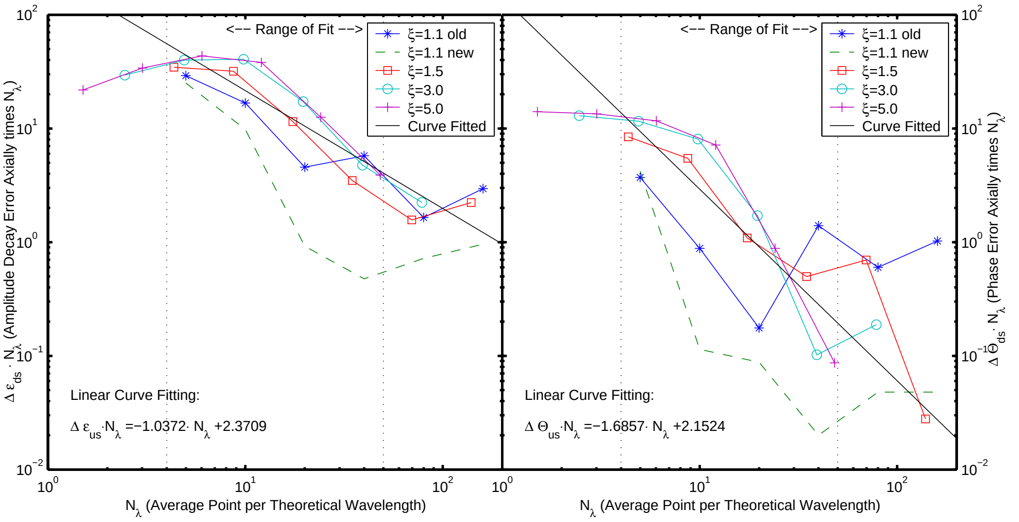

Secondly, the phase errors (see Figure 37(b) and 38(b)) is more spurious than the amplitude decay errors, but a rough curve fitting is done in order to grip some indications of the phase error development. It is difficult to draw any conclusions, but the trend is more or less the same as for the amplitude decay. The error seems to be indefinable from about $N_\lambda = 30$ up to higher resolutions – the reason for this is unknown.

Cut-off waves could be thought of as not being of significant interest since they decay naturally and will generally not contribute to the far-field. However, in a compressor or turbine, the blades are closely spaced, and because of this there could be interaction where energy can be exchanged between cut-off and cut-on waves, as well as cut-off waves can

Figure 39. Development of amplitude error (left) and phase errors (right) as a function of the Mach number.

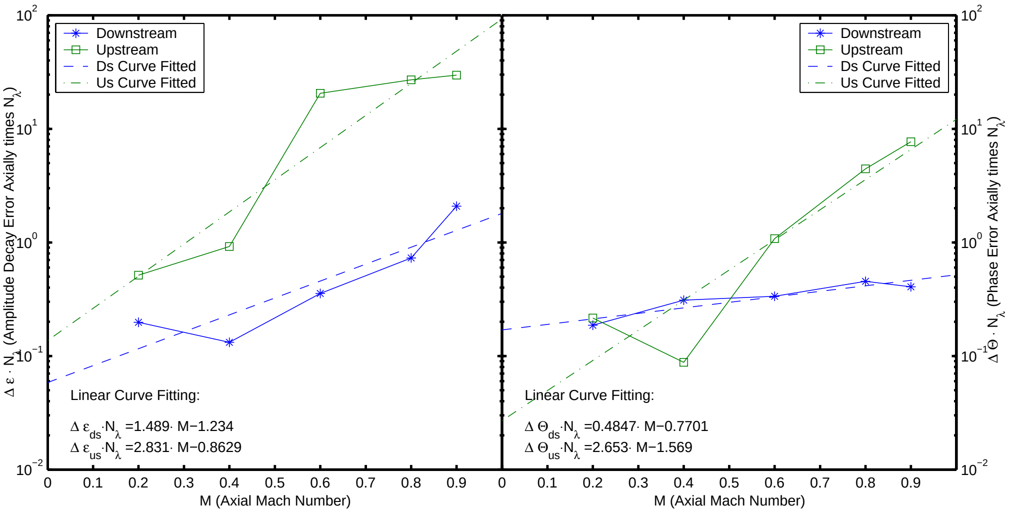

become cut-on also with varying Mach number. In Appendix B.3 the Figure 78 and 79 show the cut-off waves in similar plots to the cut-on waves. The amplitude and phase errors are far from as good as for cut-on waves, and are not in consistence. For instance, the phase error of the upstream wave, Figure 79(b), shows a positive inclination that indicates an increase in error with increased resolution. The reason for this is unknown, but errors could have occurred when the wavesplitting is applied in the post-processing.

Mach number variations show differences in dissipation and dispersion errors as well, see Figure 39. Both amplitude decay and phase errors are increasing with increasing Mach number. For downstream waves this occurs mainly because a higher Mach number reduces the axial wavelength, and therefore also the axial wave resolution N_x (and N_λ), see Eq. (19). This is also true for the upstream waves as well, for which N_x is generally smaller than for downstream waves, and the amplitude decay errors are therefore larger here too.

8.6 Influence of code dependent parameter variations

Table 4. Range of study for the code dependent parameters. Note that number of runs is the double of the number variations. For each combination, there are two runs; upstream- and downstream-imposed waves respectively. Calculations of the default value (see Table 1) are coved by the runs in Section 8.5. † Used on acoustic outflow only.

Symbol	Default	Range of Study	Variations
N_t	40	20, 80	2 variations and 4 runs
$\sigma^{(2)}$	1.0	0, 0.50, 2.0	3 variations and 6 runs
$\sigma^{(4)}$	0.1	0, 0.05, 0.2	3 variations and 6 runs
$\kappa^{(2)}$	1.0	0, 0.50, 2.0	3 variations and 6 runs
$\kappa^{(4)}$	0.1	0, 0.05, 0.2	3 variations and 6 runs
$\mathrm{Re}_{\mathrm{tu}}$	$5\cdot 10^5$	$1\cdot 10^5$	1 variation and 2 runs
b.c.	Giles†	Riemann	1 variation and 2 runs

The code dependent variables involves the parameters N_t, $\sigma^{(2)}$, $\sigma^{(4)}$, $\kappa^{(2)}$, $\kappa^{(4)}$ and $\mathrm{Re}_{\mathrm{tu}}$ (see Table 1). In Table 4 the range of study is given. The total number of runs will be 30, since there are two runs for each of the combinations; downstream and upstream traveling waves.

Few figures have been included in this section, most of the phenomena that occur here are of little effect and is not visible on a figure. All the results have been summarized at the end of this section, only a handful figures that have a clearly comparable and visible phenomena is included. We refer to Table 5 for the results instead.

8.6.1 Variation of time steps N_t per period in time

In this section the result of the effect from variation of the number of point per period in time is presented. The default flow parameters are used, see Table 1.

From the figures in this section on can notice the increased damping as the number of time steps per period is decreased.

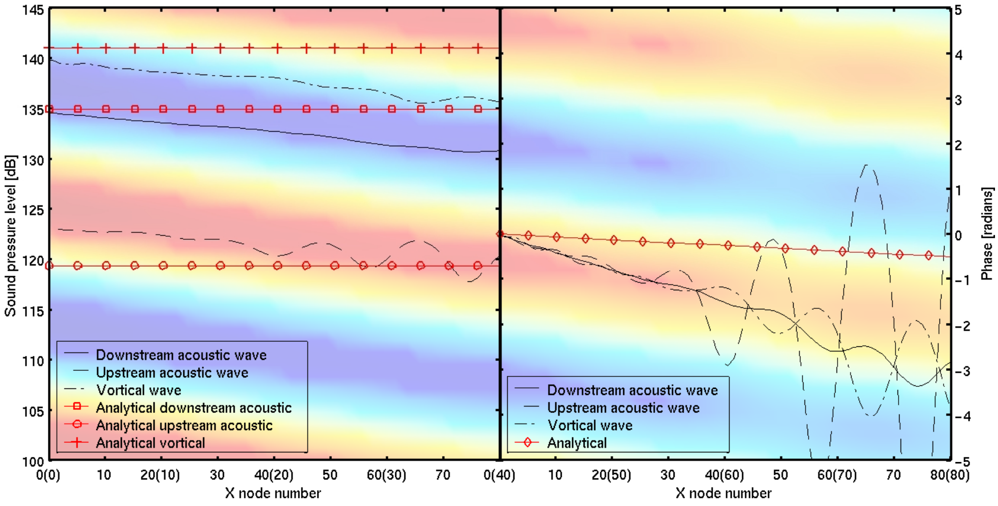

Figure 40. $N_t = 20$. Downstream. Flow parameters: $N_\theta = 20$, $\xi = 1.1$ and $M = 0.4$.

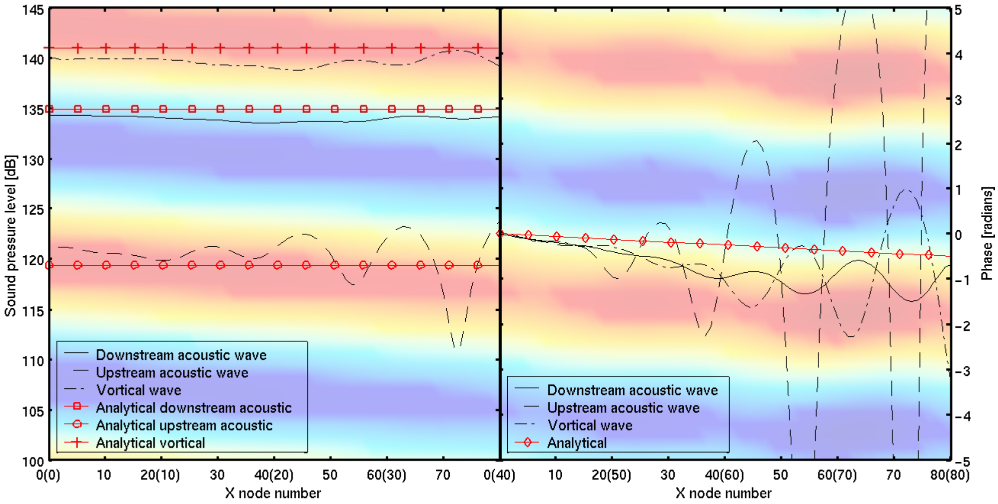

Figure 41. $N_t = 80$. Downstream. Flow parameters: $N_\theta = 20$, $\xi = 1.1$ and $M = 0.4$.

The corresponding figures for the upstream traveling wave (flow is still going from left to right, but the acoustic wave is imposed at the right boundary and traveling upstream the flow) can be found in Appendix C.1.

8.6.2 Variation of mean flow artificial viscosity $\sigma^{(2)}$ and $\sigma^{(4)}$

In this section the result of the effect from variation of artificial is presented. The default flow parameters are used, see Table 1.

Figure 42. $\sigma^{(4)} = 0$. Downstream. Flow parameters: $N_\theta = 20$, $\xi = 1.1$ and $M = 0.4$.

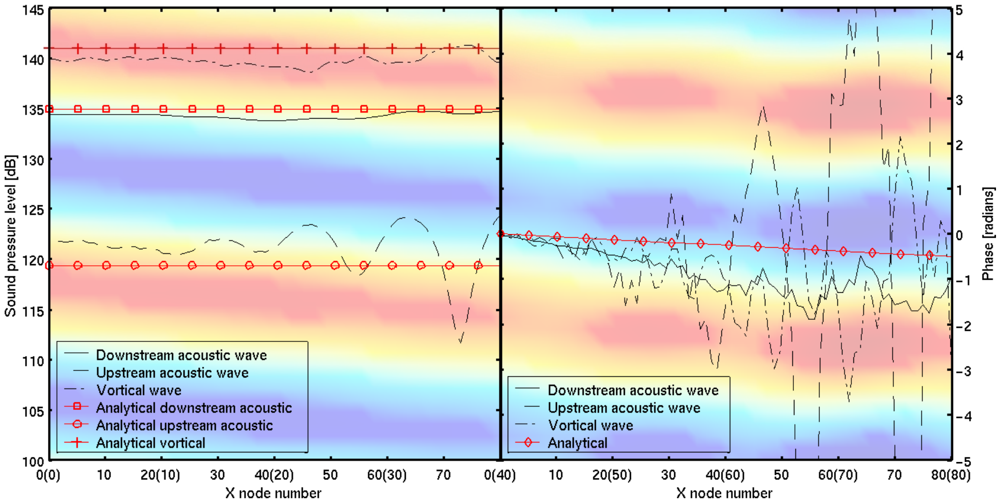

Figure 43. $\sigma^{(4)} = 0.2$. Downstream. Flow parameters: $N_\theta = 20$, $\xi = 1.1$ and $M = 0.4$.

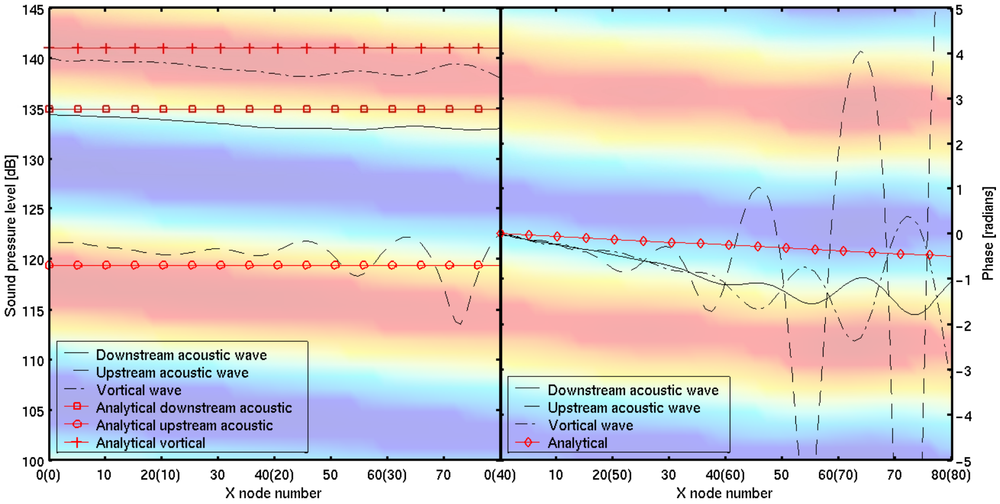

There were seen minimal effect of changing the amount of second-order artificial viscosity $\sigma^{(2)}$, and no figures are included from this variation here. For downstream waves variation of $\sigma^{(2)}$ had no effect at all, but for upstream waves the amplitude decay error and phase error imposed only minor changes.

Fourth-order artificial viscosity $\sigma^{(4)}$, on the other hand, had relatively larger effect than $\sigma^{(2)}$. From the figures in this section one can see that the small oscillations that is on the order of the grid points occurs, and damps the wave.

8.6.3 Variation of turbulent artificial viscosity $\kappa^{(2)}$ and $\kappa^{(4)}$

No effects of changing the turbulent artificial viscosity parameter were seen on neither the downstream waves nor the upstream waves. The reason for this is probably because the viscous terms are small, and therefore also the kinetic energy of the turbulent vorticities is small. See Table 5 for comparison. Since no hard walls are present in the computational domain, it was expected that the viscosity should be neglected. Moreover, when walls are present, viscous effect will be dominating in boundary layers.

8.6.4 Euler calculation

To ensure that viscosity effect was small, an Euler-calculation was also performed. This showed exactly the same properties as the Navier-Stokes-calculation, for $N_\theta = 20$ see Section C.2 for an upstream computation.

Figure 44. Euler calculation. Downstream. Flow parameters: $N_\theta = 20, \xi = 1.1$ and $M = 0.4$.

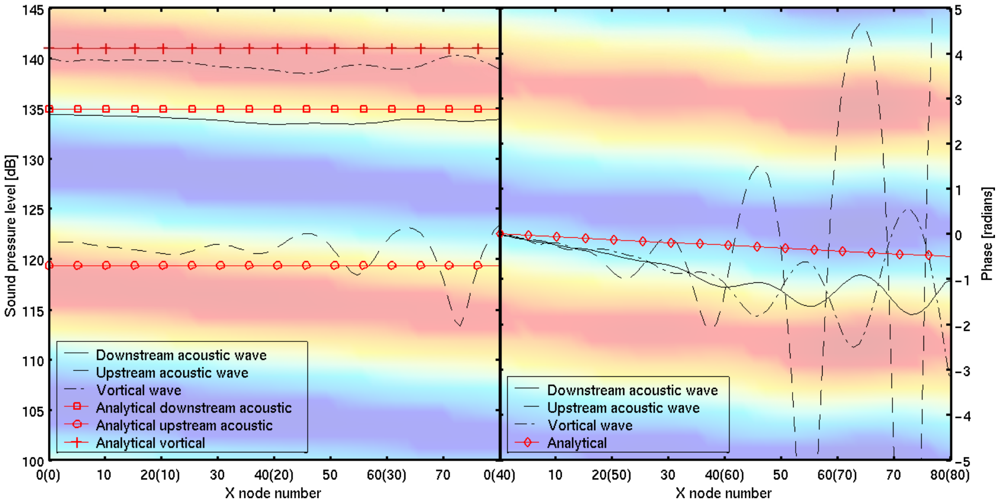

8.6.5 Variation of turbulent Reynolds number

No effect could be seen when changing the turbulent Reynolds number to $1 \cdot 10^5$ from the default value of $9.22 \cdot 10^5$. Of the same reason as for variation of $\kappa^{(2)}$ and $\kappa^{(4)}$, the production of turbulence is small due to the absence of large viscous terms.

8.6.6 Summary and comparison of the result

The result of the code dependent computations is summarized in Table 5. The only variables that imposes a noticable change is the time step N_t and forth-order artificial viscosity-term $\sigma^{(4)}$.

Table 5. Result of axial damping error $\Delta\epsilon$ and axial phase error $\Delta\Theta$ for the code dependent computations. The values are found by 1st-order curve-fitting above the 'noise floor' of the individual results.

Parameter		**Downstream**		**Upstream**	
		$\Delta\epsilon_{ds}$ [dB]	$\Delta\Theta_{ds}$ [rad]	$\Delta\epsilon_{us}$ [dB]	$\Delta\Theta_{us}$ [rad]
Default run		0.0066	0.0155	0.0461	0.0044
N_t	20	0.0525	0.0349	0.1194	0.0230
	80	0.0024	0.0073	0.0358	0.0026
$\sigma^{(2)}$	0	0.0066	0.0155	0.0461	0.0044
	0.5	0.0066	0.0155	0.0463	0.0043
	2.0	0.0066	0.0155	0.0464	0.0041
$\sigma^{(4)}$	0	0.0020	0.0178	0.0129	0.0054
	0.05	0.0038	0.0143	0.0221	0.0045
	0.20	0.0190	0.0123	0.1996	0.0046
$\kappa^{(2)}$	0	0.0066	0.0155	0.0461	0.0044
	0.5	0.0066	0.0155	0.0461	0.0044
	2.0	0.0066	0.0155	0.0461	0.0044
$\kappa^{(4)}$	0	0.0066	0.0155	0.0461	0.0044
	0.05	0.0066	0.0155	0.0461	0.0044
	0.20	0.0066	0.0155	0.0461	0.0044
N-S	Euler	0.0064	0.0119	0.0466	0.0054
Re_{tu}	$1 \cdot 10^5$	0.0089	0.0120	0.0506	0.0128

Figure 45. Development of amplitude error (left) and phase errors (right) as a function of the points per period in time N_t.

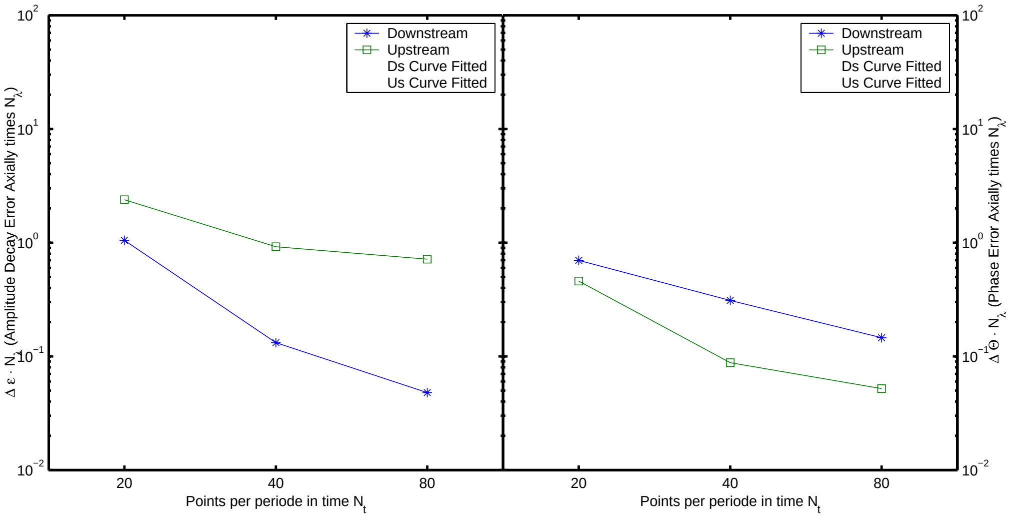

Figure 46. Development of amplitude error (left) and phase errors (right) as a function of the artificial parameter σ. The x-axis represent zero, half, default and double values.

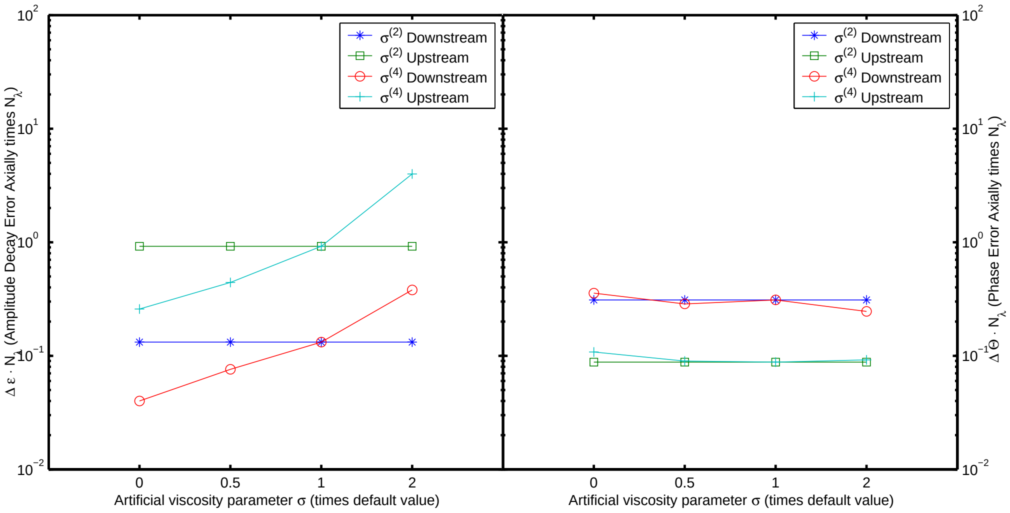

8.7 Influence from grid dependent parameter variations

The grid dependent variables involves the parameters $\frac{\Delta x}{\Delta y}$, $\frac{\Delta x_{j+1}}{\Delta x_j}$, α and Circumferential Distribution (see Table 1). In Table 6 the range of study is given. The total number of runs will be 22, since there are two runs for each of the combinations; downstream and upstream traveling waves.

Table 6. Range of study for the grid dependent parameters. Note that number of runs is the double of the number variations. For each combination there are two runs; upstream- and downstream-imposed waves respectively. Calculations of the default value (see Table 1) are coved by the runs in Section 8.5.

Symbol	**Default**	**Range of Study**	**Variations**
$\frac{\Delta x}{\Delta y}$	1.0	0.50, 2.0	2 variations and 4 runs
$\frac{\Delta x_{j+1}}{\Delta x_j}$	1.1	$\frac{1}{1.4}$, $\frac{1}{1.1}$, 1.1, 1.4	4 variations and 8 runs
α	0.0	-70°, -35°, 35°, 70°	4 variations and 8 runs
CircDist	Uniform	End biased	1 variations and 2 runs

8.7.1 Variation of Cell Aspect Ratio $\frac{\Delta x}{\Delta y}$

In this section the result from variation of the Cell Aspect Ratio is presented. The other parameters are kept constant with the default values, see Table 1.

The corresponding figures for the upstream traveling wave can be found in Appendix D.1.

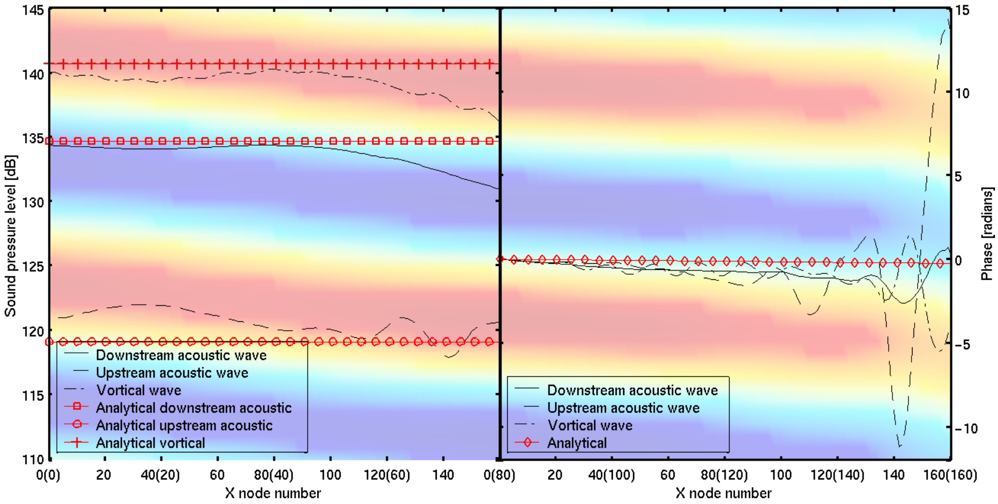

Figure 47. Downstream. Cell Aspect Ratio, $\frac{\Delta x}{\Delta y} = 0.5$. $N_\theta = 20$, $\xi = 1.1$ and $M = 0.4$. See Figure 12(b).

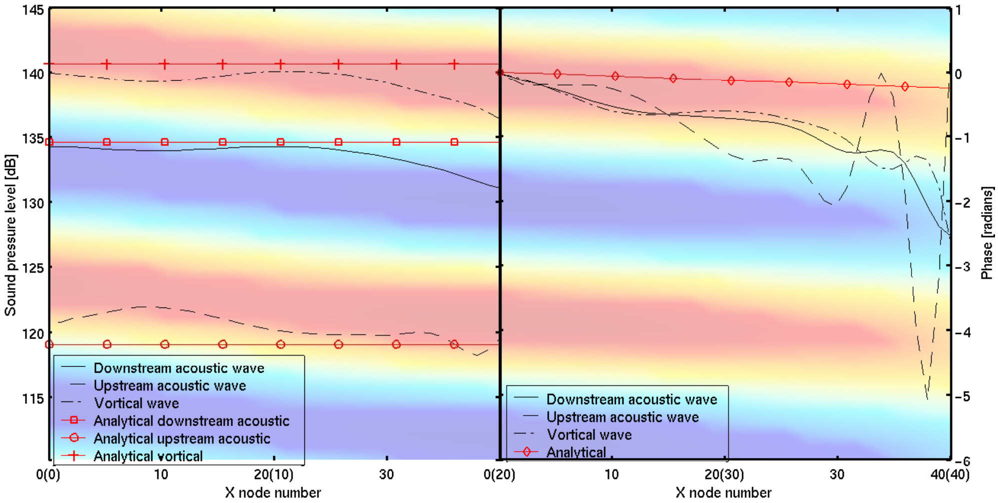

Figure 48. Downstream. Cell Aspect Ratio, $\frac{\Delta x}{\Delta y} = 2$. $N_\theta = 20$, $\xi = 1.1$ and $M = 0.4$. See Figure 12(b).

8.7.2 Variation of Axial Grid Stretching Ratio $\frac{\Delta x_{j+1}}{\Delta x_j}$

In this section the result from variation of the Axial Grid Stretching Ratio is presented. The other parameters are kept constant with the default values, see Table 1. Only two

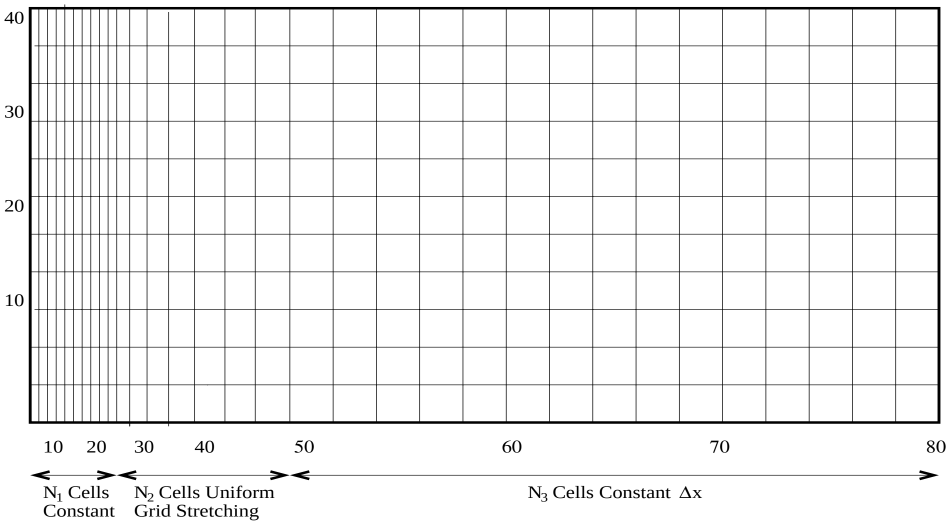

Figure 49. Schematic of the Axial Grid Stretching case

different runs are shown, $\frac{1}{1.4}$ and 1.4.

Table 7. Parameters for the Axial Grid Stretching Ratio test case.

Stretching Parameters $\frac{\Delta x_{j+1}}{\Delta x_j}$	**N1**	**N2**	**N3**	$\frac{\Delta x_{\text{start}}}{\Delta y}$	$\frac{\Delta x_{\text{end}}}{\Delta y}$
$\frac{1}{1.4}$	35	10	35	1.0	$\frac{1}{28.925}$
$\frac{1}{1.1}$	25	30	25	1.0	$\frac{1}{17.449}$
1.1	25	30	25	$\frac{1}{17.449}$	1.0
1.4	35	10	35	$\frac{1}{28.925}$	1.0

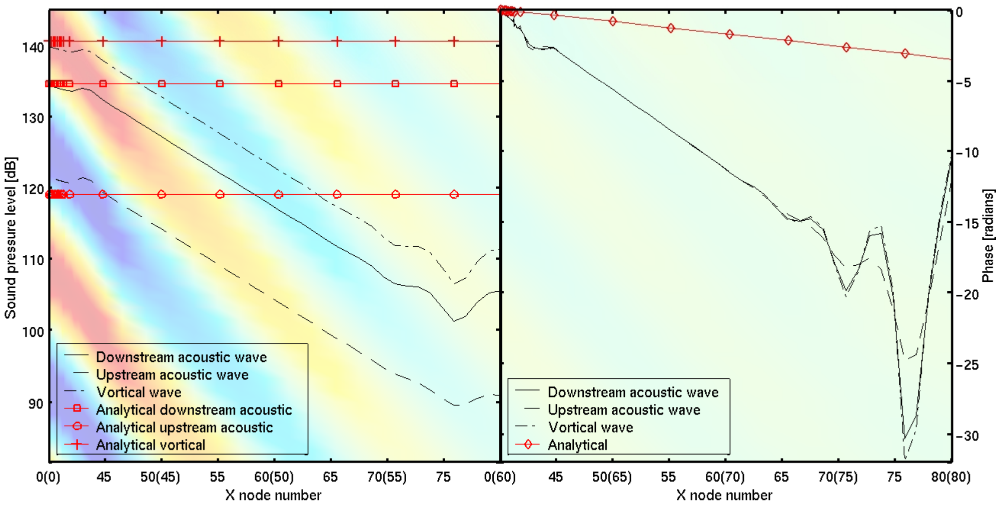

Figure 50. Downstream. Grid Stretching Ratio, $\frac{\Delta x_{j+1}}{\Delta x_j} = \frac{1}{1.4}$. $N_\theta = 20, \xi = 1.1$ and $M = 0.4$. See Figure 49.

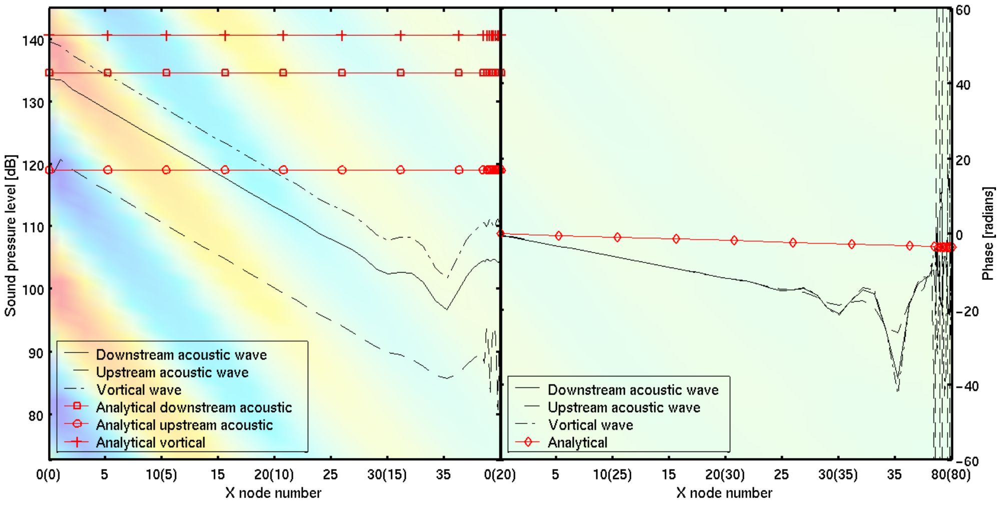

Figure 51. Downstream. Grid Stretching Ratio, $\frac{\Delta x_{j+1}}{\Delta x_j} = 1.4$. $N_\theta = 20, \xi = 1.1$ and $M = 0.4$. See Figure 49.

8.7.3 Variation of Skew Angle

In this section the result from variation of the Skew Angle is presented. The other parameters are kept constant with the default values, see Table 1. Only the Skew Angles of $\alpha = 35°$ and $-35°$ is shown.

The corresponding figures for the upstream traveling wave (flow is still going from left to right, but the acoustic wave is imposed at the right boundary and traveling upstream the flow) can be found in Appendix D.2. Here the axial wavenumber is much less than for downstream waves, giving less resolution which then induces numerical damping.

Figure 52. Schematic of the Skew Angle case

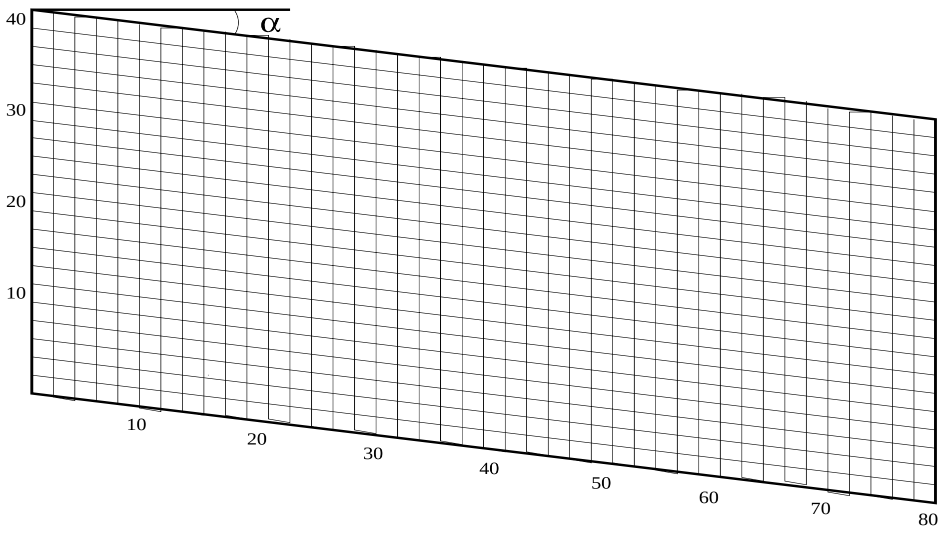

Figure 53. Downstream. $\alpha = 35°$. $N_\theta = 20$, $\xi = 1.1$ and $M = 0.4$. See Figure 52.

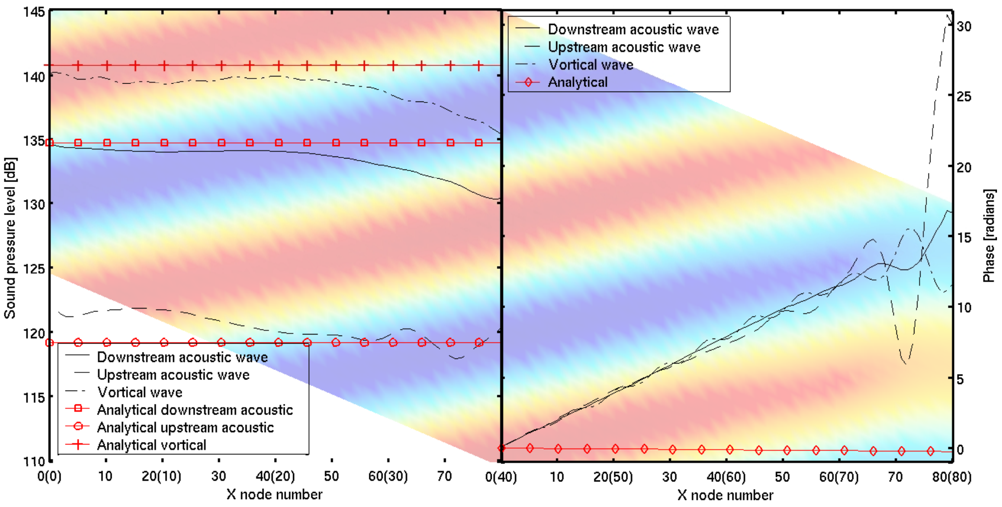

Figure 54. Downstream. $\alpha = -35°$. $N_\theta = 20$, $\xi = 1.1$ and $M = 0.4$. See Figure 52.

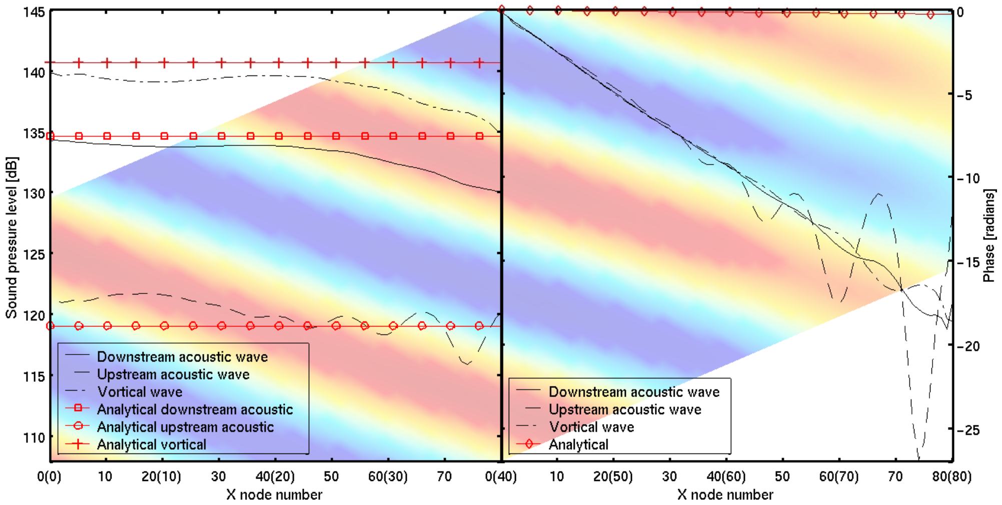

An important feature of the skew angle, is that the axial wavelength across the skew is larger for downstream waves than for upstream waves (see Appendix D.2). This causes the numerical dissipation for upstream waves at positive skew angles to become large.

8.7.4 Variation of Circumferential Distribution

In this section the result from variation of the Circumferential Distribution is presented. The other parameters are kept constant with the default values, see Table 1.

Figure 55. Schematic of the Skew Angle case

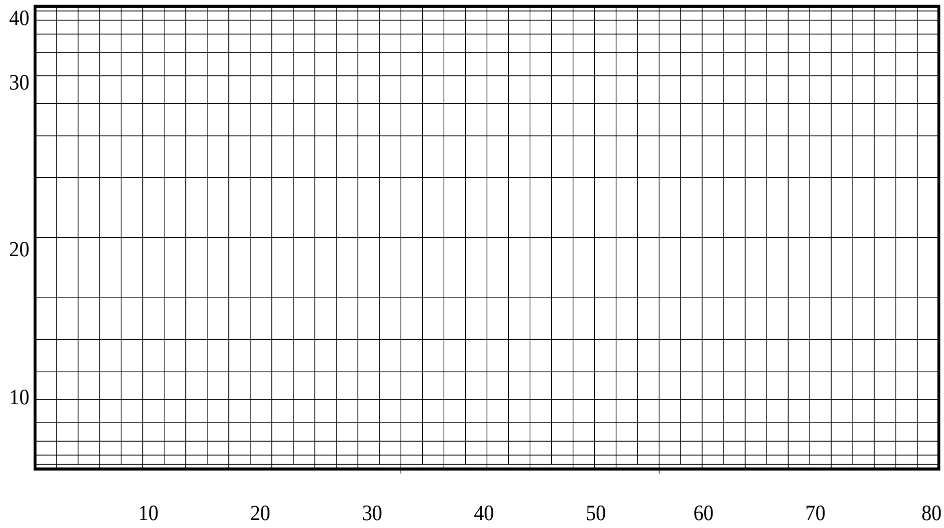

This test case is set to model the passage within a blade row where points may be closely spaced near the blades (taking account to the boundary layer), and coarser in the middle. The circumferential spacing is proportional to

$$\Delta y_j = e^{-\frac{12}{n^2}\left(j-\frac{n+1}{2}\right)^2}$$

where $n = 40$ is the number of cells in the y-direction.

Figure 56. Downstream. Non-Uniform Grid in y-direction. $N_\theta = 20$, $\xi = 1.1$ and $M = 0.4$. See Figure 55.

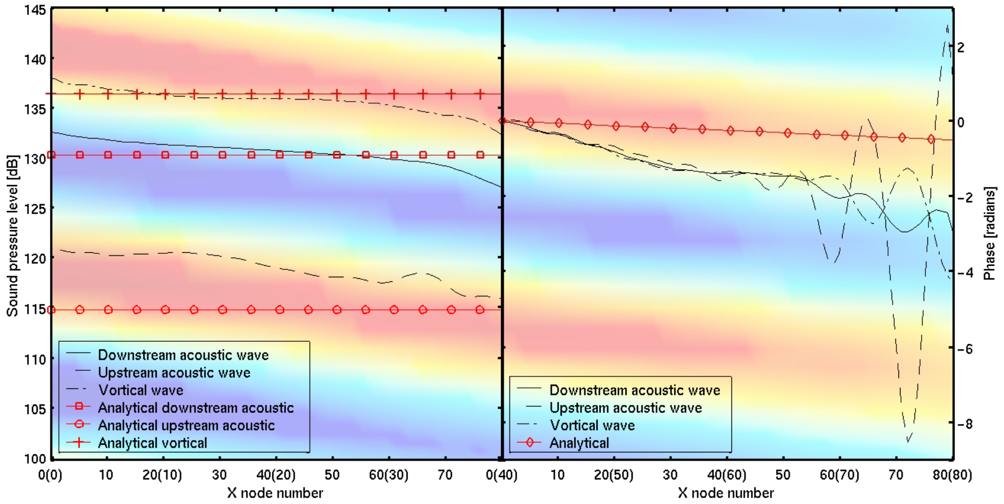

The corresponding figure for the upstream traveling wave (flow is still going from left to right, but the acoustic wave is imposed at the right boundary and traveling upstream the flow) can be found in Appendix D.3.

8.7.5 Summary and comparison of the result

The result of the grid dependent computations is summarized in Table 8.

Table 8. Result of axial damping error $\Delta\epsilon$ and axial phase error $\Delta\Theta$ for the grid dependent computations. The values are found by first-order curve-fitting above the 'noise floor' of the individual results.

Parameter		**Downstream**		**Upstream**	
		$\Delta\epsilon_{ds}$ [dB]	$\Delta\Theta_{ds}$ [rad]	$\Delta\epsilon_{us}$ [dB]	$\Delta\Theta_{us}$ [rad]
Default run		0.0066	0.0155	0.0461	0.0044
$\frac{\Delta x}{\Delta y}$	0.5	0.0013	0.0060	0.0042	0.0039
	2.0	0.0057	0.0225	0.5350	0.0959
$\frac{\Delta x_{j+1}}{\Delta x_j}$	$\frac{1}{1.4}$	0.0333	0.0146	0.3395	0.3008
	$\frac{1}{1.1}$	0.0185	0.0155	0.4412	0.2935
	1.1	0.0189	0.0107	0.1284	0.0642
	1.4	0.0376	0.0139	0.2230	0.1954
α	-70°	2.0219	0.6355	0.2823	0.8065
	-35°	0.0090	0.2277	0.0131	0.2087
	35°	0.0074	0.2044	0.1278	0.1903
	70°	0.9421	0.7049	4.3278	0.2429
CircDist		0.0518	0.0276	0.1618	0.0377

The result of the cell aspect ratio study can be seen in Figure 57. The overall trend is as expected; for increasing aspect ratio (fewer grid point) the error is increasing. In the downstream direction, at a cut-off ratio of 1.1, the axial wavelength is large, and the number of grid points per axial wavelength is therefore large. The effect of increasing dissipation from numerical errors with increasing aspect ratio should then be negliable, which can be seen in the figure. Upstream wave, on the other hand, suffer from increased numerical dissipation at high aspect ratios, since the axial wavelength is small and the effect of dissipation from poor resolutet axial wave can not neglected.

Figure 57. Development of amplitude error (left) and phase errors (right) as a function of the Cell Aspect Ratio.

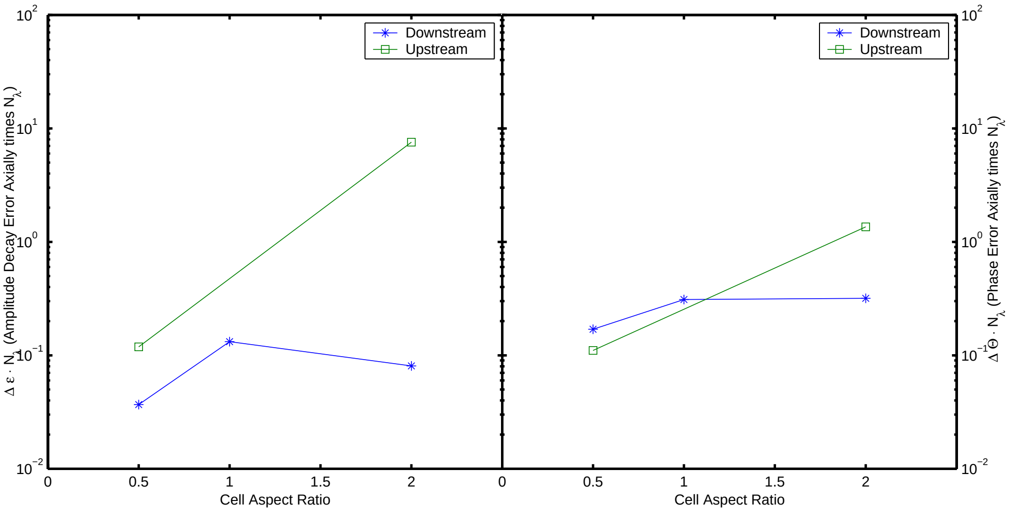

The result from the grid stretching study is shown in Figure 58. It is difficult to draw any conclusion from this, but it is clear that the grid stretching damps the acoustic wave.

Figure 59 shows the result of the skew angle study. At first sight, one observes that the upstream wave is asymmetrical around zero skew angle, and that the downstream wave is almost symmetrical. The reason for this is that the waves traveling with positive skew angle is considerably more attenuated that those traveling across the skew (negative skew angle). Since the result of that the points per wavelength across the skew is being greater that the points per wavelength with the skew, and is not accounted for in the calculation of N_λ. The downstream wave on the other hand show large numerical dissipation at high skew angles, but is instead symmetric. It is symmetric because the direction of the wavefront in these cases being close to the axial wavelength of these waves. Another important observation is that the minimum amplitude error is not at zero skew angle, but instead at $35°$ for downstream acoustic and at $-35°$ for upstream acoustic – it clearly depends on which direction the wave is traveling.

Figure 58. Development of amplitude and phase errors as a function of the Axial Grid Stretching study.

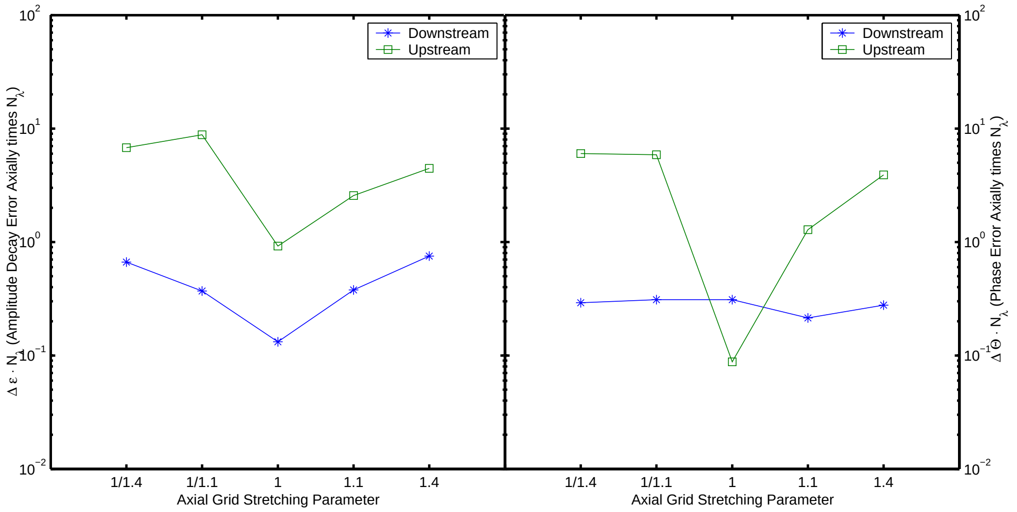

Figure 59. Development of amplitude and phase errors as a function of the Skew Angle α.

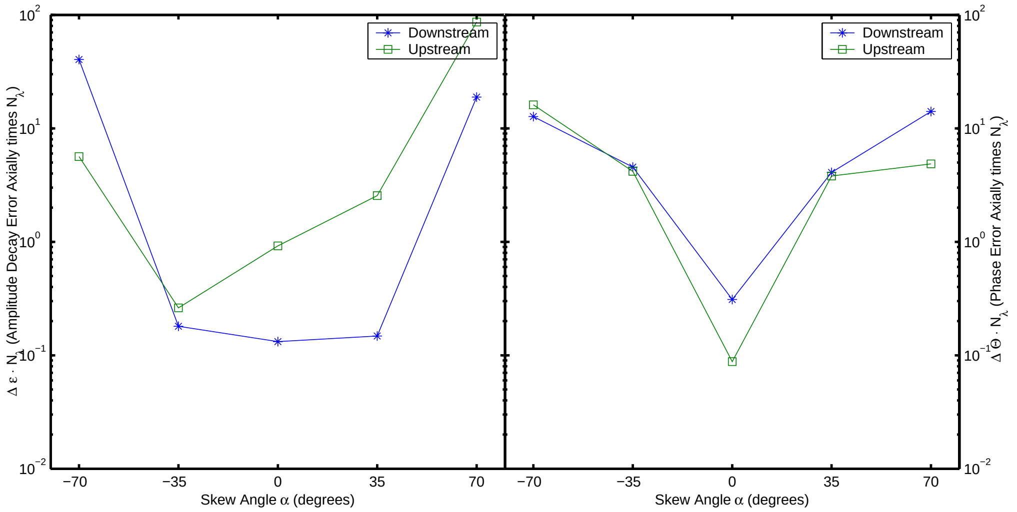

8.8 Evaluation of acoustic output boundary condition

In this section the result of the use of Riemann boundary condition at the acoustic output instead of Giles non-reflecting boundary condition. The default values, $N_\theta = 20$, $\xi = 1.1$ and $M = 0.4$ is used, see Table 1. The axes of the following figure are equal to make comparisons easier.

Wave reflections from the boundary are clearly visible when using Riemann conditions (Giles boundary condition also impose reflections, but in a much less extent). The downstream wave bounces at the right side of the domain, and back into the domain making the wave pattern wiggly. Assuming that linear theory is valid, the reflected wave will have the same wavenumber, k_x in (19), as the incoming wave except that it is in opposite direction, i.e. opposite sign:

$$k_{x,refl} = -k_x \tag{97}$$

When the reflected wave bounces back it will interfere with the original wave, and impose a phase shift as well as it will make the amplitude decay error wavy – positive and negative interference. Note that the downstream wave will not be affected before the

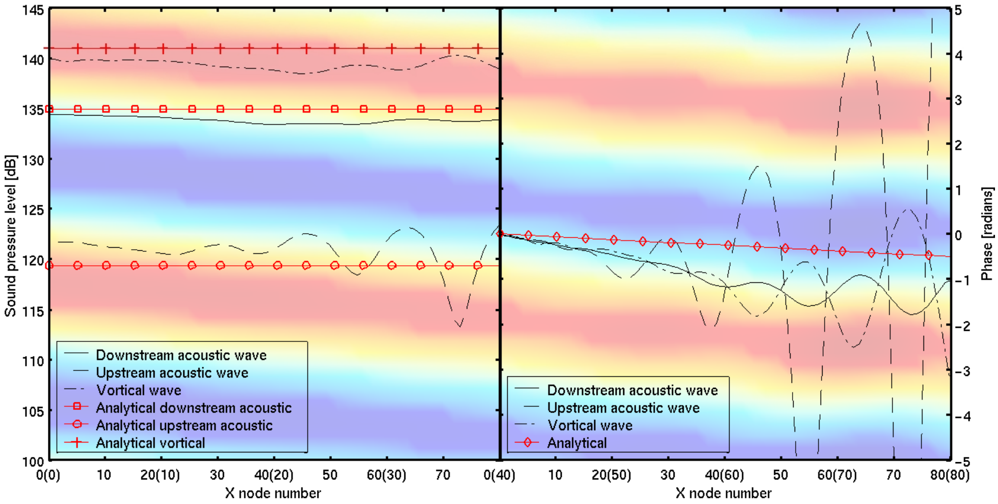

Figure 60. Downstream. Default parameters with Giles non-reflecting boundary condition at the acoustic output (right side of domain).

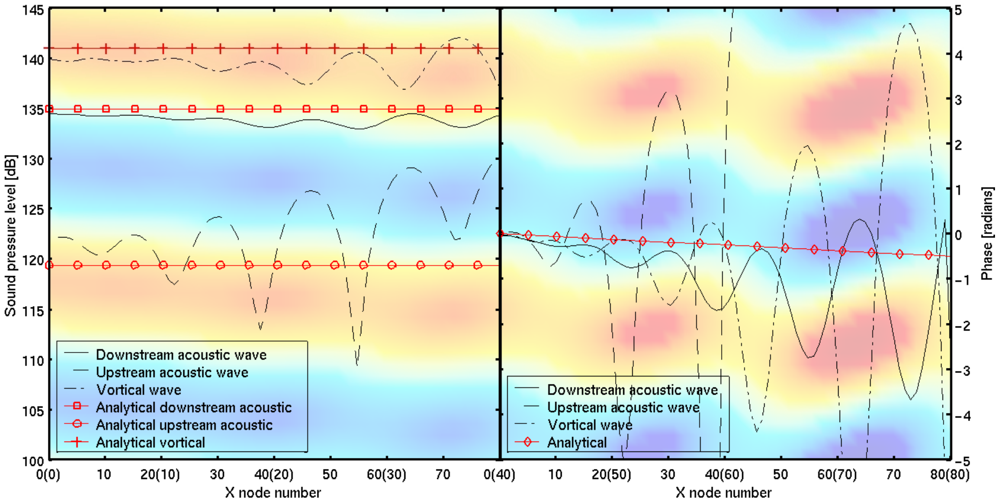

Figure 61. Downstream. Default parameters with Riemann boundary condition at the acoustic output (right side of domain).

reflections have reached the inflow boundary. A very rough estimate from the numerical results states that the amplitude decay error increases three to four times the amplitude decay error when using Giles boundary conditions.

The corresponding figures for the upstream traveling wave (flow is still going from left to right, but the acoustic wave is imposed at the right boundary and traveling upstream the flow) can be found in Appendix E.

8.9 Evaluation of iterations required for convergence

Followed by the discussion in the previous section, the important requirement of making an accurate estimate of how many iterations that is optimal to reduce errors must clarified. If too few iterations is performed, the flow have not reached the outflow boundary, and on the other hand if too many iterations is performed, the errors from reflected waves would be apparent.

This problem was not taken into account when choosing the optimal number of iterations. It is therefore expected that runs with large axial wavelength, which does not have a large axial damping, does not represent the correct result. When a large axial wave length is used, like for $\xi = 1.1$, it is much more important to adjust the number of iterations to reach an optimal value with as little boundary reflections as well as the solution is to be converged – which have proved to be difficult. This is shown in Figure 62.

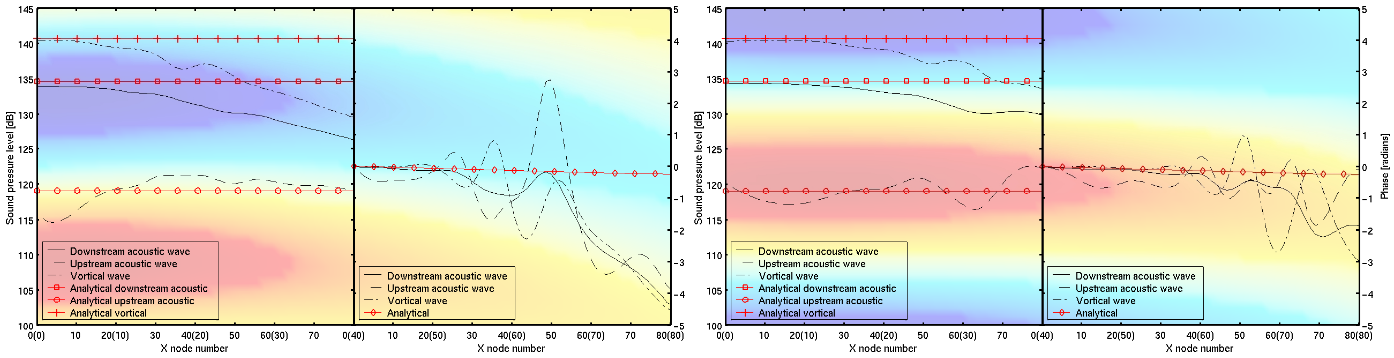

(a) 100 iterations.

(b) 150 iterations.

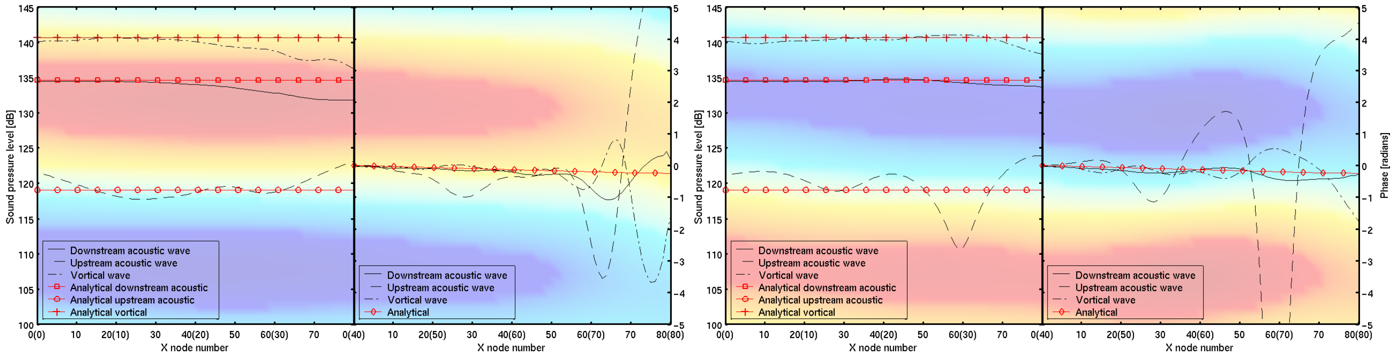

(c) 200 iterations.

(d) 300 iterations.

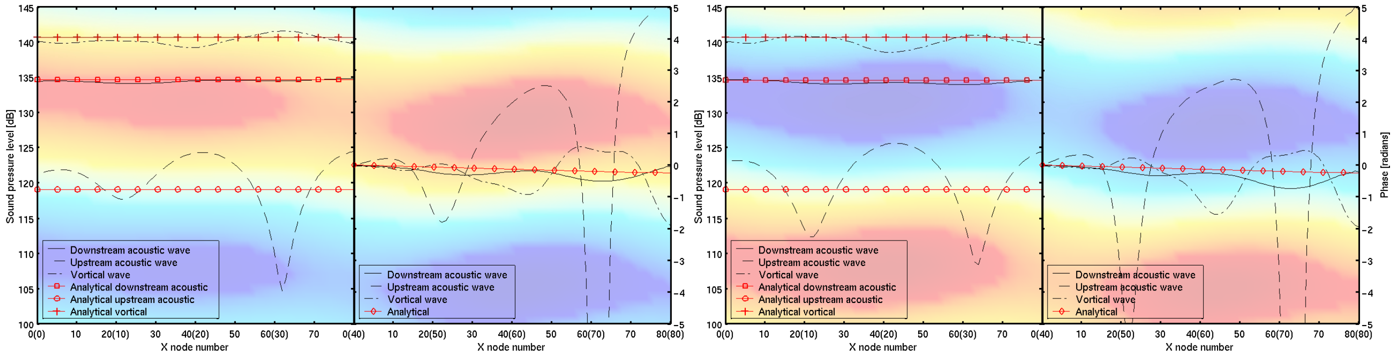

(e) 400 iterations.

(f) 500 iterations.

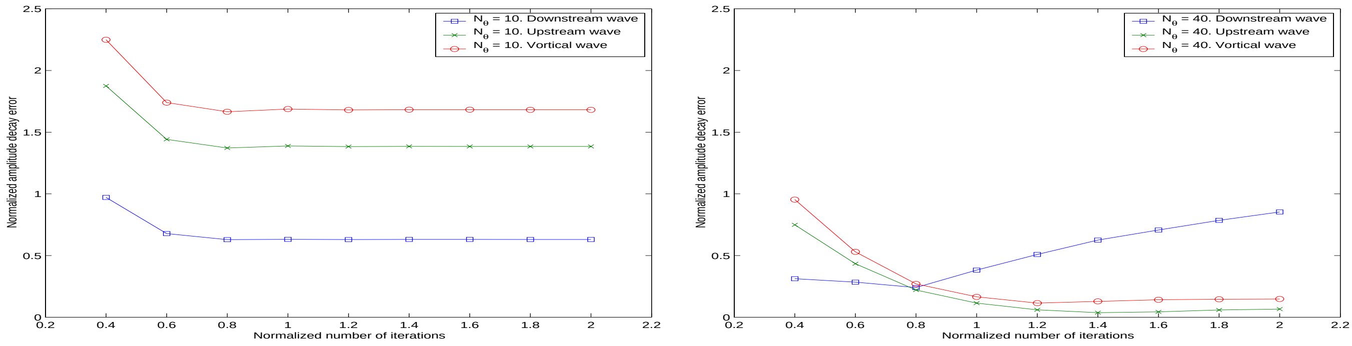

(g) $N_\theta = 10$ amplitude decay error against number of iterations.

(h) $N_\theta = 40$ amplitude decay error against number of iterations.

Figure 62. Development of amplitude and phase errors with increasing number of iterations for the run: $N_\theta = 40$, $\xi = 1.1$, $M = 0.4$.

9 Conclusion

From the results presented above, there are certain conclusions that can be drawn. First, as expected, increasing number of points per theoretical wavelength N_λ gives increasing accuracy of the result, but it also requires more computational time. An optimal number can not be established exactly, but in order to have good results within reasonable computational time a rough estimate of around 20-40 points per circumferential wavelength N_y should be sufficient to preserve the wave. Second, there are physical and numerical phenomena that has been more clarified during this work, that includes; viscous interaction, numerical dispersion and dissipation of sound waves, dependence of number of time steps per period, influence of different grid skew angles, and the errors induced by improper boundary conditions.

Generally, to preserve a sound wave using a numerical solver, one should keep the following in mind: 1) Decreasing number of points per theoretical wavelength N_λ will damp the wave by numerical dissipation, 2) increasing number of points per theoretical wavelength will introduce physical viscosity and larger truncation errors, 3) decreasing mach number will impose longer axial wavelength and thus less dissipation, 4) increasing mach number will then introduce more dissipation and also more iterations are required for convergence, 5) time steps per period should be kept not much less than 40 to ensure good quality, 6) second-order artificial viscosity for the mean flow equations is unimportant for the sound wave itself, 7) forth-order artificial viscosity parameter plays a small role on the result and should be kept in mind, 8) unless very high-resolution grid is used the turbulence is small and hence the turbulent Reynolds number and turbulent artificial viscosity parameters is unimportant, 9) with increasing grid cell aspect ratio the error is increasing especially when the axial wavelength N_x is small, 10) a grid skew angle other than in between -35° to 35° should be avoided and this has also shown strong dependence of which direction the wave is traveling, and 11) proper imposed boundary conditions is important to avoid reflections.

Last, it is important to ensure that the numerical solution is fully converged. This was a problem during the computations done in this project; amazingly an ambiguity in the definition of time steps required for convergence was found. This have caused that some of the results, especially the grid dependent, not have been obtained properly, thus it should be comparable when investigating trends only.

Appendix A

Dispersion error

To illustrate the roll that artificial viscosity plays on the stability of the scheme when large gradient or discontinuities occurs, a one-dimensional simplified version of the finite volume discretization (39) is used

$$\frac{\partial u_i}{\partial t} = -\left[\frac{f_{i+1/2} - f_{i-1/2}}{\Delta x}\right]_{\mathbf{I}}, \tag{98}$$

where the viscous part as well as the source term is removed. To give a brief overview a spectral analysis is done to see how the instabilities develop. Reformulating (98) to analytical form with mesh size of Δx

$$\frac{\partial u(x,t)}{\partial t} = -\frac{f(x + 1/2\Delta x, t) - f(x - 1/2\Delta x, t)}{\Delta x}$$

and Taylor expanding in the spatial domain

$$\frac{\partial u}{\partial t} = -\frac{\partial f}{\partial x} - \frac{1}{24}\Delta x^2 \frac{\partial^3 f}{\partial x^3} - \ldots$$

where the last term on the right hand side represents the truncation error, and makes it now apparent that this equation is of second-order $O(\Delta x^2)$. Since this scheme is semi-discrete (also called *method of lines*) and the time derivative is then solved separately implicit, it is not included in the Taylor expansion. Introducing $\frac{\partial f}{\partial x} = \frac{\partial f}{\partial u}\frac{\partial u}{\partial x} = a\frac{\partial u}{\partial x}$, where a would represent the Jacobian for a matrix formulation. One now obtain

$$u_t + au_x \simeq -\frac{1}{24}\Delta x^2 a u_{xxx} = \mu u_{xxx}, \tag{99}$$

which is a dispersive equation where μ is a constant.

The key observation is that if one look at a Fourier series solution to this equation, taking $\mathbf{U}(x,t)$ of the form

$$u(x,t) = \int_{-\infty}^{\infty} \widehat{u}(\xi,t) e^{i\xi x} \mathrm{d}\xi,$$

then the Fourier components with different wave number ξ propagate at different speeds, i.e. they disperse as time evolves. It is sufficient to consider each wave number isolated, because of linearity. Considering one wave of the form

$$u(x,t) = \widehat{u}(\xi,t) e^{i(\xi x - c(\xi)t)}$$

where the speed of the wave is given as $c(\xi)$. This is then inserted into (99)

$$c(\xi) = a\xi + \mu\xi^3, \tag{100}$$

from which this dispersion relation is obtained. An important velocity from this dispersion relation is the group velocity that is given by

$$c_g(\xi) = \frac{\mathrm{d}c}{\mathrm{d}\xi} = a + 3\mu\xi^2.$$

Comparing the group velocity with the wave velocity a, one can see that individual groups travels faster or slower, depending on the sign of μ, than the wave velocity. This difference causes oscillatory behavior near discontinuities, which further may cause the solution to "blow up". The most oscillatory components are found farthest $x = c_g(\xi)t$ from the correct location $x = at$.

Appendix B

Variation of flow dependent parameters

B.1 N_θ with constant ξ, upstream acoustic.

Figure 63. $N_\theta = 5$. Upstream.

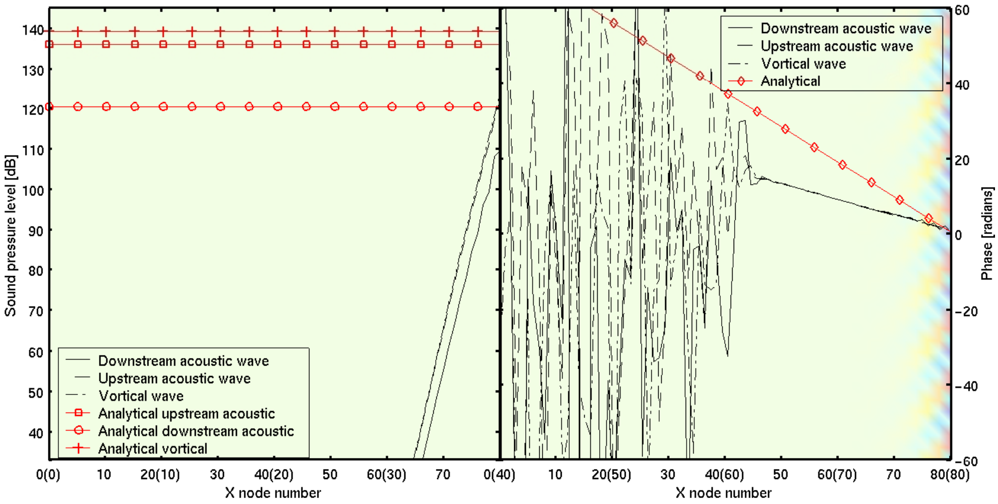

Figure 64. $N_\theta = 10$. Upstream.

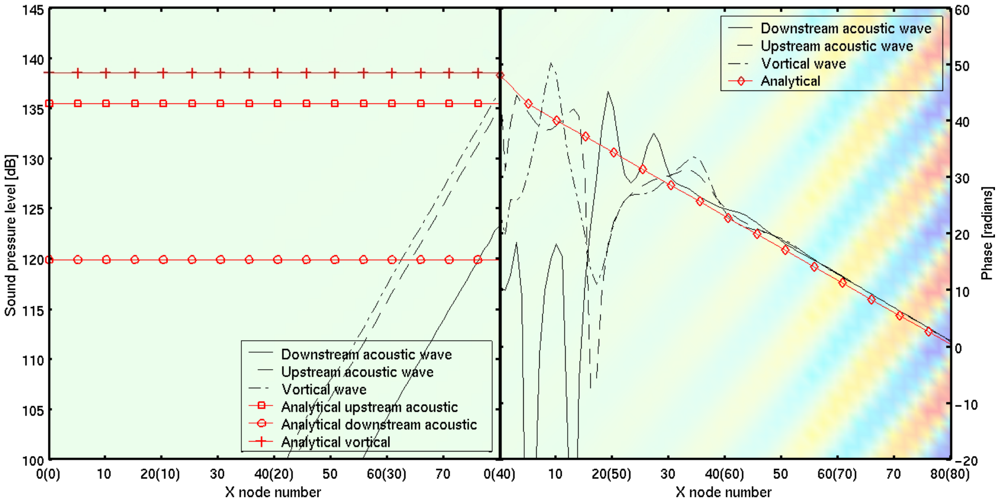

Figure 65. $N_\theta = 20$. Upstream.

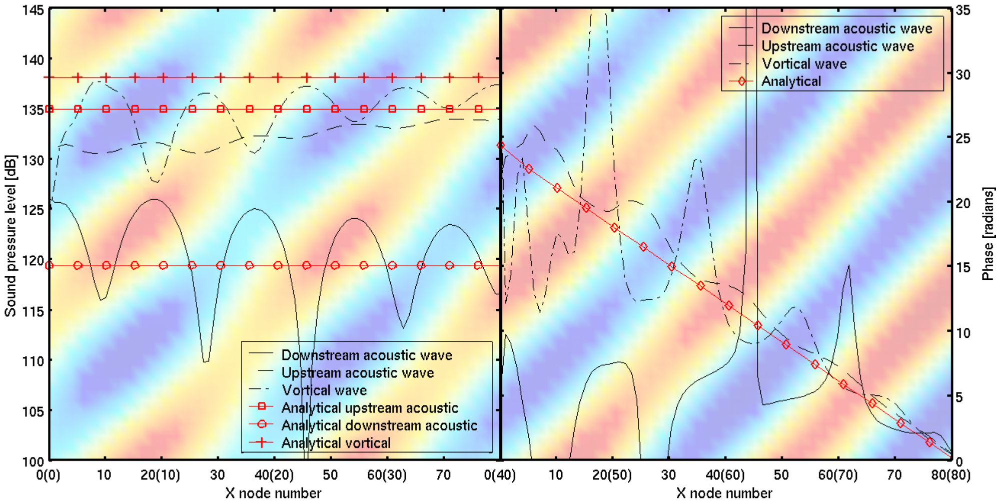

Figure 66. $N_\theta = 40$. Upstream.

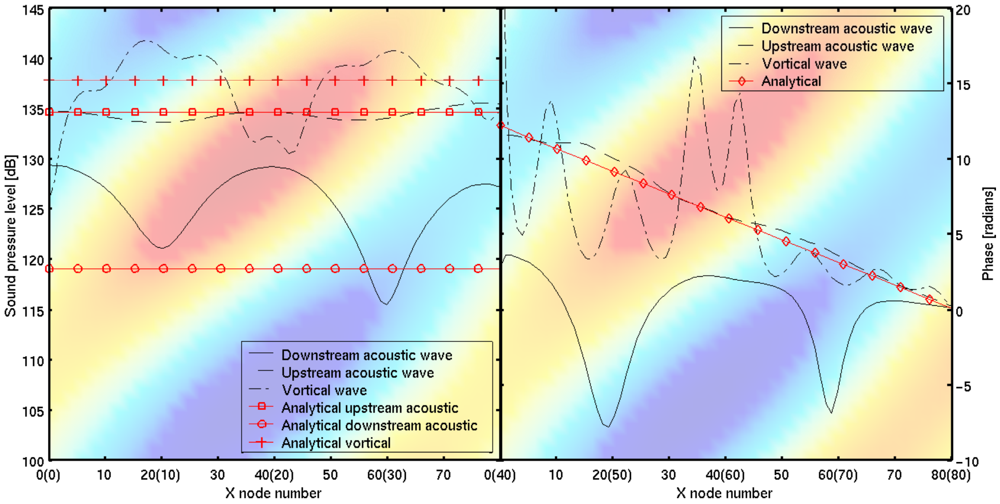

Figure 67. $N_\theta = 80$. Upstream.

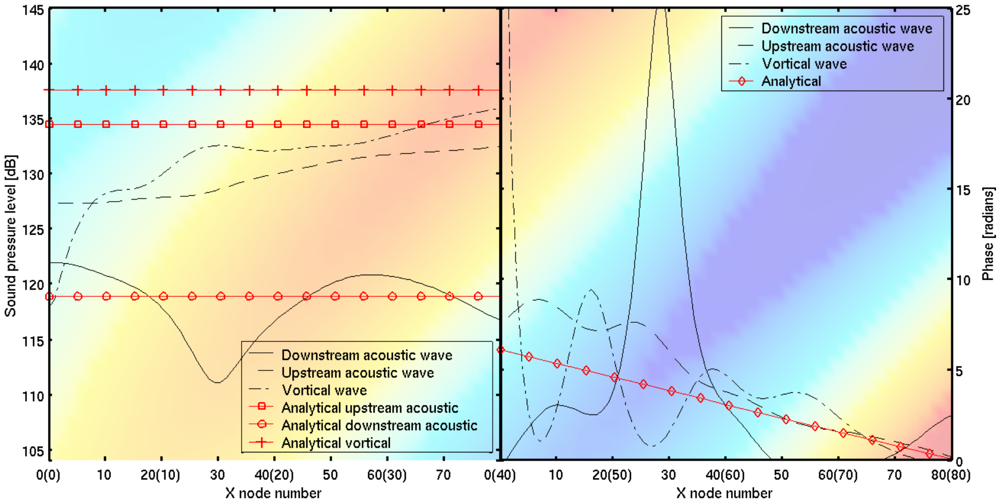

Figure 68. $N_\theta = 160$. Upstream.

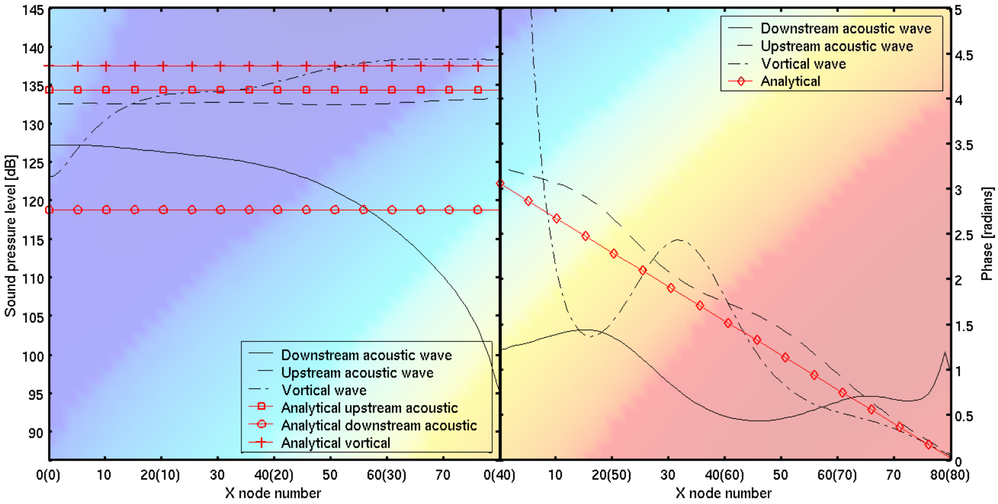

B.2 ξ with constant N_θ, upstream acoustic

Figure 69. $\xi = 0.7$. Upstream.

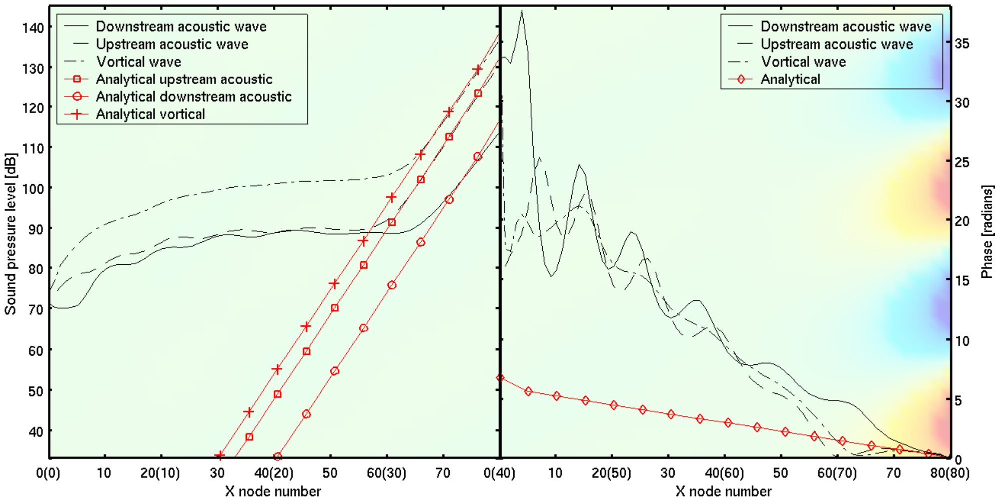

Figure 70. $\xi = 0.9$. Upstream.

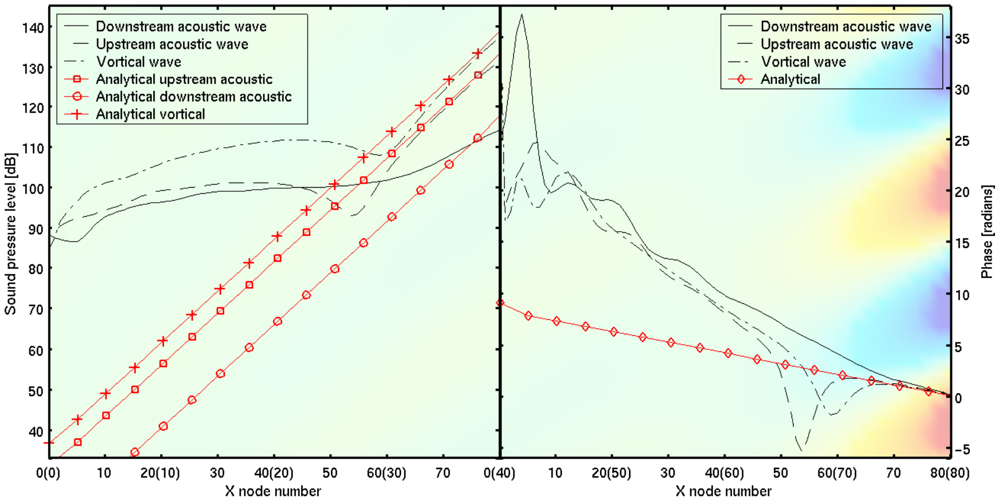

Figure 71. $\xi = 1.1$. Upstream.

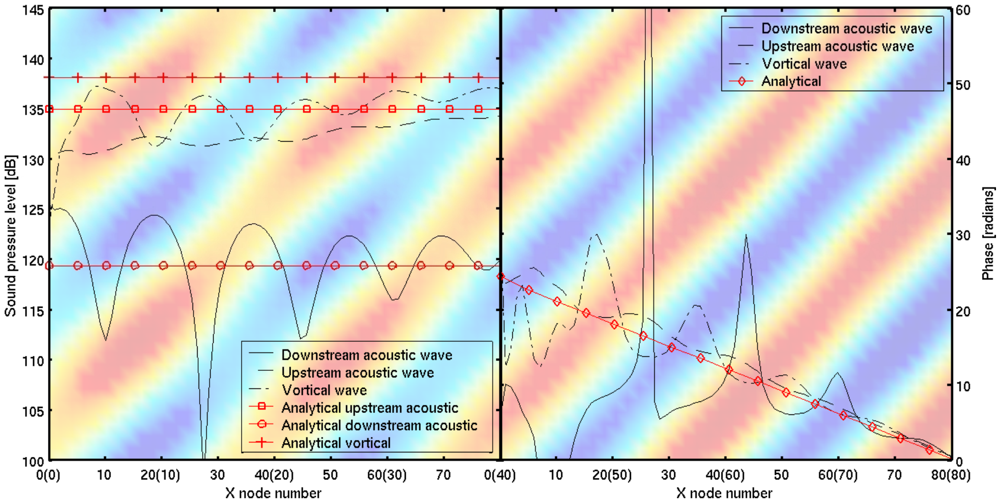

Figure 72. $\xi = 1.5$. Upstream.

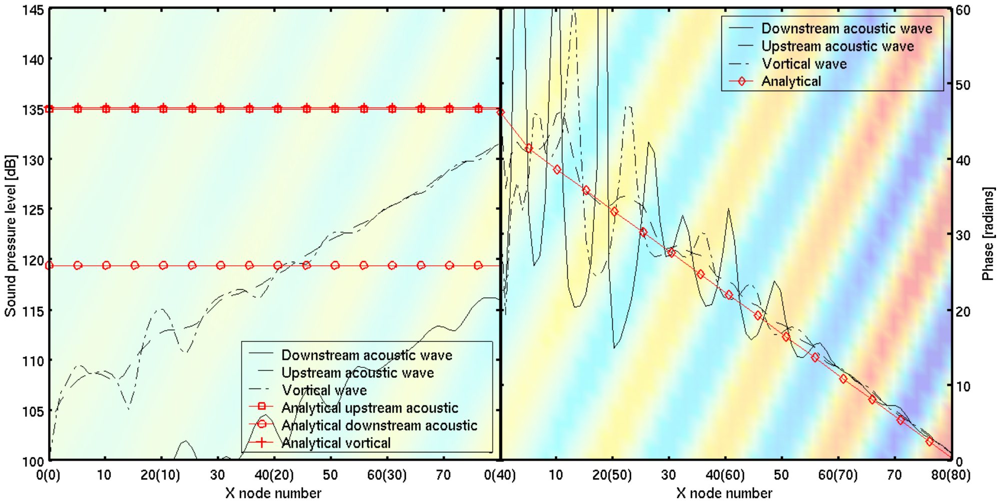

Figure 73. $\xi = 3.0$. Upstream.

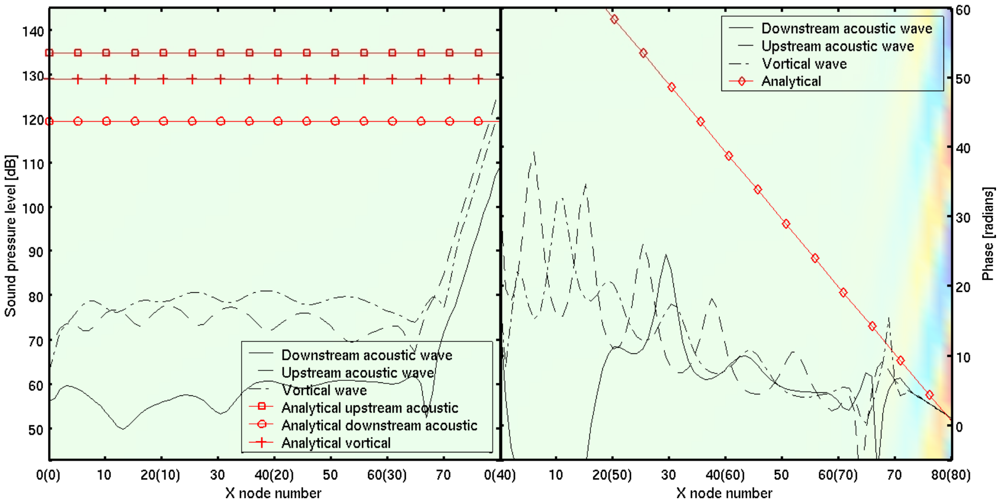

Figure 74. $\xi = 5.0$. Upstream.

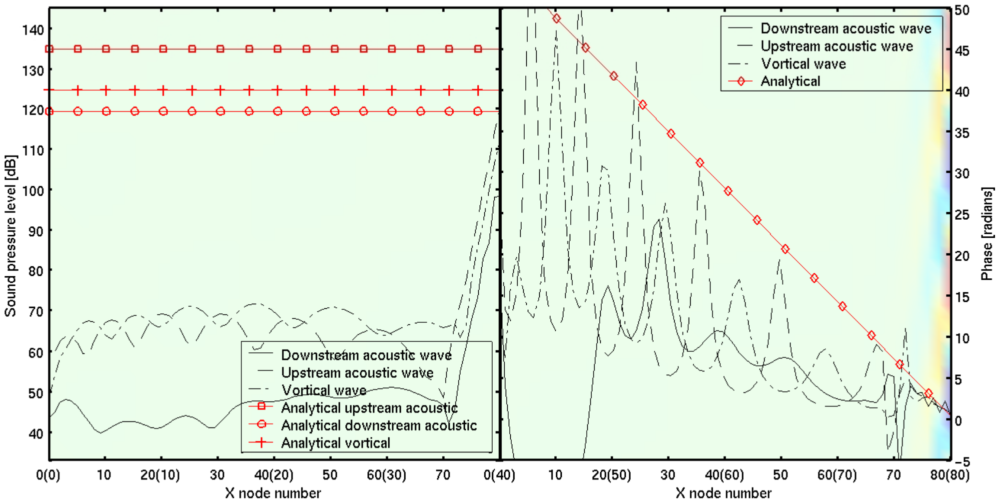

B.3 Mach number M, upstream acoustic

Figure 75. $M = 0.2$. Upstream.

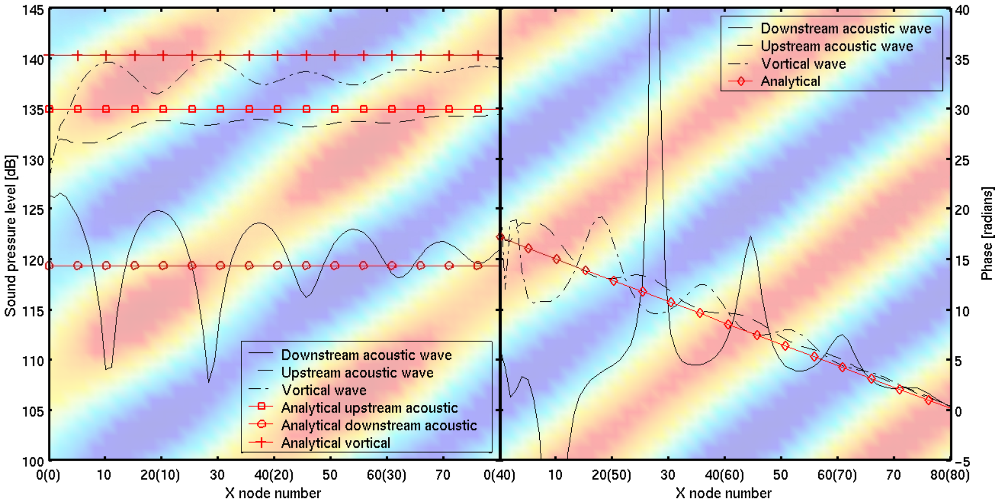

Figure 76. $M = 0.6$. Upstream.

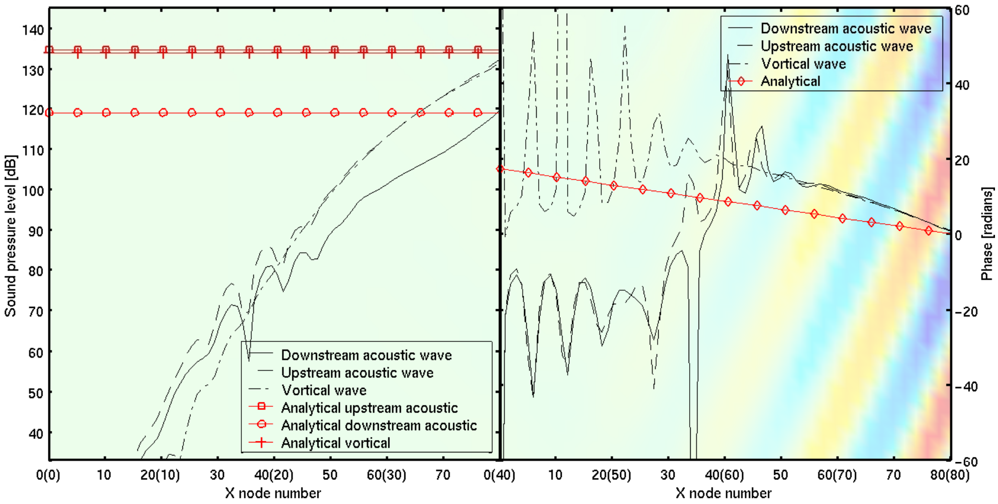

Figure 77. $M = 0.9$. Upstream.

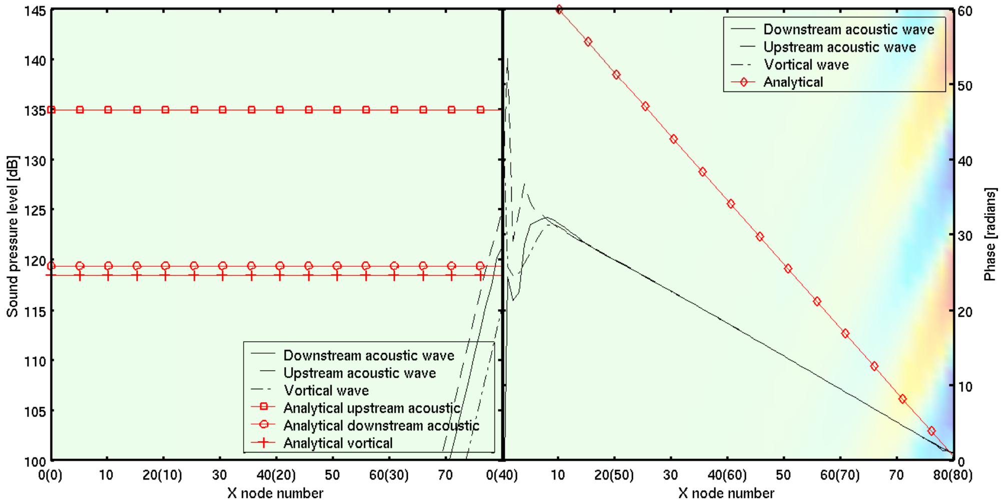

B.4 Comparisons of cut-off waves

Figure 78. Downstream, cut-off ($\xi < 0$ only). Amplitude error (left) and phase error (right) development as a function of the average points per theoretical wavelength.

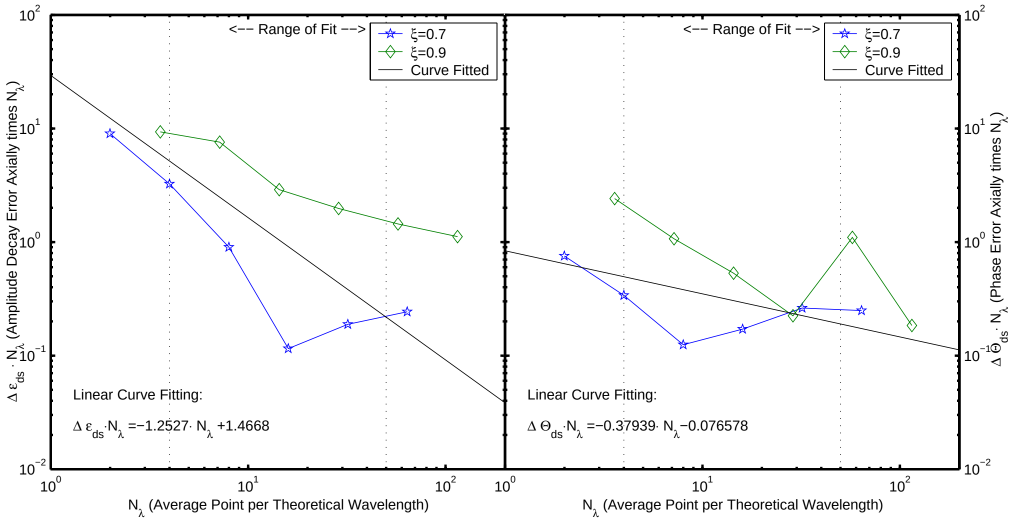

Figure 79. Upstream, cut-off ($\xi < 0$ only). Amplitude error (left) and phase error (right) development as a function of the average points per theoretical wavelength.

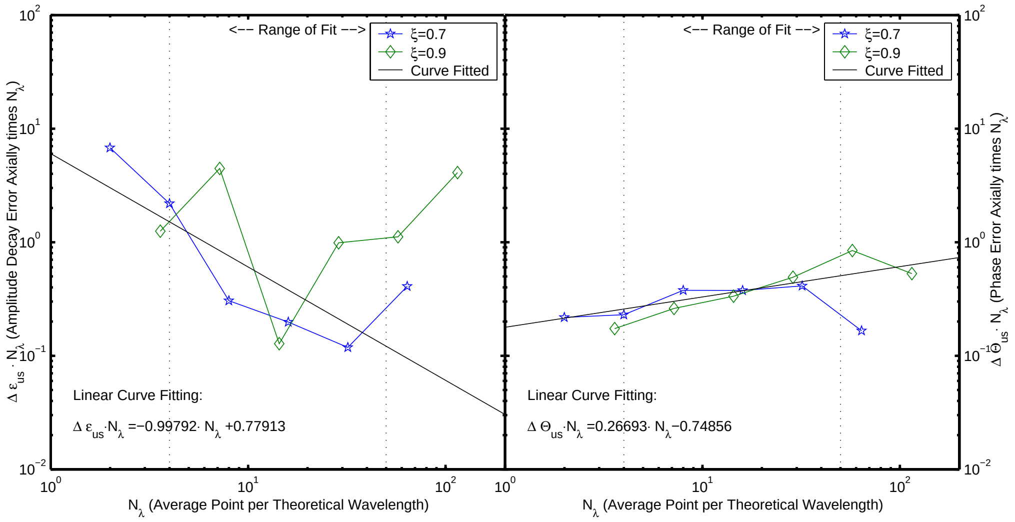

Appendix C

Variation of code dependent parameters

C.1 Time steps N_t per period in time, upstream

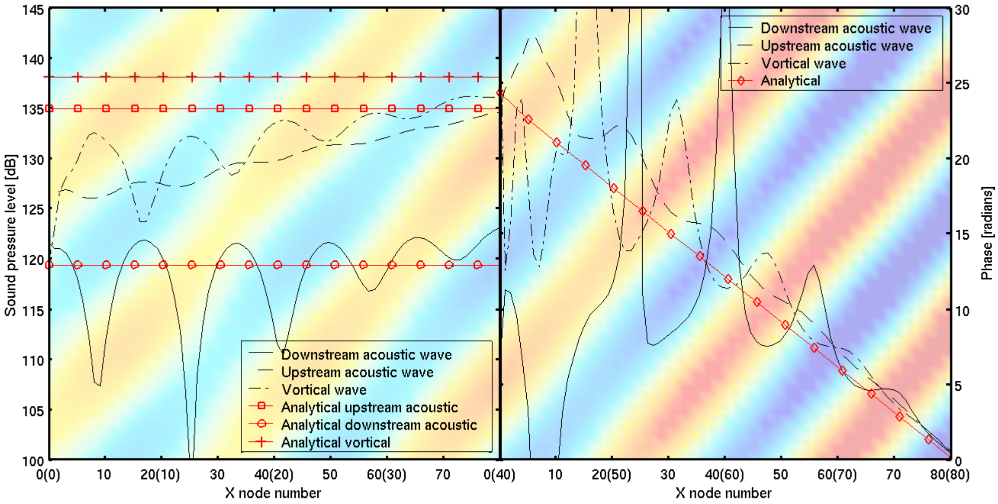

Figure 80. $N_t = 20$. Upstream.

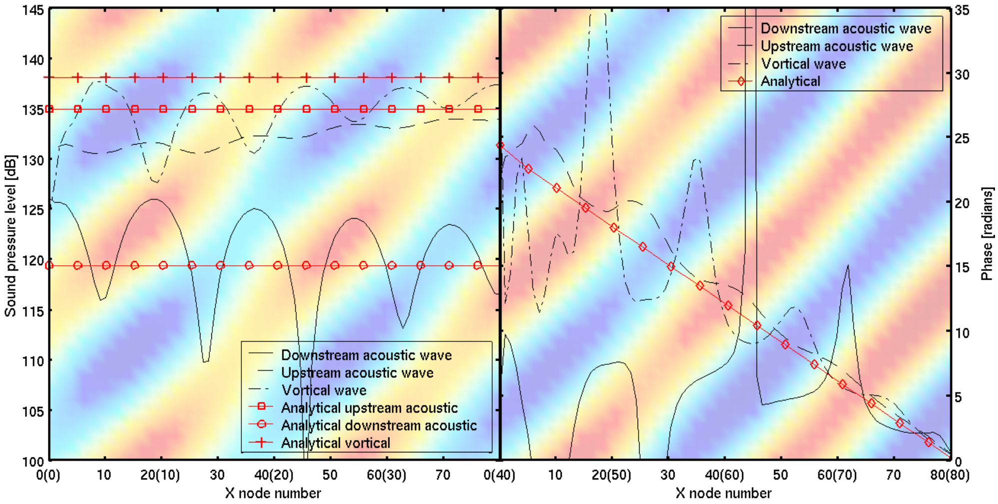

Figure 81. Default $N_t = 40$. Upstream.

Figure 82. $N_t = 80$. Upstream.

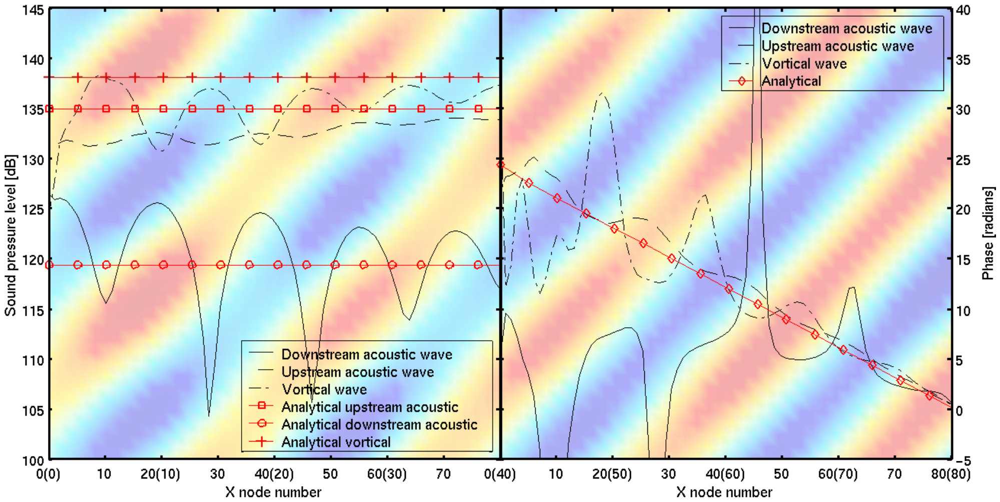

C.2 Euler calculation, upstream acoustic

Figure 83. Euler calculation. Upstream.

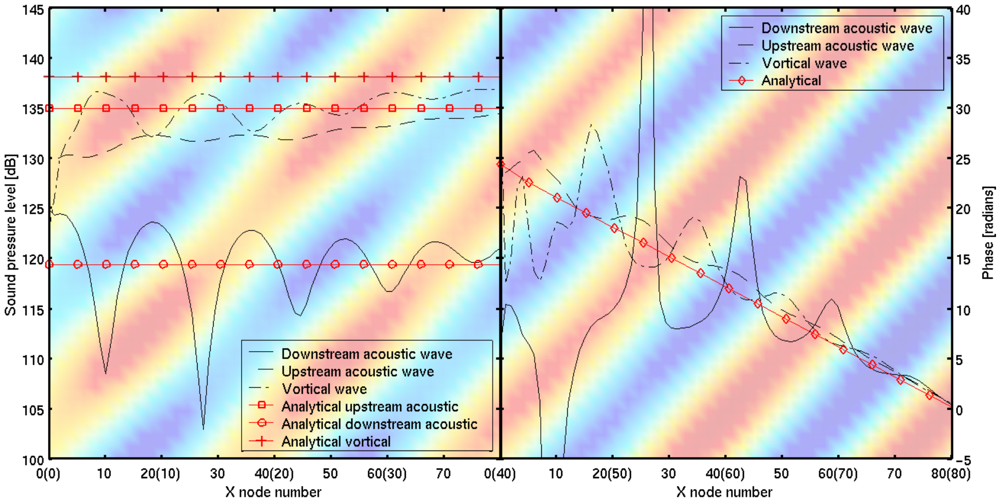

Appendix D

Grid dependent parameters

D.1 Variation of Cell Aspect Ratio $\frac{\Delta x}{\Delta y}$, upstream

Figure 84. Upstream. $\frac{\Delta x}{\Delta y} = 0.5$.

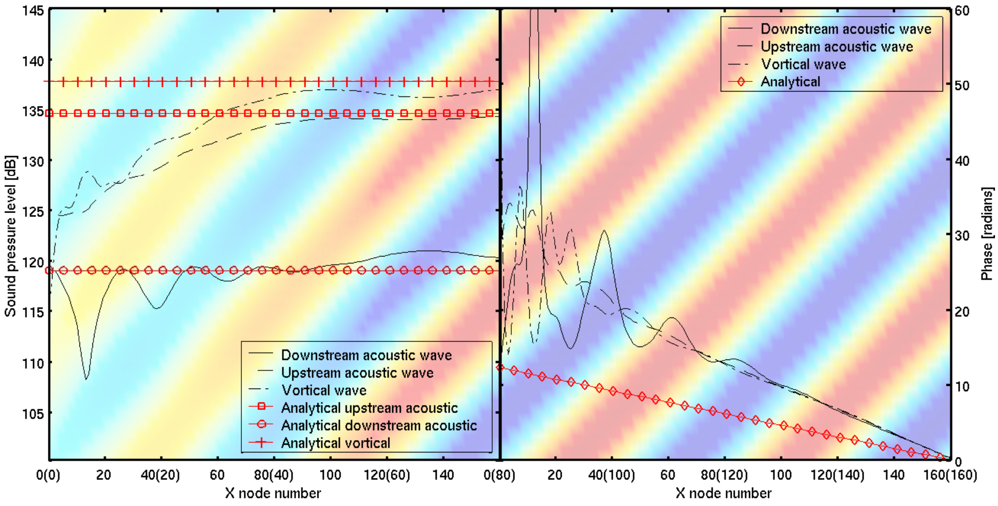

Figure 85. Upstream. $\frac{\Delta x}{\Delta y} = 2$.

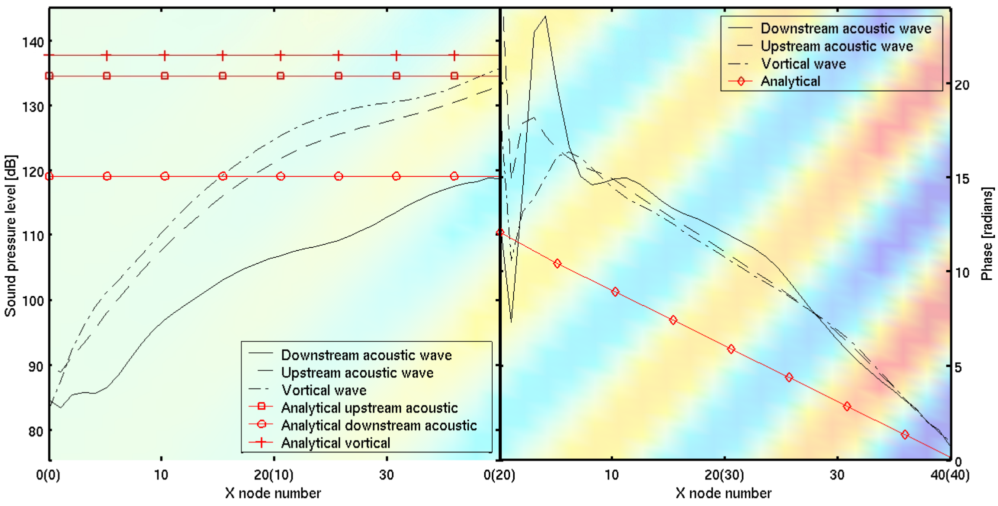

D.2 Skew Angle α, upstream acoustic

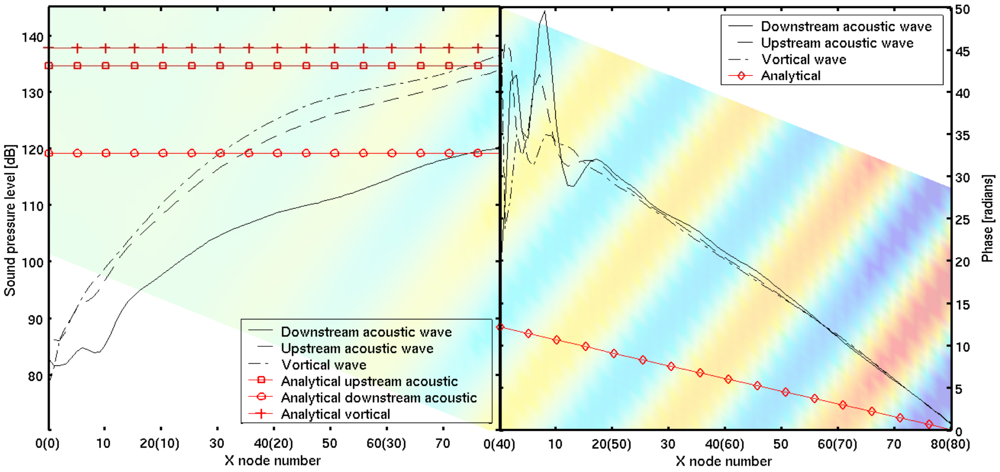

Figure 86. Upstream. $\alpha = 35°$.

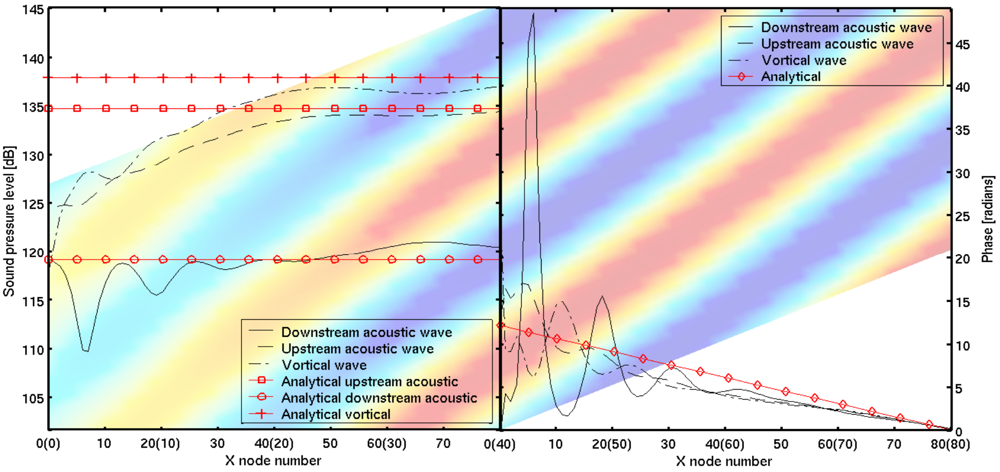

Figure 87. Upstream. $\alpha = -35°$.

D.3 Circumferential Distribution, upstream acoustic

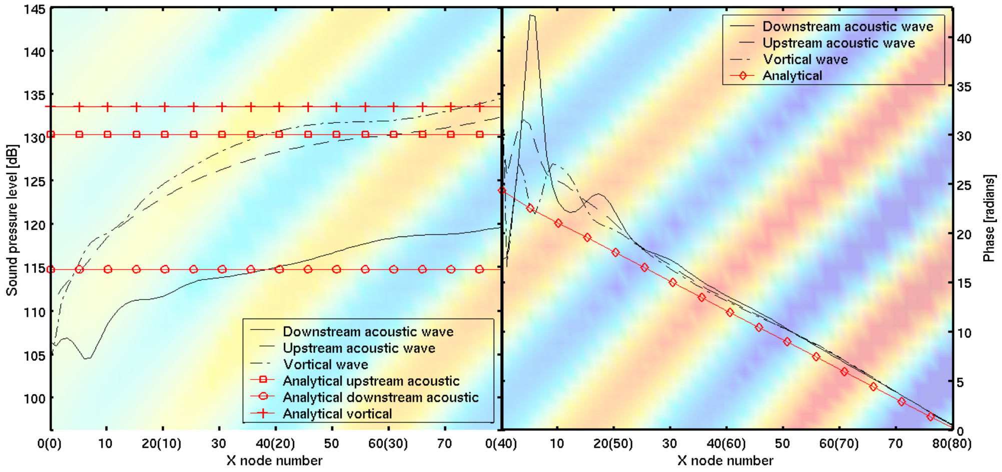

Figure 88. Upstream. Non-Uniform.

Appendix E

Evaluation of upstream acoustic output boundary condition

Figure 89. Upstream. Default parameters with Giles non-reflecting boundary condition at the acoustic output (left side of domain).

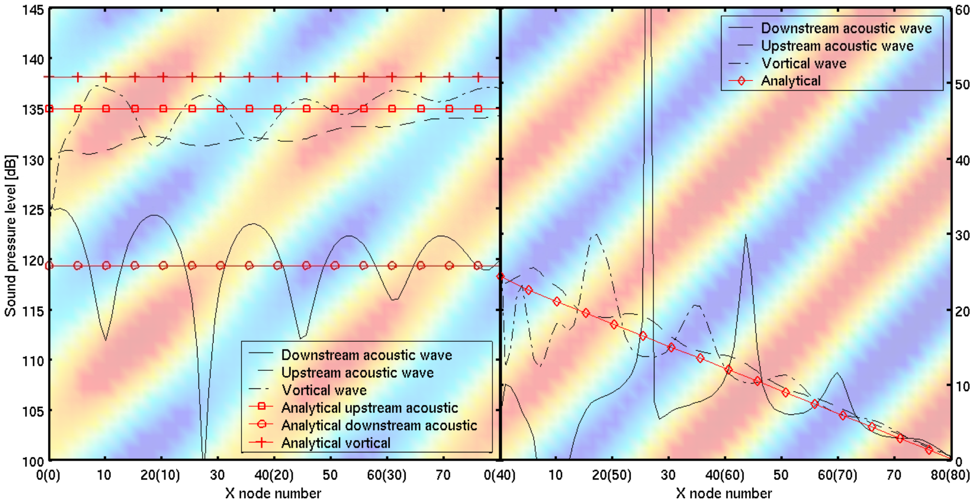

Figure 90. Upstream. Default parameters with Riemann boundary condition at the acoustic output (left side of domain).

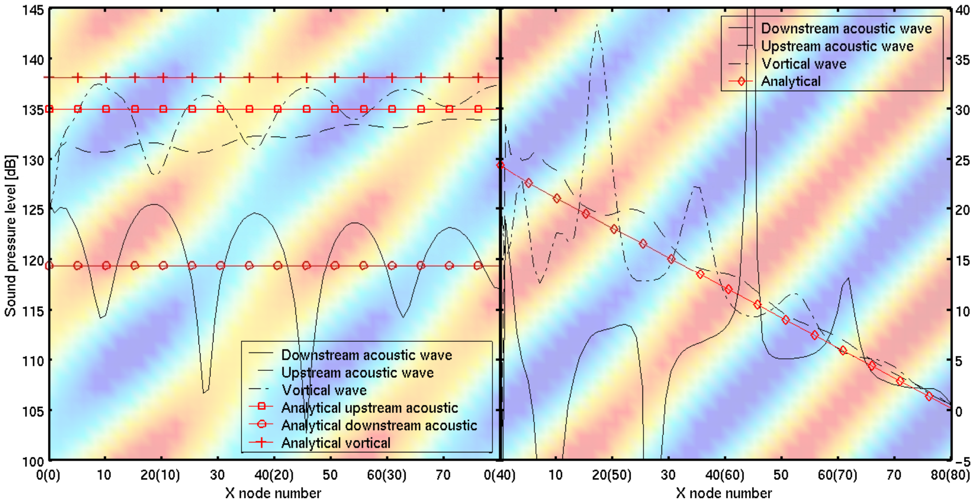

References

[1] Anderson, J. D., *Computational Fluid Dynamics*, McGraw-Hill Publishing Company, United States, 1992.

[2] Anderson, J. D., *Modern Compressible Flow*, McGraw-Hill Publishing Company, United States, 1990.

[3] Brooks, P. W., *The Modern Airliner*, Airlife Publishing Ltd, United Kingdom, 1996.

[4] Dowling, A. P. and Ffowcs Williams, J. E., *Sound and Sources of Sound*, Ellis Horwood Publishers, United Kingdom, 1983.

[5] Eliasson, P., Wang, D., Meijer, S. and Nordström, J. *Unsteady Euler Computations Through Non-Matching and Sliding-Zone Interfaces*, AIAA-paper 98-0371, FFA, Bromma, Sweden 1998.

[6] Giles, M., *Non-Reflecting Boundary Conditions for the Euler Equations*, Computational Fluid Dynamics Laboratory, Department of Aeronautics and Astronautics, Massachusetts Institute of Technology, United States, February 1988.

[7] Goldstein, *Aeroacoustics*, Airlife Publishing Ltd, United Kingdom, 1996.

[8] Hardin, J. C. and Hussaini, M. Y., *Computational Aeroacoustics*, Springer-Verlag New York Inc., United States, 1993.

[9] Hirsch, C., *Numerical Computation of Internal and External Flows Vol. 1*, John Wiley & Sons Inc, United Kingdom, 1988.

[10] Hirsch, C., *Numerical Computation of Internal and External Flows Vol. 2*, John Wiley & Sons Inc, United Kingdom, 1990.

[11] Jamesson, A., Schmidt, W. and Turkel, E., *Numerical Simulation of the Euler Equations by Finite Volume Methods using Runge-Kutta Time Stepping Schemes*, AIAA-paper 81-1259, AIAA 5^{th} Computational Fluid Dynamics Conference, United States, 1991.

[12] Johansson, A. V. and Burden, A. D., *An Introduction to Turbulence Modelling*, Department of Mechanics, Royal Institute of Technology, Sweden, 1998.

[13] Kramer, J., et. al, *Fan Noise and Performance*, Proceeding of the conference Aircraft Engine Noise Reduction May 16-17, 1972, NASA Lewis Research Center, Clevland, United States, 1972.

[14] Kreiss, O. H., Gustavsson, B. and Olieger, J., *Time Dependent Problems and Difference Methods*, Wiley-Interscience Publication, United States 1995.

[15] Rizzi A., Eliasson P., Lindblad I, Hirsch C., Lacord C. and Häuser S., *The Engineering of Multiblock/Multigrid Software for Navier-Stokes Flows on Structured Meshes*, Computers Fluids, vol 22 pp. 341-367, 1993.

[16] Rumsey, C. L., *Computation of Acoustic Waves Through Sliding-Zone Interfaces Using an Euler/Navier-Stokes Code*, AIAA-paper 96-1752, NASA Langley Research Center, United States, 1996.

[17] Shieh, C. M. and Morris, P. J., *High-Order Accurate Dual Time-Stepping Algorithm for Viscous Aeroacoustic Simulations*, AIAA-paper 98-2361, Department of Aerospace Engineering, The Pennsylvania State University, United States, 1998.

[18] Sjögreen, B., *Lecture notes on shock capturing difference methods*, Department of Numerical Analysis and Computer Science, Royal Institute of Technology, Sweden, 1999.

[19] Smith, M. J., *Aircraft Noise*, Cambridge University Press, United States, 1989.

[20] Tam, C. K. W and Webb, J. C., *Dispersion-Relation-Preserving Finite Difference Schemes for Computational Acoustics*, Department for Mathematics, Florida State University, Tallahassee, Florida, United States, 1992.

[21] Tannehill, J. C., Anderson, D. A. and Pletcher, R. H., *Computational Fluid Mechanics and Heat Transfer*, Taylor & Francis Publishing Company United States, 1997.

[22] Tyler, J. M. and Sofrin, T. G., *Axial Flow Compressor Noise Studies*, Pratt & Whitney Aircraft Div., SAE Transactions Vol. 70 pp 309-332, United States, 1962.

[23] Whitham, G. B., *Linear and Nonlinear Waves*, John Wiley & Sons Inc, United States, 1999.

[24] Wilson, A. G., *A Method for Deriving Tone Noise Information from CFD Calculations on the Aeroengine Fan Stage*, draft paper, Rolls-Royce plc, United Kingdom, 2000.

[25] Wilson, A. G., *Turbomachinery Noise Source CFD models for Low Noise Aircraft Designs*, TurboNoiseCFD-RR-01-WP1-01, Rolls-Royce plc, United Kingdom, 2001.

Utgivare Totalförsvarets Forskningsinstitut – FOI Avdelningen för Flygteknik, FFA SE-172 90 STOCKHOLM	Rapportnummer, ISRN FOI-R–0330–SE	Klassificering Vetenskaplig rapport
	Månad år 5. december 2001	Projektnummer C840234
	Verksamhetsgren 3. Flygteknisk forskning	
	Forskningsområde 7. Bemannade och obemannade farkoster	
	Delområde 73. Flygteknisk forskning	
Författare Kristoffer Jensen och Gunilla Efraimsson	Projektledare Gunilla Efraimsson	
	Godkänd av Torsten Berglind Chef, Institutionen för Beräkningsaerodynamik	
	Tekniskt och/eller vetenskapligt ansvarig Gunilla Efraimsson Institutionen för Beräkningsaerodynamik	

(101)

Rapporttitel

Krav på upplösning vid beräkning av fläktbuller från flygmotorer med CFD-verktyg

Sammanfattning

Jetbuller från flygplan har efter många års forskning blivit reducerad till ett minimum. Dock är det fortfarande problem med att hålla ljudnivåerna låga vid start och inflygning. Grunden till detta är huvudsakligen bullret från fläkten i motorn. Det är således tryckfluktuationerna som genereras i kompressorn eller turbinen som blir de dominerande ljudkällorna. Genereringen av bullret är icke-injära och komplexa aerodynamiska problem. Med hjälp av CFD-verktyg kan problemet nu bli studerat i detalj, men det finns fortfarande begränsningar eftersom det krävs många punkter per våglängd för att den fysikaliska lösningen inte ska bli förstörd av numeriska fel.

De linjära ekvationer som beskriver utbredningen av akustiska vågor i luft löstes analystiskt. Därefter löste vi samma problem, men nu beskrivna av de icke-linjära Navier-Stokes ekvationerna, numeriskt med ett finita volym schema. Den numeriska lösningen jämfördes sedan med den analytiska lösningen för att hitta fel som kan härröra från t.ex. disspertion, dissipation och reflexioner från randvilkoren.

Ett optimalt antal punkter per våglängd kunna inte hittas direkt, men för att kunna uppnå goda resultat inom acceptabla beräkningstider, är en uppskattning på omkring 20 - 40 punkter per våglängd tillräckligt för att behålla kvaliteten på vågen. Övriga felkällor som noterades var numerisk disspertion och dissipation, antal tidssteg per tidsperiod, påverkningen av skjuvade nät samt hur felet beror av randvillkoren.

Nyckelord

Aeroakustik, Fläkt-buller, Finita volym metoden, Icke-reflekterande randvilkor, Numerisk disspersion, Numerisk dissipation, Turbin, Vågdelning

Övriga bibliografiska uppgifter

Examensarbete

ISSN ISSN 1650-1942	Antal sidor 79	Språk Engelska
Distribution enligt missiv	Pris Enligt prislista	
	Sekretess Öppen	

Issuing organisation

FOI – Swedish Defence Research Agency
Division of Aeronautics, FFA
SE-172 90 STOCKHOLM

Report number, ISRN

FOI-R–0330–SE

Report type

Scientific report

Month year

December 5, 2001

Project number

C840234

Customers code

3. Aeronautical Research

Research area code

7. Vehicles

Sub area code

73. Aeronautical Research

Author(s)

Kristoffer Jensen and Gunilla Efraimsson

Project manager

Gunilla Efraimsson

Approved by

Torsten Berglind
Head, Computational Aerodynamics Department

Scientifically and technically responsible

Gunilla Efraimsson
Computational Aerodynamics Department

Report title

Aeroengine Fan-Noise Resolution Requirement in Computational Fluid Dynamics

Abstract

Jet-noise has eventually been reduced to a minimum, but still there are problems in keeping the overall noise levels low during take-off and approach. The reason for this is basically that fan-noise, i.e. pressure fluctuations generated in the compressor or turbine, becomes dominating. This phenomenon can be recognized as non-linear and complex aerodynamics rather than acoustic problem in nature, and thus it becomes difficult to obtain models that are general and accurate. However, with the aid of CFD, the problem can now be studied in detail, but unfortunately this requires a very large number of points per wavelength to distinguish the wave solution from numerical errors.

Applying the well-established linear methods for aeroacoustics in a parallel wall-duct to the fan stage, one can obtain analytical expressions for the dispersion-relation. A sinusoidal acoustic wave with the known dispersion-relation is then propagated thru a 2D numerical fan stage using a time-dependent finite-volume scheme. The numerical solution is then compared with the original wave to identify deviations that could originate from dispersion, dissipation and reflections induced by the numerical boundaries.

An optimal number of points per wavelength were not established exactly, but in order to have good results within reasonable computational time a rough estimate of around 20 - 40 points per circumferential wavelength has shown to be sufficient to preserve the wave. In addition, certain physical and numerical phenomena applied to aeroacoustics has been more clarified, that includes; viscous interaction, numerical dispersion and dissipation of the sound waves, dependence of number of time steps per period, influence of different grid skew angles, and the errors induced by improper boundary conditions.

Keywords

Aeroacoustic, Fan-noise, Finite volume method, Non-reflecting boundary condition, Numerical dispersion, Numerical dissipation, Turbomachinery, Wave splitting

Further bibliographic information

Master’s Thesis

ISSN

ISSN 1650-1942

Pages

79

Language

English

Price

Acc. to price list

Security classification

Unclassified